TRANSIT SPECTROSCOPY OF THE EXTRASOLAR PLANET HD 209458B: THE SEARCH FOR WATER

A Dissertation

Presented to the Faculty of the Graduate School

of Cornell University

in Partial Fulfillment of the Requirements for the Degree of

Doctor of Philosophy

by

Patricio Michel Rojo

January 2007

TRANSIT SPECTROSCOPY OF THE EXTRASOLAR PLANET HD 209458B: THE SEARCH FOR WATER

Patricio Michel Rojo, Ph.D.

Cornell University 2007

This dissertation describes an attempt to detect water in the atmosphere of the extrasolar planet HD 209458b using transit spectroscopy. It first discusses the importance of water detection and reviews the state of knowledge about extrasolar planets. This review discusses the main statistical trends and describes the detection methods employed to this date. The importance of the transiting planets and the many measurements of the known ones are also discussed.

A radiative transfer model designed and built specifically for this project predicts, given a planetary temperature/pressure/composition profile, the dependence in wavelength of the stellar spectrum modulation due to a transiting planet. A total of 352 spectra around 1.8 μm were obtained on four nights (three in transit) of observations on August 3–4, September 26, and October 3 of 2002 using ISAAC at the Very Large Telescope.

Correlating the modeled modulation with the infrared spectra yields a non-detection of water in the atmosphere of HD 209458b. It is found that the non-detection is due to an unfortunate choice of observing parameters and conditions that made it impossible to reach the required sensitivity. Nonetheless, the results are scaled with synthetic spectra to place strong limits on the planetary system configurations for which the observing parameters and telluric condi-

tions would have yielded a successful detection. None of the 10 other known transiting planets would be detectable with the choice of parameters and conditions for this observation.

A quantitative model of an improved observing strategy for future observations of this kind is developed. The improvements include: airmass and timing constraints, the simultaneous observation of a calibrator star, and a new method to find the optimal wavelength range.

The data-reduction process includes several original techniques that were developed during this work, such as a method to remove fringes from flat fields and several methods to correct for telluric absorption, among others.

Some of the code developed for this project is available under the GNU General Public License at the DSpace Internet archive from Cornell University.

BIOGRAPHICAL SKETCH

Patricio M. Rojo was born in Santiago, Chile, to his parents Patricio and María Isabel. Since his teens, he was interested in astronomy. However, he thought that everything was already known and did not realized that research could still be done in astronomy until late high school. Since then, he decided to follow Astronomy as profession.

He thus studied physics at the Universidad de Chile, where he obtained the *Licenciatura en Ciencias* (B.Sc. equivalent) degree in 2000, majoring in physics. Then, he continued at the same university and, in 2001, he completed a M.Sc. in Astronomy.

While doing his undergraduate work, Patricio met Andrea Matus through a romantic car accident; 4 years later they were married. Four days after the wedding, the couple flew to the United States, where Patricio began his Ph.D. studies at Cornell University. Patricio and Andrea then spent the next 5 years in Ithaca, NY, a small town with long, cold winters, but surrounded by an exceptional landscape amid rivers, lakes, and waterfalls.

In 2006, Patricio finished his Ph.D. studies and continued on to an academic position at his alma mater, the Universidad de Chile.

Con todo mi amor para mi esposa Andrea, compañera de innumerables sueños.

With all my love to my wife Andrea, companion of countless dreams.

ACKNOWLEDGEMENTS

I am very grateful to all the members of the Astronomy Department at Cornell University. I thank the staff for their great support and kindness, the professors who shared their knowledge with me, and especially those who guided me through my research: my advisor, Dr. Joseph Harrington, and the members of my committee, Dr. Peter Gierasch, Dr. Donald Campbell, and Dr. Warren Allmon. I also thank all the other people from other institutions who advised and collaborated with me in this topic, especially Dr. Drake Deming, and Dr. Günther Wiedemann.

My experience at Cornell was very rewarding academically, however my professional development would have not been complete without friendship and help from many people.

Most importantly, I would like to thank my beloved wife for all her understanding, support, and immense patience during the long hours I spent working; as well as for all her unyielding energy to go places and socialize, which produced such great memories of Ithaca.

I thank my friends, Taner, Jason, Denise, Amelie, and Pierre for their unconditional friendship and support when most needed throughout these years; Eldar and his unstoppable energy that gave us so many enjoyable moments and permitted us to start our stay in Ithaca with such ease; Marko for his great generosity; and all the others great friends that I will never forget: Barbara, Bistra, Pablo and Cecilia, Sabrina, Marta, Vicenta, Bo, Sam, Ivan, Tsveti, and Rodrigo, among others. Also, I like to mention the kind company of my late cat, Fibi.

I would also like to express my gratitude to all the people who helped more indirectly: my family, and all the persons from Department of Astronomy at the

Universidad de Chile for their support, especially to Dr. Maria Teresa Ruiz, who gave me my first opportunity and great motivation to do research in science.

Finally, I also want to thanks Dr. Deborah Campbell and Dr. Joseph Harrington for their careful proofreading of this work and their dedication in correcting my broken English.

This work was supported by the National Aeronautics and Space Administration under grant NAG5-13154 issued through the Science Mission Directorate. This publication makes use of data obtained from the Very Large Telescope (VLT), the W. M. Keck Observatory, and also of products from the Two Micron All Sky Survey. The VLT is operated by the European Southern Observatory (ESO). W. M. Keck telescope time was allocated to the National Aeronautics and Space Administration through the agency's scientific partnership with the California Institute of Technology and the University of California. The Observatory was made possible by the generous financial support of the W.M. Keck Foundation. The Two Micron All Sky Survey is a joint project of the University of Massachusetts and the Infrared Processing and Analysis Center at the California Institute of Technology, funded by the National Aeronautics and Space Administration and the National Science Foundation.

TABLE OF CONTENTS

LIST OF FIGURES

LIST OF TABLES

LIST OF SYMBOLS

Symbol	Meaning
$f_\star$	λ-dependent flux at Earth from the star
$F_\star$	total flux at Earth from the star
$I_\star$	intensity at the center of the star
$B(R)$	limb darkening. $B(0) = 1$
R	projected distance to the center of the disc
A	bond albedo
$p(\alpha)$	phase function of the planet
α	planet-star-Earth angle
$R_\star$	radius of the star
$M_\star$	mass of the star
R_p	radius of the planet
M_p	mass of the planet
a	orbital semi-major axis

Introduction | 1

Sunrise of a gigantic red sun or sunsets of two different suns are no longer in the sole realm of fiction. In the almost 200 extrasolar planets discovered to this date, the variety of orbital configurations and planetary characteristics has been closer to what science fiction writers have imagined than what theoretical models of planetary system formation expected.

Thanks to the maturity of techniques and the increasing time span of surveys, new planets are being discovered every month. Nevertheless, the real challenge is to be able to characterize extrasolar planets. Until less than 15 years ago, our planetary knowledge was limited to our own Earth, the 8 other planets orbiting our sun, all the satellites, and the myriad small bodies like asteroids and comets. In those times, the theories of planetary formation and evolution were very consistent with the observations. However, ever since the first discoveries of extrasolar planets, those theories have been challenged and in some cases proved wrong (see, for example, the discussion about gravitational instabilities in §1.2). If we consider that this happened mostly by just observation of the orbital and dynamical configurations of the extrasolar systems, we might be heading for an even bigger surprise once we start measuring in detail the atmospheric or geological conditions on extrasolar planets.

This chapter first addresses the importance of water and introduces the topic

of extrasolar planets. It then finishes with a description of my project to measure the abundance of water on the extrasolar planet HD 209458b. An outline of the strategy employed in this project is presented.

1.1 Water

Detection of water in an extrasolar planet has a two-fold importance as a biological and as a chemical indicator.

1.1.1 Water and life

For many, the ultimate goal of extrasolar exploration is to identify planets that could potentially harbor life. Organic life as we know it requires some basic environmental conditions to survive, yet it may require variability to evolve. Planets where energy exchange between organic molecules is hindered by strong chemical conditions will be hard-pressed to allow the formation of even the most primitive bacteria. A planet without weather variability, on the other hand, might be *too dull* to provoke any struggle for existence and thus evolution of simple organisms to more complex ones. Nonetheless, it would be undoubtedly valuable to find such a planet to study this other extreme of life.

The presence of liquid water has been identified as one of the most basic requirements for organic life; its presence is indispensable for the most basic cellular functions. Hence, the planetary habitable zone (HZ) is defined as the range of distances from the star at which the surface temperature of a planet will permit liquid water (Kasting et al., 1993). The inner and outer boundary radii of this zone depend on many factors, which range from tidal heating and greenhouse effect, which push the boundaries outwards, to enhanced forma-

tion of water-vapor clouds, which provokes an increase in the albedo, and thus pushes the boundaries inward.

However, there could be many exceptions of habitable planets outside the formal boundaries of the HZ. In fact, we need look no further than our own solar system, where we might have two cases. Both Jupiter's moon Europa (e.g., Kuskov and Kronrod, 2005), and more recently Saturn's moon Enceladus (Spencer et al., 2006), show evidence of liquid water underneath their ice crusts, produced by tidal heating due to their host planets. Potentially, there could be more bizarre cases: for example, imagine a hypothetical rocky planet inside the inner boundary of the HZ and tidally locked to the star. The illuminated hemisphere is thus kept at high temperatures by the continuous radiation, in contrast with the other hemisphere, which is kept at cold temperatures, in permanent darkness. It could then be possible for a small region with liquid water to exist at the boundary of the two hemispheres.

Only by statistical averages can we talk about an HZ. The 9 planets in our solar system can hardly be called a statistically complete sample to characterize the boundaries of the HZ accurately. Therefore, to obtain empirical evidence for models, it is necessary to characterize the presence of water outside our solar system. Currently, we can only look at extrasolar giant planets (EGPs), but advances in technology should eventually permit measurements of rocky planets' atmospheres. Ultimately, the best way to study these distant objects will be through the construction of a new generation of space telescopes with relatively large light-collecting areas and state-of-the-art instruments whose sensitivities are orders of magnitude better than what is currently available (see, for example, the description of the SIM, GAIA, Kepler, COROT, Darwin, and TPF mis-

sions in Chapter 2). During the next few decades we should see these projects mature and finally launch. In the meantime techniques have to be refined so that the science return from these expensive endeavors can be maximized. Most of the techniques currently in use to characterize EGPs will easily be extensible to Earth-sized planets once the required sensitivity is reached.

In parallel with the refinement of the observing technique, effort has been given to improve the models that will constrain or help explain the life-search-oriented observations. The stability of the HZ for hypothetical Earth-sized planets in extrasolar systems is investigated by dynamical models. Menou and Tabachnik (2003) examined the 85 planetary systems known to the date of their paper and concluded that about a quarter of that sample allows dynamically stable orbits of Earth-sized planets within the HZ, while in about half of the total sample such an orbit was completely forbidden by the known giant planets. Ida and Lin (2004a) studied the different orbital configurations of a hypothetical (and unbiased) sample of planetary systems through Monte Carlo simulations and concluded that the frequency of habitable rocky planets is comparable to the frequency of giant planets. The possibility of an HZ around red giant stars was suggested by Lopez et al. (2005). They find that, even though the duration of the red giant phase is much shorter than the duration of the main sequence phase, solar mass stars could still allow a stable habitable zone during ≈ 1 Gyr, which is more than the time that primitive life needed to develop on Earth. Ikoma and Hidenori (2006) find that rocky planets with masses ranging from 0.3 $M_\oplus$ up to 2–7 $M_\oplus$ (the latter value depending on an uncertain grain formation factor) can form planet-wide oceans by oxidizing the nebular hydrogen.

For the ultimate goal of detection of life, it is necessary to identify observable

bio-markers which, upon detection, could indicate the presence of life. For example, any presence of gas that implies chemical disequilibrium is potentially a biomarker (e.g., abundant O_2 in the presence of CH_4). One of the main difficulties of this approach is the elimination of all the other possible reasons for the chemical imbalance. In that regard, Melott (2004) realized that it is possible to obtain abiotic O_3 (which is considered as one of the key biomarkers for future missions like the Terrestrial Planet Finder, TPF, see §2.2) if the planet has high levels of CO_2. Ehrenreich et al. (2006) discussed the detectability of molecules like H_2O, CO, O_3, or O_2 by transit spectroscopy (see §2.2.2) of an Earth-sized planet. They conclude that such a detection will require a 30–40-m telescope; while for ocean planets, only a 10–20 m telescope is necessary. Seager et al. (2005b) review the use of a surface feature as a biomarker: the vegetation red edge at 700–750 nm, which is observable as an order-of-magnitude-change in the reflectance of leaves. They discuss the earlier observations of Earthshine (Woolf et al., 2002) and warn about the fact that exoplanetary vegetation might not have an edge or have one at a different wavelength from Earth's, as such plants will have optimized the absorption of stellar energy according to the incident spectrum of their own star. Montanes-Rodriguez et al. (2006) present a time-dependent model of the Earth's red edge that includes real land and cloud distributions. They find that under certain realistic observing geometries the feature becomes more prominent than what was observed in Earthshine.

1.1.2 Water as a Molecule

As will be summarized in §2.3, only signatures of elements have been detected in the atmospheres of EGPs. Detection of molecules is much more difficult,

as they do not have isolated strong spectral features, but rather many weak features that blend together to form spectral bands. Hence, for a first molecular detection, it makes sense to focus on a molecule with relatively strong spectral features.

Models indicate that the infrared spectrum of an EGP is dominated by absorption features of water and CO or CH_4 (e.g., Burrows, 2005). Carbon is completely combined into CH_4 at temperatures of 1000 K, but at slightly higher temperatures of $\approx$ 1500 K, CO is the dominant molecule. Since that temperature range contains the typical equilibrium temperatures of close-in EGPs (as defined in §1.2, page 8), any error in the theoretical atmospheric profiles might greatly affect the strength of the absorption bands of CO or CH_4. The water signature, on the other hand, is not sensitive to temperature. It is also expected to have the strongest absorption bands in the IR. However, water might be sensitive to abundance variation. It is possible that if the abundance of C and O is such that C/O $\gtrsim$ 1, then most of the C would combine with O to form CO, leaving little O available to form water (Seager et al., 2005a).

Ground-based water observations have the added difficulty of variable telluric water, probably canceling any observing advantage it might have as a strong absorber.

This dissertation describes the methodology involved in the detection of molecular components in the atmosphere of extrasolar planets and an attempt to detect water in the EGP HD 209458b.

1.2 Extrasolar Planets

Early searches for extrasolar planets around main sequence stars were focused on solar system analogues. Such planets would have typical periods of years, and thus the planet-induced variability in the system's signal would only be detectable after long monitoring. Since long-term monitoring implies a sparse time resolution to be practical, planets with orbital periods of a few days could not have been detected. By tracking a noise source in a radial velocity survey (see §2.1.1), Mayor and Queloz (1995) discovered the first extrasolar planet orbiting a sun-like star (51 Peg). The planet has a period of 4.23 days and thus an unexpected semi-major axis of 0.052 AU. Suddenly, everyone working on extrasolar planet search surveys realized the importance of a finer time resolution, and planets were discovered rapidly.

To this date, about 190 planets orbiting stellar objects (see the Extrasolar Planets Encyclopaedia*) have been identified by four methods: radial velocity, microlensing, pulsar timing, and transit photometry. Figure 1.1 shows all the currently known planets in a mass *vs.* semi-major axis diagram. The most successful method, radial velocity (RV), is limited by the precision by which the Doppler shift can be measured in the stellar spectrum. Recent improvements in the observing techniques have been able to push that limit close to what is necessary to observe a Saturn analogue. Nevertheless, it is evident from Fig. 1.1 that current techniques are sensitive to only a small fraction of the total possible mass-orbital distance configurations. It can also be seen that the upcoming astrometric space missions, like SIM or GAIA (see §2.1.2), will have sensitivity

*http://exoplanet.eu

limits that are very different from RV measurement limits; for example, they will be able to discover all the giant planets in a solar system analogue. Given our greater experience with such a system, we will be more competent to draw conclusions about the possibility of life, among others issues (see §2.3).

Another peculiarity of Fig. 1.1 is the large number of massive planets that are closer to their stars than Mercury is to the Sun. Many planets as massive as Jupiter (including the first known extrasolar planet around a solar type star, 51 Peg, mentioned above) have been discovered orbiting their stars at distances of ~ 0.05 AU. These planets have received various names, ranging from *roasters* and *hot Jupiters* to *class-V* planets (Sudarsky et al., 2003). In this work, they are called close-in extrasolar giant planets (or close-in EGPs). HD 209458b, the planet chosen for this study, belongs to this group. For perspective, Fig. 1.2 shows a representation to scale of the orbital distance of this system. When this project was started in 2002, this was the only known transiting planet; today, another system (HD 189733b) may present better prospects for a successful characterization of its atmosphere (see §6).

The close-in EGPs have been under intense scrutiny, not only because they were completely unexpected from previous theories of solar system formation (e.g., Boss, 1995), but also because they are the most likely to transit (to pass between us and the star, see §2.2). In fact, ten transiting planets are known to this date. Given our current technology, the study of transiting planets is yet the only alternative we have to characterize the planet itself. In §2.3 we indicate the numerous measurements that have been obtained from such planets to this date.

The numerous other properties of the total sample of extrasolar planets have

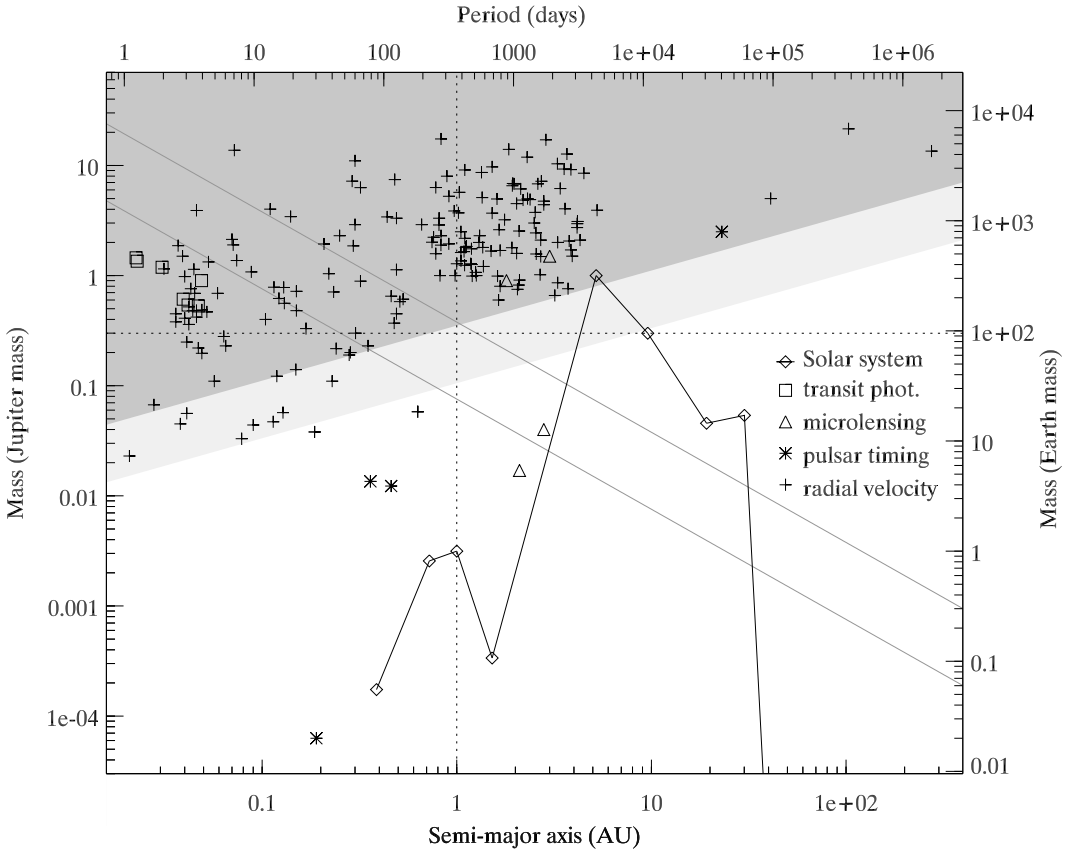

Figure 1.1: Mass-orbital distance diagram for the known planets. The left and right axis are in Jupiter and Earth masses, respectively. The top axis indicates the orbital period corresponding to the value of semi-major axis if the host star had 1 solar mass. The symbols indicate the different methods used to discover the planet. Also shown are the parameter space that the radial velocity and astrometry-based methods can probe on systems whose host stars have one solar mass (see Chapter 2 for more detail. Specifically, see Table 2.2 for the formulas limiting those regions). The solid background area indicates the region that can be probed by radial velocity searches with a sensitivity of 10 m/s (classical limit) and 3 m/s (new precision). The gray diagonal lines indicate the lower boundary of the regions that the astrometric satellite SIM (see §2.1.2) will be able to probe if the system is 10 pc (upper line) and 50 pc (lower line) away. The horizontal dotted line indicates Saturn's mass. The vertical dotted line indicates Earth's distance to the Sun.

Figure 1.2: Diagram of the HD 209458 system with the sizes and distance to scale. The image of the Sun is courtesy of the SOHO/EIT consortium. SOHO is a project of international cooperation between ESA and NASA. Website: http://sohowww.nascom.nasa.gov/

been recently reviewed in detail by Marcy et al. (2005). Some of the most notable trends are summarized below.

Planetary systems are found more frequently orbiting stars with high metallicity (Fig. 1.3). This trend has been carefully studied and sample selection biases have been discarded as a possible explanation (Fischer and Valenti, 2005, 2003). The most recent theoretical work (Ida and Lin, 2004b) justify this trend by an enhanced protoplanetary core formation rate around metal-rich stars.

The metallicity trend provides yet more evidence in favor of the core accretion theory (Laughlin et al., 2004, and references therein) against the competing theory on solar system formation: gravitational instabilities (Boss, 2006, and reference therein). The latter has been unable to explain this trend and other findings such as the massive core of HD 149026b (see §2.3.3).

A *desert* of extrasolar planets is expected to be found between a few and $\sim$ 100 $M_\oplus$ (Ida and Lin, 2004a) due to runaway mass accretion in that range. However, the sensitivity of surveys is just entering that range of masses and no unbiased statistical conclusions can yet be obtained from the observations. The other end of the mass distribution follows a power law $\mathrm{d}N/\,\mathrm{d}M \propto M^{-1.05}$

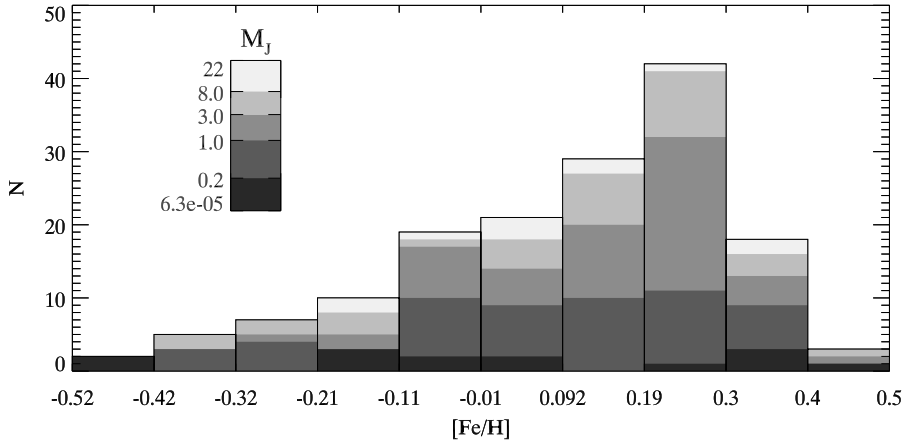

Figure 1.3: Metallicity distribution of extrasolar planets. Each contour represents the metallicity of the host star for the different range of planetary masses as indicated in the inset.

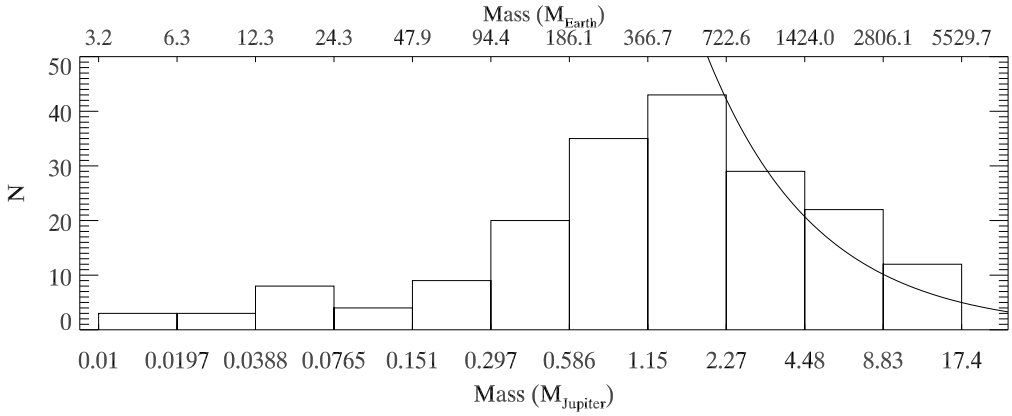

Figure 1.4: Mass distribution of extrasolar planets. Solid line indicates a power law distribution $\propto M^{-1.05}$.

(Marcy et al., 2003).

The range of orbital eccentricities was another of the extrasolar surprises (see Fig. 1.5). In contrast with the predominantly circular orbits of the solar system's planets, the extrasolar eccentricities span the full available range, 0.0– $\sim$ 1.0. As it is expected from tidal circularization, planets in orbits smaller than $\sim$ 0.1 AU have small eccentricities.

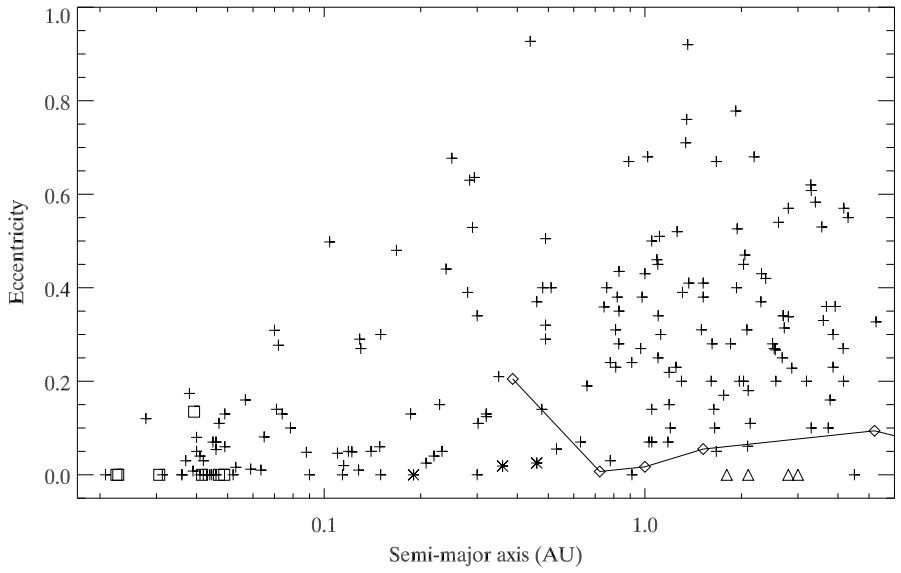

Figure 1.5: Eccentricity *vs* semi-major axis for extrasolar planets. Symbols as in Fig. 1.1.

1.3 Analysis Strategy

This section outlines the chosen approach to the problem of measuring water in HD 209458b's atmosphere. Refer to Fig. 1.6.

The main difficulty for this project is trying to observe water through the Earth's atmosphere, which has water as well. The signature of the telluric water is many times stronger than the signature of HD 209458b's water, and its strength varies on timescales of only minutes. Removal of the telluric water signature and an adequate modeling of the specific water signature of HD 209458b are thus critical to obtain a meaningful result. Then, correlation is employed to compare a synthetic model of the observable quantity (modulation, see §3.1) with spectral data processed under the most optimal methods available to this date.

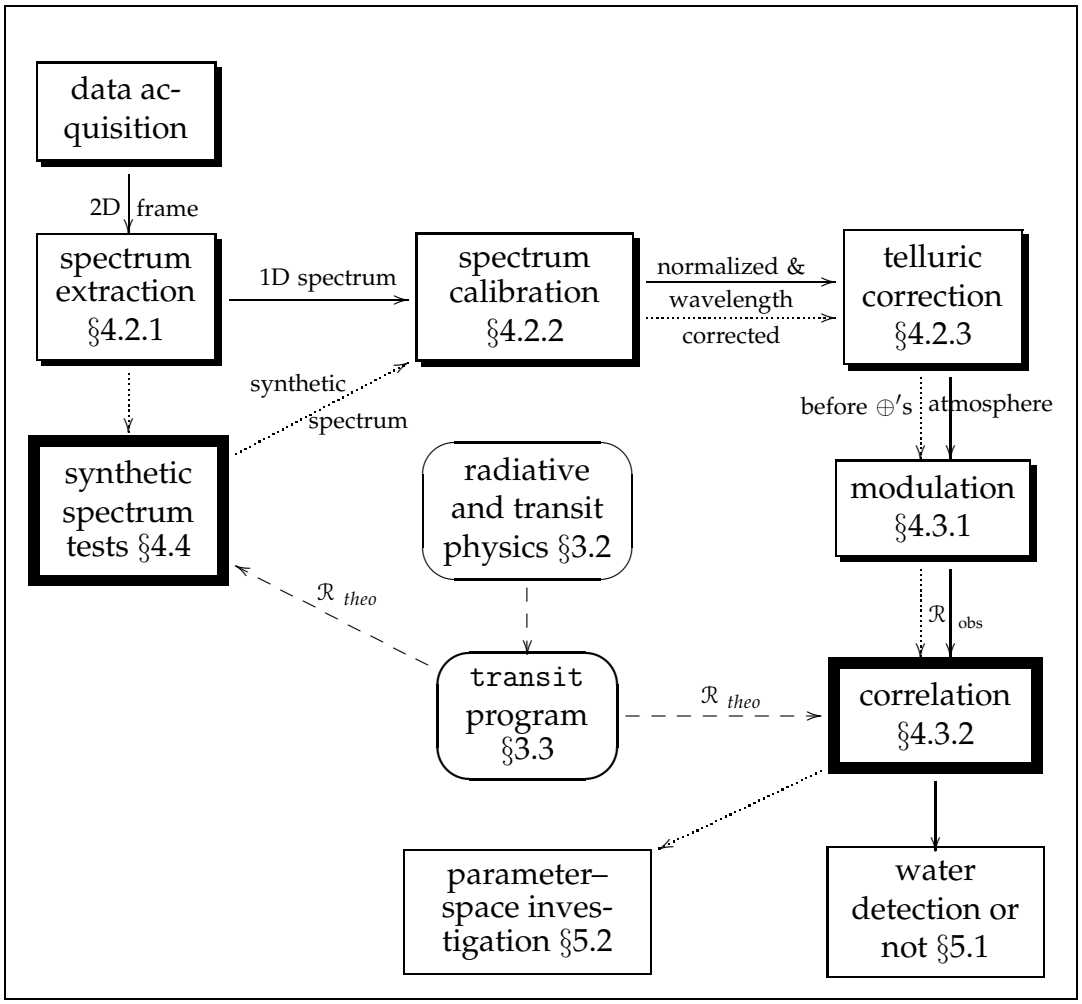

Figure 1.6: Data analysis strategy used for this work. Shadowed boxes indicate data reduction steps, oval boxes indicate the creation of a synthetic spectrum using `transit`, and thick boxes indicate application of the synthetic spectrum to the data. Dotted arrows indicate the path the synthetic spectrum (data + model) follows on the tests, solid arrows indicate the path of the real data, and dashed lines indicate the path of the model data.

This project can thus be divided into two main stages: the modeling of the transit modulation spectrum, and the acquisition and analysis of the data. The former stage, described in detail in §3 (oval boxes of Fig. 1.6), involves the understanding of all relevant physics and its application to a computer model whose main output is the modulation of stellar light due to a transiting planet. For the data acquisition stage, 352 spectra were obtained on 4 photometric nights at the Very Large Telescope (VLT) in Chile. Chapter 4 describes in detail how these spectra were processed to obtain the stellar modulation (shadowed boxes) for the real data (solid arrows) and for a synthetic dataset (dotted arrows). In addition, that chapter details the comparison of the synthetic modulation with the observed data using the correlation method. Finally, Chapter 5 presents and discusses the result: a non-detection with limits on the conditions that would have produced a significant detection. It also discusses a quantitative model of an improved observation strategy that should yield a significant result.

The synthetic dataset is obtained by injecting, early in the reduction stage, the synthetic modulation from our model into the real dataset. This synthetic dataset has a double purpose. First, recovering the injected signal verifies that the pipeline created to analyze the data and detect the modulation is working. Second, scaling the synthetic modulation allows examination of the parameter space for different planetary systems: the confidence levels for successful detections with the different parameters can thus be estimated.

Before the chapters describing this work, Chapter 2 gives a summary of the different methods and results regarding measurements of extrasolar planets.

Methods for Measuring Planets

2

There are several methods, sensitive to different kinds of planetary system configurations, that have been used to detect and measure extrasolar planets. Table 2.1 identifies two alternative groupings of the methods according to the object they aim to observe (star or planet) or what type of observation they use (photometry or spectroscopy). Photometric observations are usually time-series observations where the information is obtained by analyzing the variation of the intensity over time. Spectroscopic observations, on the other hand, yield information by analysis of intensity variation over wavelength (some spectroscopic methods require, in addition, time-series observations of the spectrum).

This chapter presents an updated summary (cf. Charbonneau, 2004) of the methods under consideration by the scientific community for measuring or detecting extrasolar planets as of May 2006. Given the level of activity and the number of new discoveries in the area of extrasolar planets, much of the information presented here will probably be obsolete by the time this is read. An excellent resource, which is constantly kept up to date, is the Extrasolar Planets Encyclopaedia* website maintained by J. Schneider.

Table 2.2 presents 3 fictitious planetary systems that have typical values for one close-in extrasolar giant planet (EGP), a more distant EGP, and an Earth-

*http://exoplanet.eu

Table 2.1: Extrasolar planet detection and measurement methods grouped by either the object they observe (horizontal grouping) or by the type of observations (vertical grouping).

	Spectroscopy	**Photometry**
Purely Stellar Observations	radial velocity §2.1.1	astrometry §2.1.2
		microlensing §2.1.3
		pulsar timing §2.1.4
	observations of chromospheric activity §2.1.5	
Planetary Observations	phase variation §2.2.2	phase variation §2.2.1
	transit §2.2.2	transit §2.2.1
	occultation §2.2.2	occultation §2.2.1
		radio emission §2.2.1

like planet, respectively. This table can be used as reference when precision requirements are discussed in each section.

2.1 Observations of the star

Methods that observe a star have in common that, since they observe the bright host star, they are the best choice when trying to identify previously unknown planetary systems. However, as these methods do not yield much more than the orbital parameters or bulk properties of a planet, follow-up observations to characterize the planet in detail will probably be performed using one of the methods that observe the planet directly, as described in §2.2.

Table 2.2: Parameters of extrasolar planets in three typical conditions. In all cases, they are around a solar-type star with a temperature ($T_\star$) of 6000K, a mass ($M_\star$) of 1 $M_\odot$, with an orbital inclination (i) of 45°, and at a distance (d) of 50 pc from Earth. The table has three horizontal divisions: heading, physical and orbital properties, and magnitude of the effect in some of the methods (the section that discusses each is indicated)

		close-in EGP	distant EGP	Earth-like
system denomination		A	B	C
M_p	mass (M_J)	1	1	3.15×10^{-3}
R_p	radius (R_J)	1	1	0.09
a	distance to star (AU)	0.04	1	1
P	period (days)	2.92	365.25	365.25
A	bond albedo	0.4	0.4	0.4
T_{eq}	equilibrium temp. (K)	1273	255	255
M_{bol}	bolometric magnitude	16.44	23.42	28.65
m_{bol}	apparent bol. magn.	19.93	26.91	32.14
§2.1.1	$RV_\star$ amplitude[a] ($m\ s^{-1}$)	100.46	20.07	0.06
§2.1.2	stellar wobble[b] (μas)	27	668	2
§2.1.4	time lag[c] (sec)	0.026	0.66	0.002
§2.2.1	transit depth[d] (%)	1	1	8×10^{-3}
§2.2.1	refl. occult. depth[e] (%)	1.4×10^{-3}	2.2×10^{-6}	1.8×10^{-8}

[a] amplitude $= \frac{M_p}{M_p+M_\star}\frac{2\pi a \sin i}{P}$

[b] wobble (μas) $= 2\frac{M_p a/M_\star}{d}\frac{180\times3600\times10^6}{\pi}\cos i$

[c] time lag $= 2\frac{aM_p}{M_\star c}\sin i$

[d] depth $= \left(\frac{R_p}{R_\star}\right)^2$

[e] occultation depth $= \frac{A}{4}\left(\frac{R_p}{a}\right)^2$

2.1.1 Radial velocity

When a stellar system has one or more planets, the center of mass will not lie at the center of the star. Consequently, the star will orbit the center of mass (which lies within the star, nonetheless). If the orbital plane of the system is not perfectly perpendicular (face-on) to the line of sight (inclination $i > 0$), there is a radial component to the velocity of the star (RV). Struve (1952) was the first to propose using the Doppler shift of the stellar spectral lines to look for planets (in the same paper, he also proposed searching for planetary transits). The shift is regular, with a period equal to the orbital period, P. The value of the semi-major axis of the orbit, a, and a lower limit to the planetary mass, $M \sin i$, can be obtained using Kepler's laws and geometrical considerations; eccentricity can also be obtained by fitting the shape of the RV curve. These are the only quantities that this method will yield.

By this method alone, it is impossible to determine the value of i. Hence, if their orbital planes were oriented nearly face-on ($i \gtrsim 0$), several of the candidate planets it detects could later be proved to be sub-dwarf companions instead of planets (e.g., Gatewood et al., 2001, Zucker and Mazeh, 2000).

Ever since the first extrasolar planet around a main sequence star was discovered (Mayor and Queloz, 1995), this method has proved to be the most effective in identifying new planetary systems. It has discovered over 90% of the total extrasolar planets known to this date. RV observations are also the first to be made to confirm a tentative new detection from any other method (except pulsar timing and microlensing). Until recently, 10 m s^{-1} has been the limit in the precision to which the velocity could be measured. This permitted the detec-

tion of Jupiter-like planets (see Fig. 1.1). However, recently that limit has been improved, yielding precision as impressive as 2.20 m s^{-1}, which is permitting the discovery of planets with masses of only $\gtrsim 10\ M_{\oplus}$ (Lovis et al., 2006).

There are many ongoing efforts to search for RV variations due to extrasolar planets. A comprehensive list can be found at the Extrasolar Planets Encyclopaedia*. The most successful (by having claimed detection of more than 20 planets each) are: the Anglo-Australian Planet Search team**, the N2K consortium and the California & Carnegie Planet Search Team†, and the searches done with the ELODIE spectrograph††.

2.1.2 Astrometry

If the orientation of the orbital plane is not completely edge-on for a planetary system, then the star will be observed moving back and forth (or wobbling) in the sky as it revolves around the center of mass of the system. The orbital inclination (i) can be determined immediately by geometry and thus, if combined with radial velocity measurements, the exact value for the mass of the planet can be calculated.

The first successful determination of planetary mass using both astrometric and radial velocity measurements was done by Benedict et al. (2002). They used the Hubble Space Telescope (HST) to observe the star's wobble in the sky due to the outermost planet around the star GJ 876. They determined a value for i of $84^{\circ} \pm 6^{\circ}$ and a mass of $1.89 \pm 0.34 M_{Jup}$. Later, the co-planarity assumption

*http://exoplanet.eu

**http://www.aao.gov.au/local/www/cgt/planet/aat.html

†http://exoplanets.org

††http://obswww.unige.ch/∼ udry/planet/elodie.html

among all the planets in that system permitted the announcement of a well-constrained mass of $7.5M_{\oplus}$ in the discovery of the least massive yet of the planets found using the radial velocity method (Rivera et al., 2005).

Measurements with an angular resolution accurate to within 10 or 100 microarcseconds (μas) is a practical requirement for astrometric discovery of extrasolar planets (see Table 2.2). Interferometers and space telescopes are thus the best means to carry out these observations. In fact, the Space Interferometry Mission (SIM)* is an important project from the National Aeronautics and Space Agency of the United States (NASA), originally scheduled to launch in 2011 but postponed until no earlier than 2015 due to recent budget developments. The SIM mission will monitor the position of stars to an accuracy of 1.44 μas, several hundred times more accurately than any previous observations. SIM will be able to probe previously inaccessible system configurations; for example, it will be sensitive to all the giant planets of many solar system analogues (see the grey diagonal lines in Fig. 1.1). Another astrometry project with ambitious goals is the European Space Agency's (ESA) project GAIA**, a spacecraft scheduled to launch in 2011. Current design requirements estimate a precision of 10–20 μas.

As an alternative to space-based observations, Lazorenko (2006) argues that astrometric measurements with current ground-based large telescopes, under optimal reduction, are never atmosphere-limited. In particular, observation with FORS2 at the VLT could reach the necessary precision of 30–50 μas.

*http://planetquest.jpl.nasa.gov/SIM/

**http://www.esa.int/esaSC/120377_index_0_m.html

2.1.3 Microlensing

As first pointed out by Einstein (1936), when a massive object passes in front of or very close to a projected background light source, some of the light that originally was not directed towards the Earth is gravitationally bent, producing a lens-like effect. When there are two or more foreground objects, the gravitational interaction produces areas called caustics in the projected plane perpendicular to the line of sight. If light from the background source passes through one of the caustics as the foreground objects move in front, the intensity is magnified several times more than it would be if the foreground object were a single mass (e.g., Udalski et al., 2005).

The frequency of lensing events in the galactic disk is so small that it was never considered a viable alternative until Paczynski (1986) realized that the galactic halo would contain many objects that would produce frequent events if an area with a high density of stars (like the Magellanic clouds or the galactic center) is used as background.

This method is not constrained by the distance to the objects or the orbital inclination. However, microlensing events are one-time events and do not give any information about the orbit of the system, nor is it guaranteed that there could be any follow-up observations. There is also a chance that the two bodies that are causing the caustic are not part of the same system, but just happen to lie along the same line of sight to the background source.

Four planets in four microlensing events have been discovered to this date: OGLE235-MOA53 b (Bond et al., 2004), OGLE-2005-BLG-071 (Udalski et al., 2005), OGLE-2005-BLG-169 (Gould et al., 2006), and OGLE-2005-BLG-390Lb

(Beaulieu et al., 2006). The events were picked up by the Optical Gravitational Lensing Experiment (OGLE) early warning system, which was able to predict, with several days' advance notice, the moment of maximum magnification (the moment when the background source is most likely to pass through one of the caustics if there are multiple foreground objects). As that time approaches, observations are carried out much more frequently, by different teams, and from several telescopes around the globe, in order to obtain continuous coverage. If more than a single magnification peak is observed, then necessarily, the foreground object is not a single mass. Detailed modeling of the shape of the magnification curve yields an accurate mass ratio between the objects.

Teams like the OGLE* collaboration, MACHO**, MPS†, μFUN††, and MOA‡ monitor thousand of background light sources in the direction of the Magellanic clouds or the galactic center in search of microlensing events.

2.1.4 Pulsar timing

Years before the first detection of an extrasolar planet around a main sequence star, the first planet outside the solar system was discovered orbiting a millisecond pulsar (Wolszczan and Frail, 1992). The discovery was made possible by analyzing the small deviations from the otherwise perfectly periodic pulses from the pulsar. The tiny variations are caused because photons take a longer or shorter time to arrive at Earth when the pulsar (pulled by the planet) moves

*http://www.astrouw.edu.pl/∼ ogle/
**http://wwwmacho.mcmaster.ca/
†http://www.nd.edu/∼ srhie/MPS/
††http://www-astronomy.mps.ohio-state.edu/∼ microfun/
‡http://www.phys.canterbury.ac.nz/moa/

farther from or closer to us, respectively. The technique yields the same upper limit on the planetary mass as the radial velocity method: $M \sin i$.

Only two planetary systems around pulsars have been discovered to this date (Wolszczan and Frail, 1992, Backer et al., 1993). One of them, the system around pulsar PSR 1257 + 12, is a three-planet system that contains a minute planet that has only 0.015 times the mass of Earth. The discovery of such a small planet (Wolszczan, 1994) was only possible because the pulsar has a very stable period of 6.2 ms, which permitted a precision of 3 μs over the 3-year span of the observations.

2.1.5 Planet-induced chromospheric activity

Close-in giant planets are expected to considerably perturb the star gravitationally and magnetically. Magnetic perturbations will produce observable effects with the same period as the orbital period, P. On the other hand, the gravitational (tidal) perturbation produces observable effects with a characteristic period equal to half of the orbital period: $P/2$. Cuntz et al. (2000) investigated, for the first time, the different possible interactions between the planets and the surfaces of the host stars. They compare the relative strength of the different effects and suggest, among 12 selected planetary systems known to that date, those that are the best candidates in which these effects could be detected.

The height of the tidal bulge produced by the gravitational interaction is only a few percent of the photospheric scale height (Cuntz et al., 2000) (solar photospheric scale height $\approx$ 70 km). Nonetheless, tidal interaction also produces enhanced flows and turbulence which, in turn, produce magnetoacoustic heating and affect the dynamo action. The magnitude of the magnetic interac-

tion is very difficult to model precisely, but it produces a hot-spot on the stellar surface with the period of the planet. The light curve will have a characteristic shape.

Saar and Cuntz (2001) report the first systematic search for a periodicity that could be attributable to a companion body, by monitoring the strength of the chromospheric Ca II triplet in 7 systems. They identify only one instance, the τ Boo system, where they find that the variability of the triplet could be due to magnetic effects (22% false alarm probability). Photometric observations used by Henry et al. (2002) to declassify HD 192263 as a planet were later proposed to correspond to magnetic (and maybe even tidal) interactions on the surface of the star (Santos et al., 2003). Shkolnik et al. (2003) monitored 5 close-in EGP over more than a year. They find the first strong detection of planet-induced enhancement in Ca II H and K emission on HD 179949. This enhancement is coincident in period with a magnetic interaction from the planet, has a magnitude of 4% of the total stellar flux, and has a phase lag of 60° with respect to the orbital period. Later, Shkolnik et al. (2005), with a longer time span, confirmed the planet-induced effect on HD 179949 and added a strong detection for υ And with a phase lag of 169°. They could not detect any signal from τ Boo, which they attribute to tidal locking of the planet that leaves less free energy available from the planet's orbit.

Ip et al. (2004) model the magnetic interaction between a planet and its star. They present results from a magnetohydrodynamic (MHD) model, which agrees with the scenario, proposed by Rubenstein and Schaefer (2000), in which the planet could provoke strong magnetic flares if the magnetic fields of both bodies present a favorable orientation. Such energy would be directed into the

planet's ionosphere, increasing the temperature drastically, and thus contributing to massive atmospheric loss (as the one observed in HD 209458b by Vidal-Madjar et al., 2003, see §2.3). Shkolnik et al. (2005) were able to explain the lag of the magnetically induced period in HD 179979 by postulating an appropriate magnetic axis alignment, but were unable to explain the larger phase lag of υ And.

2.2 Observations of the planet

The apparent magnitude of typical EGPs is within the capabilities of current telescopes (see Table 2.2). Chauvin et al. (2005) have even reported the first direct detection of a planetary-mass companion (5 M_J, though this figure is controversial) orbiting a brown dwarf at a distance of more than 50 AU. However, the orbital separations of systems around main-sequence, sun-like stars, which are much brighter, cannot be resolved spatially. The small planet-to-star flux ratios (bottom frame, Fig. 2.1) make it impossible to attain static data (like one-time observations) from the planet (see Lucas and Roche, 2002, for one such attempt).

An ambitious project from NASA, the Terrestrial Planet Finder (TPF)*, is being designed to separate the light from the star spatially. Currently, the project consists of two telescopes to be launched sequentially: the first telescope will use a coronograph to mask out the light from the star, and the second will use optical interferometry. However, the launch date has recently been postponed indefinitely (probably to no earlier than 2020). ESA is also planning an equiva-

*http://planetquest.jpl.nasa.gov/TPF/

lent mission, which is called Darwin*. Its current design consists of a flotilla of 3 telescopes, which will use interferometry to cancel out the light from the star. It is scheduled to launch in 2015.

Current efforts are focused on the detection of periodic variability. The stellar flux is constant or, hopefully, has only small, quasi-random fluctuations. Therefore, any periodic variability will be due to the planet as it orbits the star. Other than the smooth changes that should occur for all planets as they orbit and the planet-induced chromospheric activity discussed in §2.1.5, there are up to two other orbit-related instances that produce changes in the flux from a single-planet system. They are when, with respect to Earth's line-of-sight, the planet passes in front of (transit) or behind (occultation) the star. Not all the systems have the appropriate geometry; those that have it are called transiting planets. Considering a random orientation of orbits, the probability that a planet with an eccentricity, e, stellar radius, $R_\star$, and orbital semi-major axis, a, will transit its star is given by (Charbonneau et al., 2006a):

$$P_{\text{transit}} = 0.0045 \left(\frac{1\ \text{AU}}{a}\right) \left(\frac{R_\star + R_p}{\text{R}_\odot}\right) \left[\frac{1 + e\cos\left(\pi/2 - \varpi\right)}{1 - e^2}\right]. \qquad (2.1)$$

It is clear that, with the above equation, the sample of transiting planets will be biased toward close-in planets orbiting host stars with large radii.

In part because these drops in intensity are much more abrupt than the variation due to orbital phase, they present the best opportunity to obtain information on the planet's composition and internal structure. The plethora of information from the 10 known transiting planets is summarized in §2.3, after this discussion of measurement methods.

*http://sci.esa.int/science-e/www/area/index.cfm?fareaid=28

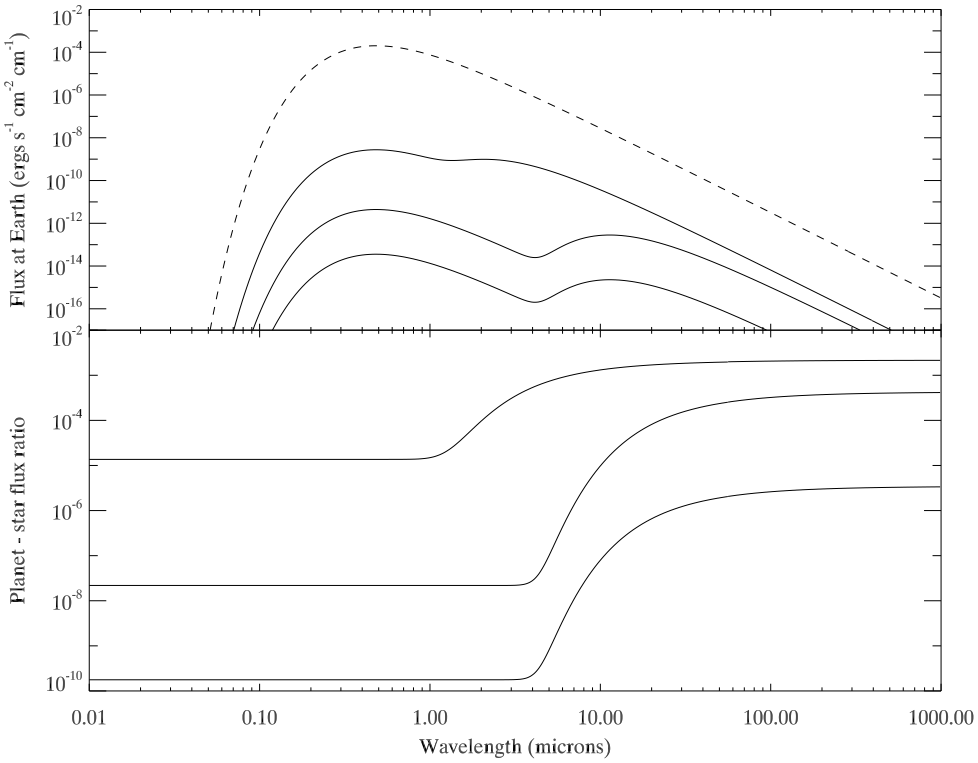

Figure 2.1: Sample blackbody curves for the nominal planets from Table 2.2. *Top*: Received flux from the star (dashed curve) and from each of the planets' illuminated hemispheres (solid curves; planets A to C, from top to bottom). Note that the planets have two peaks, which correspond to maximum of the reflected emission (leftmost peak) and the maximum of the thermal emission (rightmost peak). *Bottom*: Planet-to-star flux ratio. Note that blackbody curves are crude approximations to the real system emissions, especially in the infrared where molecular absorptions dominate.

There are two bright sources of radiation from the planet: reflected light and thermal emission. The former is light reflected from the star and thus it usually peaks at optical wavelengths. The latter is the radiation the planet emits and it is dominant at IR wavelengths. The top panel of Fig. 2.1 shows the blackbody-curve approximations to the emission and reflection for our nominal planets from Table 2.2. In all cases the planet-to-star ratio is more favorable in the IR (beyond ~ 5 μm) where the thermal emission dominates. Note that the longer

the wavelength, the dimmer the system becomes, and the more difficult it is to attain the required signal-to-noise ratio (SNR) in the observations. A more precise model of the received radiation would include molecular and atomic lines, and a wavelength-dependent geometric albedo. These considerations would affect the blackbody curves by orders of magnitude in certain spectral regions (e.g., Burrows, 2005, Seager et al., 2005a, Sudarsky et al., 2003, Marley et al., 1999).

The blackbody temperature is given by the equilibrium temperature (T_{eq}) of the planet, which is defined as the temperature at which the energy emitted from the planet is in equilibrium with the energy incident from the star. For blackbodies, the total flux is proportional to the fourth power of the temperature ($F = \sigma T^4$, where σ is the Stefan-Boltzmann constant). Then,

$$\begin{aligned} E_{\text{emitted}} &= E_{\text{incident}}, \\ \sigma T_{eq}^4 4\pi R_p^2 &= \sigma T_\star^4 4\pi R_\star^2 (1-A)\frac{1}{4\pi a^2}\pi R_p^2, \text{ and} \\ T_{eq}^4 &= \frac{1-A}{4}\left(\frac{R_\star}{a}\right)^2 T_\star^4, \end{aligned} \tag{2.2}$$

where a is the semi-major axis of the orbit, A is the albedo, and $R_\star$ and $T_\star$ are the stellar radius and temperature, respectively. Consequently, the total (wavelength-integrated) thermal flux (f_T) will be given by

$$\begin{aligned} F_T &= \sigma T_{eq}^4 \pi R_p^2 \frac{1}{4\pi d^2} \\ &= \frac{1-A}{4}\left(\frac{R_\star}{a}\right)^2 \sigma T_\star^4 \pi R_p^2 \frac{1}{4\pi d^2} \\ &= \frac{1-A}{4}\left(\frac{R_p}{a}\right)^2 F_\star \end{aligned} \tag{2.3}$$

where $F_\star$ is the bolometric stellar flux.

The reflected light flux per wavelength is given by

$$f_{rl} = \underbrace{I_{0\star}\frac{2\pi}{a^2}\int_0^{R_\star} B(R)R\,\mathrm{d}R}_{\substack{\text{stellar flux}\\ \text{at the planet}}} \cdot \underbrace{\pi R_p^2 A}_{\substack{\text{fraction}\\ \text{intercepted}\\ \text{and reflected}}} \cdot \underbrace{\frac{1}{4\pi d^2}}_{\substack{\text{inverse}\\ \text{square law}\\ \text{fall off}}} \cdot \underbrace{p(\alpha)}_{\substack{\text{geometric}\\ \text{factor}}}$$

$$= \frac{A\ p(\alpha)}{4}\left(\frac{R_p}{a}\right)^2 I_{0\star}\frac{2\pi}{d^2}\int_0^{R_\star} B(R)R\,\mathrm{d}R$$

$$= \frac{A\ p(\alpha)}{4}\left(\frac{R_p}{a}\right)^2 f_\star, \tag{2.4}$$

where $p(\alpha)$ is the phase function and $f_\star$ is the wavelength-dependent stellar flux at Earth.

Close-in EGPs present the best candidates for both reflected and thermal emission observations, since both Eqs. (2.3) and (2.4) are directly proportional to the square of the planetary radius and inversely proportional to the square of the distance to the star.

2.2.1 Photometric observations

Photometric observation of electromagnetic radiation that has directly interacted with the planet has the potential of yielding more detailed information than just the bulk properties found by measuring the star (§2.1). Furthermore, it is very easy to monitor several stars at once with a wide-field-of-view telescope.

There is one space telescope already in orbit and two more upcoming missions designed exclusively for high precision photometry. The Canadian Microvariablity and Oscillations of STars (MOST)* satellite has been in orbit since

*http://www.astro.ubc.ca/MOST/

June 30, 2003. It does not possess survey capabilities but is capable of monitoring an area for 60 days uninterruptedly. A full review of the capabilities of MOST that are relevant to planetary photometry has been given by Green et al. (2003). However, to this date, only one publication (Rowe et al., 2006) has given any result about an extrasolar planet (see below under *Photometric phase variation*). ESA's COROT telescope* is a 30-cm space telescope scheduled to launch in October 2006. It will observe starquakes and survey at least 200,000 stars, in search of transit light curves in stars brighter than magnitude 15.5. COROT is expected to be sensitive to rocky planets several times larger than Earth. Then, the NASA Kepler** mission is scheduled to launch in October 2008. This 1.4-m space telescope will be dedicated to monitor a small area in the solar neighborhood encompassing 100,000 stars for 4 years. This telescope is eagerly awaited, as it will be sensitive to transit curves produced by Earth-size planets and is expected to find thousands of them.

Photometric phase variation

As a planet moves around its orbit, it constantly presents different faces to the Earth.

In the regime of reflected light, this means that different amounts of the hemisphere illuminated by the star are visible to us. This effect is quantified by the phase function, p (Eq. 2.4). In contrast, the emitted light's phase variability depends on more factors than just observing geometry. A fast rotator or a planet with very strong winds will move heat very efficiently from the illuminated hemisphere to the dark hemisphere. On the other hand, close-in EGPs are

*http://www.esa.int/esaSC/120372_index_0_m.html

**http://kepler.nasa.gov/

expected to have marked day-night differences because of the level of irradiation and their anticipated tidal locking(e.g., Cooper et al., 2003, Guillot, 2005, Cho et al., 2003).

The phase curve and its dependence on wavelength has been studied by many groups (Marley et al., 1999, Seager et al., 2000, Sudarsky et al., 2003, Barnes and Fortney, 2004, Arnold and Schneider, 2004, Dyudina et al., 2005, Sudarsky et al., 2005). Of the most recent ones, Sudarsky et al. (2005) study the phase curve for widely separated planets. They find that its shape strongly depends on the presence of clouds and the sizes of their particles, as scatter is only strong in planets with high-altitude clouds (low-gravity planets). Dyudina et al. (2005) simulate the expected curves for extrasolar Jupiters and Saturns considering different conditions like eccentricity and, for the first time, anisotropic scattering. They also investigate the effect of rings and find that Saturn-equivalent structures could potentially increase the apparent luminosity of a planet by a factor 2–3, and that such structures could be detected by asymmetries in the light curve. The latter result is in agreement with Barnes and Fortney (2004): both groups expect rings to be detectable in reflected light with future space telescopes like Kepler.

Using close-in EGP statistics and Monte Carlo tests, Jenkins and Doyle (2003) assert that on its 4-year mission, Kepler will detect, with no more than one false alarm, between 100 and ~ 760 new close-in EGPs by reflected light (depending on the presence, composition, and structure of clouds).

Transit photometry

When a planet passes in front of its star as seen from Earth, it blocks a fraction of the stellar light proportional to the ratio of projected areas. The corresponding drop in intensity is abrupt; thus, it is much easier to detect than the smooth phase change discussed in the previous section.

A light curve of such an event will produce a drop in intensity for a fixed period of time that would have the following properties: (1) it will fall and rise symmetrically (except maybe if there are satellites or rings to the planet, Barnes and Fortney, 2004), (2) the frequency with which the intensity drop occurs is constant, (3) the in-transit and out-of-transit intensity levels will be fixed even after many orbits, and (4) the ingress/egress curve shape is determined by the limb-darkening law and orbital inclination. Even if a lightcurve fulfills the previous conditions, it could still be a false positive (e.g., a white dwarf could be producing the drop in intensity instead of a planet). Radial-velocity follow-up observations are thus necessary to confirm whether a planetary system was discovered or not. The rate of false positives is significant. For example, the OGLE collaboration (while looking for microlensing events) identified 177 transit-like light curves among the stars used as background objects after their 2003 campaign; however, only 5 of these systems were later confirmed as having planets (see §2.3). Nevertheless, transit photometry has been the only method outside the purely star-observing methods described in §2.1 that has reliably identified previously unknown planets.

The planetary radius and orbital inclination share a degeneracy: the curve produced by a planet transiting closer to the limb of one star could be equal to the curve produced by a planet transiting closer to the center of a smaller

star. As recognized by Jha et al. (2000), this degeneracy can be broken if multi-wavelength photometry is simultaneously used to fit limb-darkening in the transit curve. Then, the only uncertainties remaining in these values come from uncertainties in the stellar parameters, which are thought to be constrained by mature theory, with a 10% error (e.g., Sato et al., 2005).

Miralda-Escudé (2002), Holman and Murray (2005), and Agol et al. (2005) analyze the effect that an unseen companion will have in the timing of a sequence of transit events. They argue that this variation could lead to detection of Earth-like systems.

Benefits of having a transiting extrasolar planet do not stop with the attainment of the radius and an unambiguous mass. Below and in §2.2.2, we discuss how to obtain information about internal composition and physical structure of the planet (see also Charbonneau et al., 2006b, for more details on the importance of transiting planets).

Occultation photometry

Approximately one half orbit after it passes in front of its star, a transiting planet might pass behind its star (secondary eclipse, occultation) and give another opportunity to detect an abrupt change in the intensity received from the system. The relative timing of the events and whether the planet will have both eclipses or not depends on the orbital eccentricity and the argument of pericenter.

Occultation photometry is different from transit photometry in a fundamental way. The latter is sensitive to the size of the planet, and is basically independent of the planet's reflected light or emitted intensity (except indirectly, as a hotter planet will evolve to a planet with a bigger radius, Chabrier et al., 2004).

Occultation photometry, on the other hand, is the best alternative to detect light from the planet as the system changes in view abruptly from having an almost fully illuminated planet to a system without a planet. Hence, even though the secondary eclipse is much weaker than the primary eclipse, it has the potential to give much more photometric information.

Occultation observations in the thermal regime constrain planetary temperature and Bond albedo, as was the case for HD 209458b, TrES-1, HD 189733b and HD 149026b (Deming et al., 2005b, Charbonneau et al., 2005, Deming et al., 2006, Harrington et al., 2006). On the other hand, occultation observations in the reflected regime constrain the visible albedo, as was the case for HD 209458b once again (Rowe et al., 2006). More details on these measurements are in §2.3.

Radio emission

Other than reflected star light and thermal emission, the giant planets of our solar system present strong auroral-related radio emission. Hence, since long before the first extrasolar planet discoveries, searches for such emission have been carried out (Winglee et al., 1986). Mechanisms responsible for these emission have been discussed in detail by Farrell et al. (1999), Bastian et al. (2000), Zarka et al. (2001), Sánchez-Lavega (2004) and Stevens (2005). For close-in EGPs, they expect the power of such emissions to be 1000 times stronger than Jupiter's, and thus potentially detectable.

The periodicity in a successful detection of radio emission would directly determine the planetary rotational period and even indicate the presence of planetary satellites. In addition, intensity and polarization measurements will constrain several magnetic parameters of the system (Bastian et al., 2000).

Farrell et al. (2003) and Bastian et al. (2000) performed searches for radio emission from extrasolar planets, but they were only able to place upper limits. Recently, Stevens (2005) presented a new analysis with an updated stellar wind model. They list new, promising candidates to search for radio emission.

2.2.2 Spectroscopic observations

Spectroscopic observations have the potential to yield much more information than photometric observations: the former yields an entire spectrum where the latter yields one data point. But, for that same reason, they are much less sensitive per point and each observation is much more expensive in telescope time since, traditionally, only one star at a time can be observed.

Recently, the use of integral field spectroscopy* (IFS) has been proposed to observe extrasolar planets (Arribas et al., 2006). The IFS technique consists of simultaneously observing a two-dimensional (2D) field of the sky by redirecting the light through lenses, fiber optics, or mirrors towards the same detector array, such that the spectral dispersion direction from the different areas in the 2D field is arranged in parallel on the detector array.

As suggested by Gilliland et al. (1999), for the Space Telescope Imaging Spectrograph (STIS) on the HST, a spectrograph can be used to spread the number of photons from a source over the array. Thus, by simply binning channels across wavelengths, a photometric (or lower-resolution spectroscopic) data array can be obtained at a higher SNR (for photon-limited observations) than if such resolution had been used since the beginning. This concept can be extended us-

*For a more comprehensive description of IFS, see the webpage of Jeremy Allington-Smith: http://star-www.dur.ac.uk/$\sim$ jra/integral_field.html

ing integral field spectroscopy, where the stellar photons are not only spread in wavelength but also in the spatial direction, using a defocused star and an image splicer (Berton et al., 2006).

For extrasolar planets, this technique is particularly useful when the host star is very bright, as it makes it possible to have longer integration times without saturating the array. Another benefit of the technique is that the efficiency of the spectroscopic observation will be less affected by changes in seeing, since the light from the defocused star will just be captured by a neighboring spatial channel. The spectrographs of the new generation of space telescopes will all be equipped with this capability. Among them, the James Webb Space Telescope (JWST)* project from NASA, a space telescope with a main mirror of 6.5 m (cf. Hubble Space Telescope's 2.4 m), is scheduled to be launched no earlier than June 2013.

Spectroscopic phase variation

The periodic Doppler amplitude of the planetary spectral lines is larger than that of the star (it scales proportionally to the mass ratio). Hence, in principle, planetary spectral lines could easily be differentiated from stellar spectral lines by their greater amplitude and the 180° phase offset with respect to the shift of the stellar lines.

To this date, however, the many high-resolution spectroscopic searches for reflected (Charbonneau et al., 1999, Collier Cameron et al., 2002, Leigh et al., 2003b,a) or thermal (Wiedemann et al., 2001) emission have yielded no detections yet. The latter do find a signal consistent with a planet, but it is only 2.4σ

*http://www.jwst.nasa.gov/

above the noise level.

Transit spectroscopy

Transit spectroscopy of HD 209458b has so far been the only successful method of obtaining information about atmospheric composition. It is based on the fact that radiation at some wavelengths penetrate deeper into the exoplanetary atmosphere than at other wavelengths. This translates to a wavelength dependence of the planetary area, which is observable as the light from the star is blocked.

This is the chosen method for this project and it is thus explained in detail in Chapter 3. The measurements this method has made possible are discussed in §2.3.

Occultation spectroscopy

Occultation spectroscopy has the potential to yield important information about planetary structure analogous to the information we obtain by directly looking at the planets in our solar system. Richardson et al. (2003a,b) obtain upper limits on the strength of CO, CH_4, and H_2O absorption bands of HD 209458b with this technique.

The James Webb Space Telescope will be capable to attain the required sensitivity for occultation spectroscopy

2.3 Transiting planets

Given the importance of transiting planets, the current knowledge of the 10 transiting extrasolar planets known to this date is discussed in this section.

The OGLE team identified more than 170 transiting planet candidates while they were monitoring the stars they selected as background sources for their microlensing experiments (Udalski et al., 2002a,b, 2003). Of them, only five were later confirmed as planetary systems by spectroscopic follow-up: OGLE-TR-56 (Konacki et al., 2003), OGLE-TR-113 and OGLE-TR-132 (Bouchy et al., 2004), OGLE-TR-111 (Pont et al., 2004), and OGLE-TR-10 (Konacki et al., 2005). However, all of these planets are at a distance close to 1500 pc from Earth and are thus very unfavorable candidates for follow-up studies.

The other five known planets have been under intense study. Below, the most important measurements done on each of these systems are discussed. What is not discussed is the characteristics of the many other projects underway that attempt to discover transiting extrasolar planets (for a good summary, refer to Pepper and Gaudi, 2005).

Some early estimates regarding the success of planetary searches by transit photometry (e.g., Horne, 2003, who expected some 10–100 new transiting planets every month) were greatly overestimated, partly due to the overwhelming number of false positives per confirmed transiting planet. Only the five planets detected by OGLE and two other planets, TrES-1 (Alonso et al., 2004) and just recently XO-1b (McCullough et al., 2006), were initially identified by transit photometry. Tingley and some collaborators have been developing, in a series of papers (Tingley, 2004, Tingley and Sackett, 2005, Tingley et al., 2006), a color photometry method that will allow quick discrimination of a planetary transit against binary star transits or blends. This, along with other new criteria and new telescopes like Kepler, should make the photometric-transit method more efficient at discovering new planets. Hence, maybe the era of frequent discov-

eries of these important planets is still just around the corner.

2.3.1 HD 209458b

The first planet discovered to transit its star was HD 209458b. It was discovered almost simultaneously by two groups doing independent radial velocity surveys at the end of the last century (Mazeh et al., 2000, Henry et al., 2000). Follow-up observations (again by two independent groups) confirmed, for the first time, a photometric transit by an extrasolar planet (Charbonneau et al., 2000, Henry et al., 2000). The importance of this discovery was immediately recognized: radius, inclination, and even atmospheric composition of an extrasolar planet could now be measured.

The most recent physical parameters for the planet and the star are summarized in Table 2.3. Knutson et al. (2006) obtained 1066 medium-resolution ($\Delta\lambda/\lambda = 1500$) spectra from the STIS spectrometer on the HST during four transits. They binned their result in ten spectrophotometric bandpasses and made simultaneous fits to the planet's radius, the stellar limb darkening, and the inclination. By using a multi-wavelength fit, they broke the degeneracy between radius and inclination and obtained a mass of 1.320 ± 0.025 M_J, which is a factor of two more precise than, but in agreement with, previous work (Wittenmyer et al., 2005, Winn et al., 2005, Richardson et al., 2005).

Once the inclination is obtained, the ambiguity in the mass determination from radial velocity measurements disappears. Scaling the mass obtained by Laughlin et al. (2005b) with the inclination obtained by Knutson et al. (2006), a value of 0.656 M_J and, consequently, the unusually low density of 0.378 g cm^{-3} are obtained. HD 209458b has a density that is unaccountably low (OGLE-TR-

Table 2.3: Measurable parameters of the HD 209458 system. Uncertainties are in parentheses and refer to the last digits in the value.

Parameter	Value	Uncert.	Reference[a]
planetary radius (R_J)	1.320	(25)	a
planetary mass (M_J)	0.657	(6)	a+c
inclination (°)	86.929	(10)	a
period (days)	3.52474859	(38)	a
ephemeris time (JD)	2452826.628521	(87)	a
orbital eccentricity	0.018	(9)	d
Bond albedo	$\lesssim 0.375$		e
semi-major axis (AU)	0.04680	(14)	from above
gravity (cm s^{-2})	974	(9)	from above
density (g cm^{-3})	0.378	(3)	from above
equilibrium temperature (K)	$\gtrsim 1285$		from above
scale height (km)	$\gtrsim 475$		from above
stellar radius ($R_\odot$)	1.125	(23)	a
stellar mass ($M_\odot$)	1.101	(66)	a
stellar temperature (K)	6117	(26)	b
stellar gravity (cm s^{-2})	4.48	(8)	b
stellar [Fe/H]	0.02	(3)	b
apparent V magnitude	7.645	(2)	f
apparent H magnitude	6.366	(35)	g

[a]References. a: Knutson et al. (2006); b: Santos et al. (2004); c: Winn et al. (2005); d: Laughlin et al. (2005b); e: Rowe et al. (2006); f: Hipparcos catalogue (ESA, 1997); g: 2MASS catalogue (Skrutskie et al., 2006).

10b and XO-1b's densities are also low, to a lesser degree, see Fig. 2.2). The density of all the other known EGPs can be explained by an evolutionary history governed by intense radiation from the star, which prevents an efficient cooling and contraction (Burrows et al., 2000, Guillot, 2005). However, no single theoretical explanation is yet fully satisfactory in explaining the large size of HD 209458b. Showman and Guillot (2002) argue that if at least 1% of the incident radiation is converted completely into strong winds, then the downward transport of energy could explain the observed radius of HD 209458b. However, there does not seem to be any reason why these winds would not occur on all hot Jupiters. Energy liberated by tidal dissipation of an eccentric orbit has also been postulated (Bodenheimer et al., 2001, 2003). However, observational constraints from the RV measurements (Laughlin et al., 2005b) and the timing of the secondary eclipse (Deming et al., 2005b) are consistent with an eccentricity of 0.018 ± 0.009, which is too small for a structurally significant tidal heating of the planet. If the eccentricity changes in time by interaction with a yet-undetected companion (Bodenheimer et al., 2001), then this could be detectable as short-term oscillations in the timing of transits (Miralda-Escudé, 2002, Holman and Murray, 2005, Agol et al., 2005). A third alternative was proposed by Winn and Holman (2005). They suggest that sufficient energy to explain the extended radius will be available if the planet is in a particular Cassini state, where spin precession resonates with the orbital precession. If this is the case for HD 209458b, the evolution of this state throughout the system's age implies that the spin axis is now tilted close to 90° with the normal of the plane of the system. However, a measurement of the oblateness, which could prove this theory, is beyond current instrument capabilities (ingress/egress curves would be

different from those of a circular planet by a factor of $\approx 10^{-5}$, Seager and Hui, 2002). If the spin axis of HD 209458b is as inclined as predicted by this theory, the atmospheric temperature distribution could differ significantly from what current models predict. Another theory by Burrows et al. (2003) tries to explain the radius only by proper irradiation in an evolutionary model, but it fails to agree with the most recent measurements of the radius. Baraffe et al. (2004) suggest that HD 209458b has a very small probability to be in an evolutionary stage with a very short lifetime where the planet is evaporating violently. Their model fits the observed parameters and age of HD 209458b, but they warn that we must be very lucky to see such a short-lived phase.

Recently, Rowe et al. (2006) reported measurements made with the MOST* satellite that allowed the placement of an upper limit of 0.375 to the Bond albedo of HD 209458b. They found this value by comparing with models and extrapolating from a wavelength-dependent single albedo, which is what can be inferred directly from MOST measurements.

HD 209458b transit spectroscopy has yielded the first detections of an exoplanetary atmosphere's constituents. Na I was the first element to be detected, at a 4σ significance level using HST's STIS spectrograph (Charbonneau et al., 2002). The level of the signal was three times lower than expected. Several alternative scenarios have been postulated to explain this discrepancy, most importantly the presence of high clouds, which would truncate the amount of atmosphere probed by transmitted stellar rays (for a complete review of the different explanations see Seager, 2003). In contrast to the low value of the Na I detection, Vidal-Madjar et al. (2003), using the same instrument, claims a de-

*http://www.astro.ubc.ca/MOST/

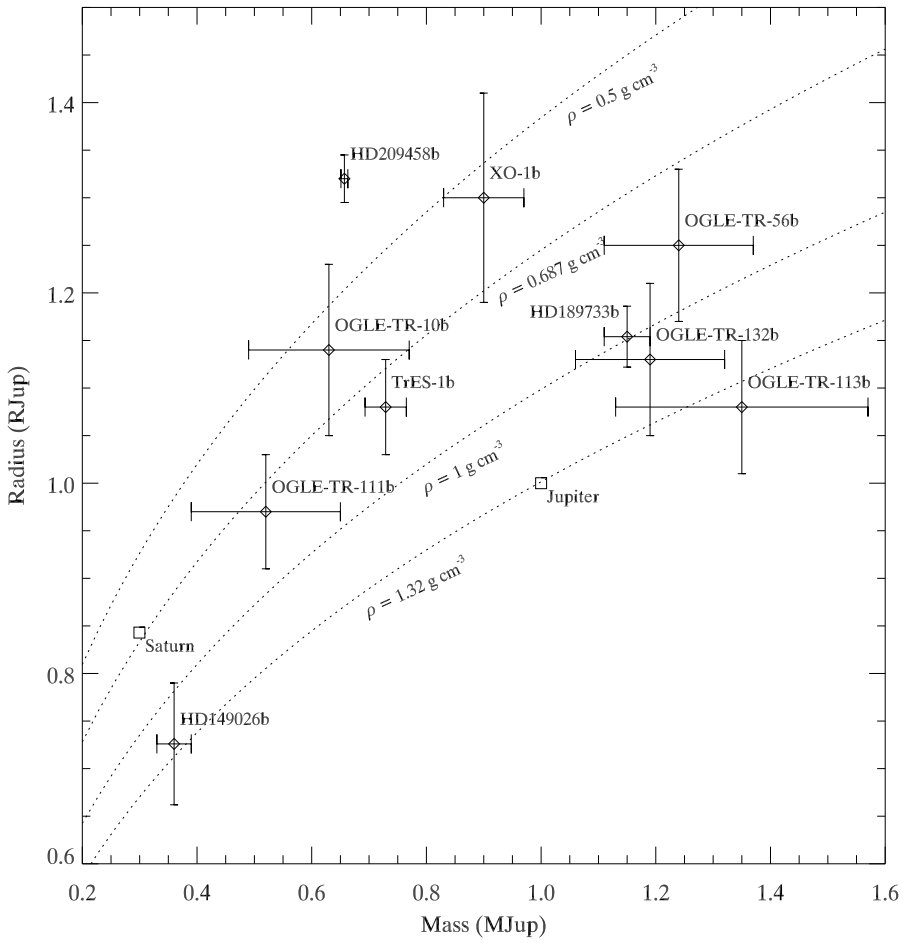

Figure 2.2: Mass-radius diagram for the known transiting extrasolar planets. Jupiter and Saturn are shown as open boxes displayed beside the dotted lines representing their densities. References: HD 209458: (Knutson et al., 2006, Santos et al., 2004), TrES-1: (Laughlin et al., 2005c), HD 149026: (Charbonneau et al., 2006c), HD 189733: (Bouchy et al., 2005, Bakos et al., 2006), XO-1: (McCullough et al., 2006), OGLE-TR-10: (Konacki et al., 2005, Santos et al., 2006), OGLE-TR-56b: (Santos et al., 2006, Holman et al., 2005), OGLE-TR-113: (Moutou et al., 2004), OGLE-TR-132: (Bouchy et al., 2004), OGLE-TR-111: (Santos et al., 2006)

tection of the Hα line of neutral hydrogen, which was 10 times stronger than expected (15% as opposed to an optical transit depth of 1.5%). In fact, the hydrogen signal implied an atmosphere that extended 4.3 planetary radii, which is beyond HD 209458b's Roche lobe of 2.7 planetary radii. The Hα measurement can thus only be explained in terms of escaping hydrogen atoms. Shkolnik et al. (2005), later confirmed that the neutral hydrogen loss rate is much greater than the loss rate of ionized hydrogen. A third atmospheric detection was made by Vidal-Madjar et al. (2004), again using the STIS spectrograph. They find O I and C II spectroscopic signatures, indicating that both atoms are also present in the extended atmosphere, the former atom even being present *up to* the level of the Roche lobe.

Parallel to all of these successful detections, there have been several significant non-detections reported. Deming et al. (2005a) report a non-detection of CO features during transit, even though a cloudless, radiative-equilibrium model would have been detected at the 3σ level. They propose a high, horizontal, optically-thick cloud deck to explain this level. Vidal-Madjar et al. (2004), together with their detection of O I and C II, report non-detection in transit of C I, C IV, N V, S I, Si II, Si III, and Si IV. Non-detections of the 3.6-μm methane signature using ISAAC at the Very Large Telescope (VLT) (Richardson et al., 2003b), nor water or CO using SpeX at the Infrared Telescope Facility (IRTF) in the range from 1.9 to 4.2 μm (Richardson et al., 2003a) were reported using occultation spectroscopy.

HD 209458b has also been the first planet (tying with TrES-1, see below) whose photons have been clearly distinguished from the stellar photons using occultation photometry. Deming et al. (2005b) reported detection of the sec-

ondary eclipse using the Multiband Imaging Photometer for the Spitzer Space Telescope (MIPS) using the 24-μm channel. From their timing and measurement of the secondary eclipse (depth of $0.260\% \pm 0.046\%$), they obtain a brightness temperature of 1130 ± 150 K and conclude that the data are consistent with zero orbital eccentricity, and thus is too low for any significant tidal heating. Fortney et al. (2005) present a model of the planet's atmosphere with standard solar abundances that fits the 24-μm observations.

2.3.2 TrES-1

TrES-1 was the second close-by transiting planet to be discovered (Alonso et al., 2004). It was discovered by the TrES* survey, which uses small-aperture, wide-field telescopes to search for transits among bright stars. It was confirmed by radial velocity measurements; in fact, it is the only confirmed discovery to this date by the TrES survey. The most recent measurements (Laughlin et al., 2005c) of the $\sim 2\%$ transit depth indicate a radius of 1.08 ± 0.05 R_J and a mass of 0.729 ± 0.036 M_J, values that are in agreement with their models of irradiated EGPs.

Charbonneau et al. (2005) report detection of thermal emission from TrES-1 using the 4.5- and 8-μm filters in the Infrared Array Camera (IRAC) on the Spitzer telescope. For each of the filters they find an eclipse depth of $0.066\% \pm 0.013\%$ and $0.225\% \pm 0.036\%$, respectively. They thus find a blackbody temperature of 1060 ± 50K. Just by coincidence, their paper was submitted on the same day as the paper by Deming et al. (2005b), with the equivalent result for HD 209458b. Fortney et al. (2005) find that a metallicity that is enhanced 3–5 times over the solar abundances is necessary to fit the observations of TrES-1.

*http://www.astro.caltech.edu/$\sim$ ftod/tres/tres.html

2.3.3 HD 149026b

Discovery of HD 149026b was reported by Sato et al. (2005). As is evident from Fig. 2.2, this planet is the least massive of all the transiting extrasolar planets. Furthermore, its transit depth of only $\sim 0.3\%$ is even smaller than what was expected for a planet of its mass orbiting a relatively large star ($\sim 1.45 R_{\odot}$). Sato et al. (2005) immediately recognized that its high density can only be explained by an enormous core of over 60 $M_{\oplus}$, composed of elements heavier than helium and hydrogen. This is more heavy elements than in all the planets of our solar system combined. Furthermore, the host star is richer in metals than our sun ([Fe/H] = 0.5). Hence, a high metallicity is expected in this planet.

Fortney et al. (2006) propose that if the planet has the metallicity of its host star (or several times as much as is the case for the giant planets in our solar system), it would imply an enhanced absorption of stellar flux by VO and TiO molecules, which could produce a hot stratosphere, and consequently limb brightening.

Harrington et al. (2006), using IRAC at Spitzer, measure an 8-μm secondary eclipse depth of $0.0844\%^{+0.0092}_{-0.0121}$. The corresponding brightness temperature of 2300 ± 200 K (7.9σ) is substantially hotter than measured for any other planet.

2.3.4 HD 189733b

Bouchy et al. (2005) detected a planet around the K star HD 189733. Since the star is of a late type and thus small, this system has the biggest transit depth ($\sim 3\%$) of all transiting planets discovered to this date. Therefore, it is expected to be under intense scrutiny in late 2006 when the observing conditions are the

most favorable (see Fig. 5.2).

Soon after its discovery, Hébrard and Lecavelier Des Etangs (2006) reported an a-posteriori detection in Hipparcos data, which improved the ephemeris considerably. Recently, multi-band photometric observations refined the values of radius, inclination, and mass (Bakos et al., 2006). The current best estimate of mean density is thus ~ 1 g cm^{-3}, which would place it between Jupiter's and Saturn's densities.

Deming et al. (2006) recently reported a detection of strong IR absorption from HD 189733b with an unprecedented 32σ confidence level using the peak-up imaging mode of the InfraRed Spectrograph (IRS) on the Spitzer telescope to observe the secondary eclipse (occultation photometry). The transit depth was $0.551 \pm 0.030\%$, which implies a 1117 ± 42 K brightness temperature at 16 μm. The high SNR they obtain allowed them to recognize the ingress/egress slope in the light-curve, but was not enough to distinguish between realistic models of the temperature distribution across the planet's disk. Charbonneau's group have already obtained Spitzer IRAC observations that will complement the result of Deming et al..

2.3.5 XO-1b

Very recently, the newest member of the transiting-planets family, XO-1b, was discovered (McCullough et al., 2006). For the first time, there are more transiting planets than the classical number of planets in our solar system. The host star of this system is the most similar to the Sun of all the host stars of transiting planets. The system is at a similar distance to that of TrES-1, an estimated 200 pc. The transit depth is ≈ 2 % and the orbital period is 3.941534 days, one of the

largest among the known transiting planets. The first estimate of the average density is ~ 0.52 g cm^{-3}, placing the planet within model expectations of a close-in EGP.

McCullough's group have already been granted follow-up occulatation photometry observations in Spitzer's cycle 3.

2.3.6 GJ 876?

Finally, it is worth mentioning the unusual case of the three planets orbiting the star GJ 876. Once the second planet ($M \sin i = 1.935$ M$_J$) was discovered, it was immediately identified as being in 2:1 orbital resonance with the first planet ($M \sin i = 0.56$ M$_J$, Marcy et al., 2001). A third planet was discovered later ($M \sin i = 0.023$ M$_J$, Rivera et al., 2005), but it is small and does not have any significant effect on the dynamics of the other planets. If the orbits of the two largest planets are not coplanar, then, on average for the possible orbital configurations, the resonance would cause a precession in the line of nodes of $-4\ ^\circ$ yr^{-1} (Laughlin et al., 2005a). This precession implies that the planets will become transiting planets as seen from the Earth at some point in the near future. If this happens, the transit depth of the biggest planet will be an unprecedented 10%, due to the small size of the host star. The transit will be observable for a period of about 2 yr.

Modeling the Transit | 3

The depth of a transit light curve is proportional to the ratio of the projected areas of the planet and the star. The key in current efforts to determine the composition of extrasolar planets has been that the projected planetary area depends on wavelength.

This chapter details our model of this phenomenon. The first section, §3.1, discusses the general properties of an appropriate model. The next section, §3.2, derives from general principles the main physics involved in the modeling. Finally, §3.3 discusses the programming of our code, `transit`.

3.1 The Model

A ray of light passing through the planet's atmosphere becomes dimmer at wavelengths located in the cores of atmospheric absorption features than at wavelengths where the atmospheric molecules do not absorb much (Fig. 3.1). The radius at which a ray of light is dimmed by a given amount (R_s) will thus vary over wavelength according to the spectral signature of the atmospheric molecules. Since the depth of the eclipse is proportional to the area blocked by the planet, a spectroscopic analysis of the out–of–transit *vs.* in–transit flux ratio (modulation) will permit identification of the molecules that are absorbing

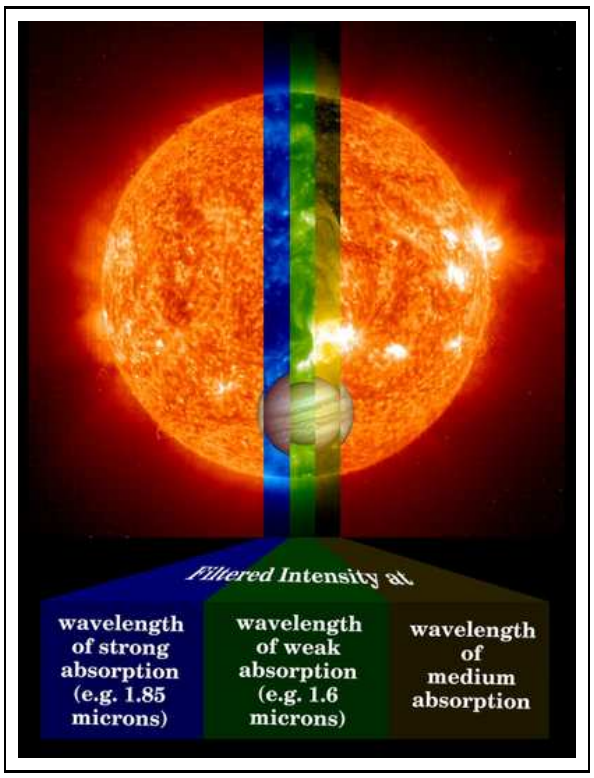

Figure 3.1: Representation of the modulation effect. This figure was made from edited pictures, which are courtesy of the SOHO/EIT consortium. SOHO is a project of international cooperation between ESA and NASA. Website: http://sohowww.nascom.nasa.gov/

the light in the exoplanetary atmosphere. The strength of the modulation also allows measurements of molecular abundances by comparison to models.

Based on the principles described in §3.2, a code was written in C in order to compute how much light the planet blocks at each wavelength. The code, called `transit`, returns the modulation spectrum, $\mathcal{R}_\lambda$, defined in Eq. (3.1). The result from the code was verified by matching the output of test cases to the result obtained by other groups like S. Seager's, J. Fortney's, and N. Iro's (private communication).

The code is described in more detail in §3.3. However, it is important to mention that the code has two required inputs: a database containing informa-

tion for all the molecular line transitions that are to be modeled, and an atmospheric profile for the planet. The latter consists of the temperature, pressure, radii, and composition tabulated for each level of the atmosphere. This work does not attempt to implement a second code to compute a synthetic planetary atmosphere. Instead, such profiles were obtained from collaborators who possess consistent codes which, at least, solve for the planetary emergent flux and temperature–pressure structure by simultaneously solving the hydrostatic, radiative, and chemical equilibrium equations in an atmosphere with the upper boundary condition that the bolometric emergent flux has to equal the incoming flux (e.g., Clayton, 1983).

Planetary profiles used in this work were obtained from Fortney et al. (2005) and Iro et al. (2005). These two teams model a plane–parallel atmosphere, which consists of a one–dimensional vertical simulation of the atmosphere that is justified by assuming that the curvature of the planet is negligible at the outer layers of a giant planet relative to the scale height. Furthermore, Fortney's code uses the prescription of Ackerman and Marley (2001) to find the cloud condensation parameters; and Iro's code accounts, in a first approximation, for atmospheric winds using a solid body rotation at each layer. Figure 3.2 compares the profiles from these groups. Even though the differences in the profiles on the region of relevance differ by up to 30% at some levels, they do not produce a significant effect on the computed modulation spectra.

3.2 The Physics

This section discusses the physics behind the modulation of stellar light by a transiting planet. Its contents are not specific to the case of HD 209458b, al-

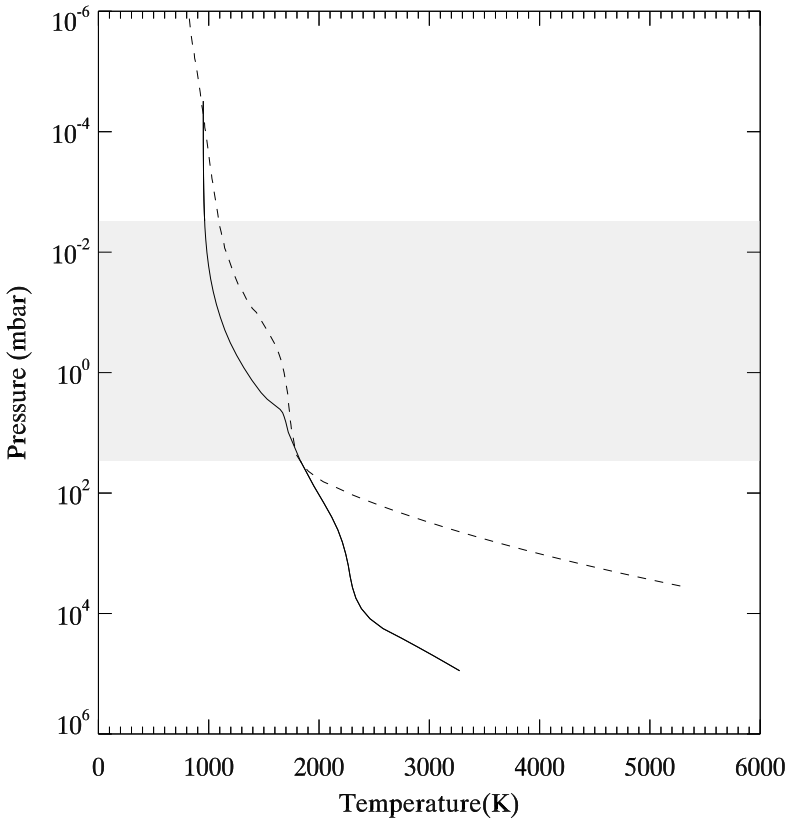

Figure 3.2: Comparison of the planetary profiles for HD 209458b obtained by Fortney et al. (2005, solid line) and Iro et al. (2005, dashed line). Gray area indicates the range of effective radius (Eq. 3.14) for the wavelength range used in our VLT observations (see Table 4.1).

though sometimes values from this planetary system have been used as examples.

The first section, §3.2.1, defines the conventions used in the modeling. After that, the sections are arranged such that the physics are discussed starting from a general perspective towards specific knowledge. Basic physics concepts and much of the mathematics behind the equations has been left to Appendix B and Appendix D, respectively.

3.2.1 Conventions

Only the most general conventions will be defined in this section; others will be defined when they are required. Most of the symbols used in this work are consistent within different sections. However, there are some instances where the same symbol had to be used to refer to different quantities; those cases are defined explicitly in the text.

Several definitions can be encountered in the literature regarding energy-related quantities; hence, Appendix B.1 derives from basic concepts a consistent notation and a set of definitions, which are used in this chapter.

Unless specified otherwise, *area* will refer to the projected area of the object in the sky plane. A star ($\star$) as a subscript indicates quantities related to the star, while the subscript 'p' indicates quantities related to the planet. Thus, R_p and $R_\star$ are the planetary and stellar radii, respectively. Also, from §3.1, R_s is defined as the projected radius at which the atmosphere becomes opaque by a given amount. The subscripts T and oT indicate in and out of transit, respectively. The letters b (for the radius) and ς (for the angle) are used for polar coordinates originating from the center of the planet's projected disc; R and ϕ are the equivalent stellar coordinates.

3.2.2 The Blockage

The observable (and distance-independent) quantity *modulation*, $\mathcal{R}_\lambda$, also known as spectrum ratio (Brown, 2001), is defined as

$$\mathcal{R}_\lambda = \frac{f_{\mathrm{T}}(\lambda)}{f_{\mathrm{oT}}(\lambda)}, \tag{3.1}$$

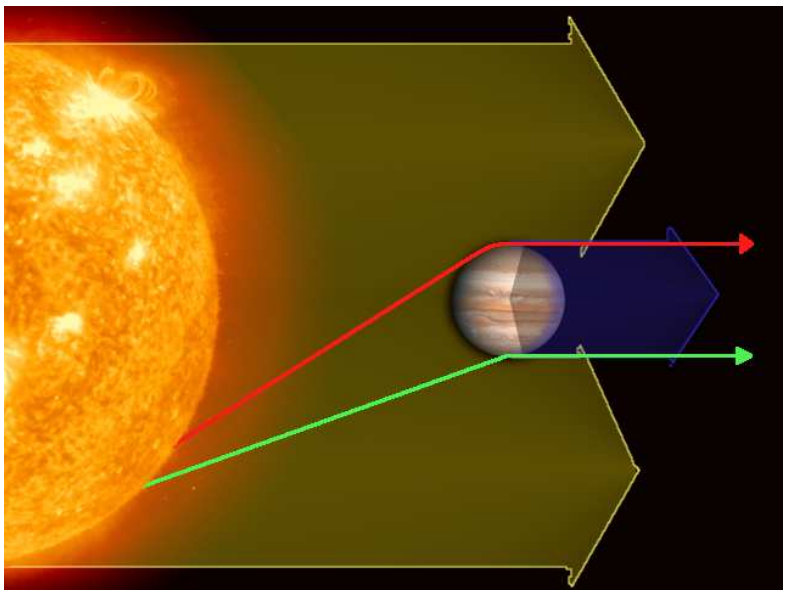

Figure 3.3: Diagram showing the possible sources of flux received from the planetary system while the planet is transiting. The picture of the sun is courtesy of SOHO/EIT consortium. SOHO is a project of international cooperation between ESA and NASA. Website: http://sohowww.nascom.nasa.gov/. Note that, because of the star's angular extent, less than a hemisphere is in shadow. The green arrow represents a particular reflected (f_{rl}) ray. The red arrow represents a particular ray that is either refracted (f_{rr}) or scattered (f_s). The yellow and blue arrows are the stellar ($f_\star$) and planetary (f_p) thermal emissions, respectively

where f denotes the flux from the system observed from Earth. Omitting the dependency of each term in λ for clarity, and including all the possible flux contributions that can be received from the system (Fig. 3.3), Eq. (3.1) becomes

$$\mathcal{R}_\lambda = \frac{f_{\star,\mathrm{T}} + f_\mathrm{p} + f_{rl} + f_{rr} + f_s}{f_{\star,\mathrm{oT}} + f_\mathrm{p} + f_{rl} + f_{rr} + f_s}. \tag{3.2}$$

Next, each of the terms in the equation above are described in detail.

Thermal emission (f_p)

The flux coming from the planet is defined as

$$f_\mathrm{p} = \frac{1}{d^2} \int_0^{2\pi} \int_0^{R_p} I_\mathrm{p}(b, \varsigma) b \, \mathrm{d}b \, \mathrm{d}\varsigma. \tag{3.3}$$

Sudarsky et al. (2003) find that thermal emission for a close-in EGP is of order 10^{-4} times the stellar flux for wavelengths greater than 2μm:

$$\frac{f_{\rm p}}{f_\star} \approx 10^{-4}. \tag{3.4}$$

This value is comparable with the value that will ultimately be obtained for $\mathcal{R}_\lambda$. However, the thermal emission remains essentially constant throughout the transit observations and hence its effect on the value of $\mathcal{R}_\lambda$ is to have a modified stellar flux, $\bar{f}_{\star,\rm oT}$, such that

$$\bar{f}_{\star,\rm oT} = f_\star + f_p \approx f_\star. \tag{3.5}$$

Reflected Emission (f_{rl})

The stellar flux reflected by the planet is given by (Eq. 2.4)

$$f_{rl} = f_\star \frac{A\ p(\alpha)}{4} \left(\frac{R_p}{a}\right)^2, \tag{3.6}$$

where a is the semi-major axis of the orbit, A is the albedo, and $p(\alpha)$ is the phase function, which depends on the planet-star-observer angle α.

For close-in EGPs like HD 209458b, the transit encompasses about $2\alpha \sim 15^\circ$ of the total orbit. If the observations span twice as much phase angle, then the maximum extension of the angle α during the observations is $\sim 15^\circ$. Even if the angular extent of the star (which leaves less than a hemisphere of the planet in shadow) is included, the geometry implies a small illuminated crescent on the planet, and consequently, a small phase function. For an order-of-magnitude estimate, the planet can be approximated as a Lambertian sphere and thus $p(\alpha) = 2[1 - \cos(\alpha)]$ for such a small value of α (Brown, 2001, and references therein). Consequently, even with $A = 1$, for a typical close-in EGP

the reflected light term is $< 10^{-7}$ times the flux from the star between the center of the transit and end of observations, respectively. Then,

$$\frac{f_{rl}}{f_\star} < 10^{-7}, \tag{3.7}$$

and thus, this term can safely be ignored, since, ultimately, $\mathcal{R} \approx 10^{-4}$.

Refracted flux (f_{rr})

Refracted or scattered flux have in common that both are produced by the redirection of rays that were not originally moving in our direction. Conversely, they can also deflect rays that were originally going in our direction. They differ in the physics that produce each effect.

Refraction is produced by a change of the index of refraction, n, in the atmosphere, which results from changes in the speed of light with index of refraction (see §3.4). The consequences of this change are derived in §3.2.3. For now, it is just important to note that it will produce a net bending of the ray given by (see Appendix D.1)

$$\Phi = -2\rho_0 \int_{r_c}^{\infty} \frac{\frac{\mathrm{d}n}{\mathrm{d}r}\,\mathrm{d}r}{n\sqrt{n^2r^2 - \rho_0^2}}, \tag{3.8}$$

which will cause the redirection of some rays towards the Earth (ρ_0 is the impact parameter defined as the closest approach of the ray to the planetary center if it were unbent, and r_c is the real closest approach). Hubbard et al. (2001) studied the magnitude of the refracted flux and concluded that it is negligible for close-in EGPs, as enough bending will only be attained by rays that pass deeply through the atmosphere, and thus they will be absorbed (mainly by molecular extinction, see §3.2.7) before they can get out.

For EGPs that are orders of magnitude farther from their host stars than a typical close-in EGP's distance of ~ 0.05 AU, the refraction could be important as the angle by which the rays need to be bent to reach Earth is smaller. Thus, the relevant rays will only go through the outermost layers, where they will not be absorbed. However, the chances of finding transiting planets that far from the host star are very low and their transits would be infrequent.

Scattered flux (f_s)

Scattering is produced by the interaction of a photon with a particle. It has different properties (and names) depending on the kind of particle. There are no free or relativistic electrons in the planetary atmosphere below the ionosphere (where the densities are too low to have any important effect); hence, there is no Thompson or Compton scattering. Mie scattering will only be relevant inside condensates (clouds). Raman scattering (which produces a change in the wavelength of the photon in addition to a change in direction) depends on many factors and has yet to be successfully modeled in the atmosphere of an extrasolar planet. However, extrapolating the work of Bétremieux and Yelle (1999) and Karkoschka (1994), Raman scattering is expected to be significantly less important than Rayleigh scattering in the IR.

Scattering due to molecules, Rayleigh scattering, is worth mentioning. Its effect on deflecting a ray that was originally directed towards Earth is accounted for by a scattering cross-section, which is discussed in §3.2.6. Hubbard et al. (2001) study the effect of Rayleigh scattering to deflect rays that were not originally directed toward us. They use Monte Carlo simulation to follow a photon as it travels through plane-parallel slabs. They find that even for optical wave-

lengths, the light scattered towards the Earth is negligible in comparison with the stellar flux. They do not support their result with numbers, but only with figures that needed to be enhanced by several orders of magnitude to visualize the flux due to scattering.

Stellar flux when out of transit ($f_{\star,\mathrm{oT}}$)

Considering a radial (only dependent on the distance to the center of the star) limb darkening function, B, the flux received from an unblocked star is (Eq. B.3)

$$f_{\star,\mathrm{oT}} = I_{0\star}\frac{2\pi}{d^2}\int_0^{R_\star} B(R)R\,\mathrm{d}R, \tag{3.9}$$

where d is the distance to the Earth, I_0 is the intensity at the center of the stellar disk, and $R_\star$ is the radius of the star.

Stellar Flux when in transit ($f_{\star,\mathrm{T}}$)

When the planet is transiting, we do not receive the full intensity from the star. Thus, the dimming of intensity due to blockage by the planet must be included. The intensity of a ray passing through a medium decays exponentially with the optical depth of the medium. Hence, the flux we receive from the star can be written as

$$\begin{aligned} f_{\star,\mathrm{T}} &= \frac{I_{0\star}}{d^2}\int_0^{2\pi}\int_0^{R_\star} B(R)\exp\left[-\tau_\lambda(b_{R,\phi})\right] R\,\mathrm{d}R\,\mathrm{d}\phi \\ &= f_{\star,\mathrm{oT}} - \frac{I_0}{d^2}\int_0^{2\pi}\int_0^{R_p} B(R_{b,\varsigma})\left\{1-\exp\left[-\tau_\lambda(b)\right]\right\} b\,\mathrm{d}b\,\mathrm{d}\varsigma, \end{aligned} \tag{3.10}$$

where τ_λ is the optical depth of the ray as it goes through the planet's atmosphere. It carries all the dependence of the above expression on wavelength.

Finally, consideration of all the above approximations (i.e., ignoring thermal,

scattered, and reflected emission) gives the following expression:

$$\mathcal{R}_\lambda = 1 - \frac{\int_0^{2\pi} \int_0^{R_p} B(R_{b,\varsigma}) \left(1 - e^{-\tau(b)}\right) b \, \mathrm{d}b \, \mathrm{d}\varsigma}{2\pi \int_0^{R_\star} B(R) R \, \mathrm{d}R}, \tag{3.11}$$

where the integration over ς is analytically impossible, due to the stellar-radius dependence of B. Notice that the limb darkening function varies the blocked flux for different positions of the planet on the star's projected disk. As we can only hope to acquire a significant signal by combining together all the observations obtained during transit, there is little point in trying to model a modulation spectrum using a limb darkening law. Thus, considering $B(R) \approx 1$, the expression for the modulation can be easily integrated to obtain

$$\mathcal{R}'_\lambda = 1 - \frac{1}{R_\star^2} \left(R_p^2 - 2 \int_{R_s}^{R_p} e^{-\tau_\lambda(b)} b \, \mathrm{d}b \right), \tag{3.12}$$

where R_s is the planetary *surface* radius, that is, the planetary radius at which the optical depth becomes so great as to be practically opaque to radiation at all wavelengths:

$$e^{-\tau_\lambda(R_s)} \longrightarrow 0. \tag{3.13}$$

We can thus define the *effective radius* ($R_{p,\mathsf{eff}}$) as

$$R_{p,\mathsf{eff}}(\lambda) = \left(R_p^2 - 2 \int_{R_s}^{R_p} e^{-\tau_\lambda(b)} b \, \mathrm{d}b \right)^{\frac{1}{2}}. \tag{3.14}$$

This is the equivalent wavelength-dependent radius at which an opaque disk with a hard edge produces the same modulation as the planet:

$$\mathcal{R}'_\lambda = 1 - \frac{R_{p,\mathsf{eff}}^2}{R_\star^2}. \tag{3.15}$$

Using the code `transit`, it is found that the effective radius is, at least in the case of HD 209458b, very close to the radius at which the tangential optical depth, τ_λ, equals 1.

The basic equations for the transit modulation have been expressed as a function of the optical depth τ_λ, which is the topic of the next section.

3.2.3 Occultation Theory

The path of a ray through the atmosphere of a planet is described by a well developed theory, the *Occulation Ray-Bending Theory*, a summary of which is presented here.

If the refractive index changes through the atmosphere, the ray will follow a curved path depending on the variation of the refractive index. Under the essential assumption of solely radial dependence of the refractivity index, one can solve analytically for the curved path.

Fermat's principle states that *the actual path between two points taken by a beam of light is the one that is traversed in the least time*. This principle implies that one needs to find the path, $\theta(r)$, that minimizes the total time, Δt, that the photon spends traveling through the atmosphere:

$$\Delta t = \int_{Atmosphere} \frac{n(s)}{c}\, \mathrm{d}s, \tag{3.16}$$

where c is the speed of light in vacuum, $n(s)$ is the refractive index ($n_{\text{vacuum}} = 1$) along the ray's path, and s is the the path traversed by the photon, which is defined as 0 at the point of closest approach.

Solving this equation analytically requires the use of a well known result from variational calculus (see Appendix D.2): If x_1 and x_2 are fixed points, then the path that minimizes the integral

$$T = K \int_{x_1}^{x_2} g\left(x, y(x), \frac{\mathrm{d}y(x)}{\mathrm{d}x}\right)\, \mathrm{d}x \tag{3.17}$$

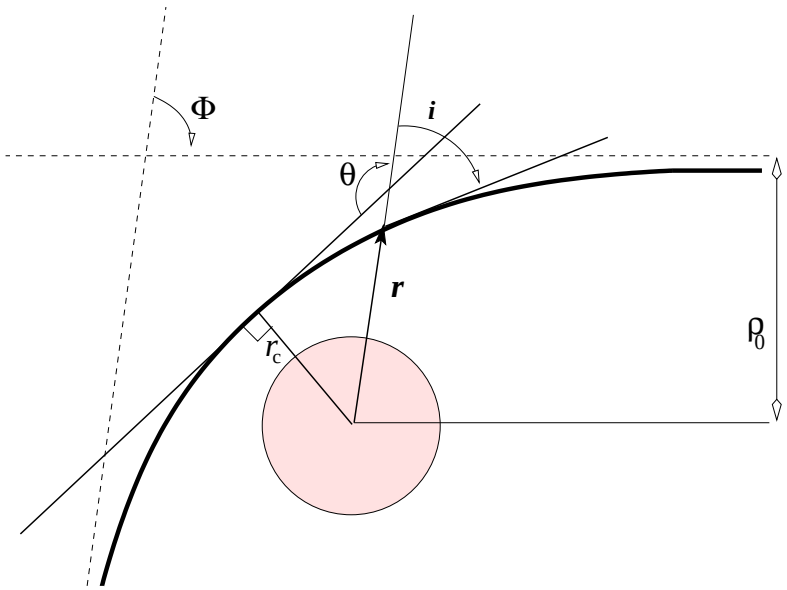

Figure 3.4: Geometry of a ray passing through a planetary atmosphere. Values refer to the position of a particular photon characterized by the vector **r**, or the angle between the direction of the photon at its closest approach and the projection of the position vector, **r**. The angle Φ is the total deflection of the ray, ρ_0 is the impact parameter, and i is the angle between the projection of the position vector and the instantaneous direction of motion.

follows

$$\frac{\mathrm{d}}{\mathrm{d}x}\left(\frac{\partial\, g}{\partial\left(\frac{\mathrm{d}y}{\mathrm{d}x}\right)}\right) = \frac{\partial g}{\partial y} \quad , \tag{3.18}$$

where K is a constant and g is any continuous function of x, y, and $\frac{dy}{dx}$.

Figure 3.4 shows the parameters for the path of a ray. A particular instant is characterized by the position vector **r**, which indicates the position of the photon, or by θ, which is the angle between the direction of the photon at its closest approach to the planet and the projection of the position vector. Other quantities are defined in the figure's caption.

Geometric considerations from Fig. 3.4 let us express a unit length of the

path as a function of either $\mathrm{d}r$ or $\mathrm{d}\theta$:

$$\mathrm{d}s = \sqrt{1 + r^2 \left(\frac{\mathrm{d}\theta}{\mathrm{d}r}\right)^2}\,\mathrm{d}r = \frac{r}{\sin i}\,\mathrm{d}\theta. \tag{3.19}$$

Then, making use of the bilateral symmetry about r_c, one can write Eq. (3.16) as

$$\Delta t = \frac{2}{c}\int_{r_c}^{\infty} n\sqrt{1 + r^2 \left(\frac{\mathrm{d}\theta}{\mathrm{d}r}\right)^2}\,\mathrm{d}r, \tag{3.20}$$

where r_c is position of the photon's closest approach to the center of the planet.

Identifying terms in Eqs. (3.17) and (3.18), one obtains

$$\frac{\mathrm{d}}{\mathrm{d}t}\left(\frac{nr^2\left(\frac{\mathrm{d}\theta}{\mathrm{d}r}\right)}{\sqrt{1 + r^2\left(\frac{\mathrm{d}\theta}{\mathrm{d}r}\right)^2}}\right) = 0, \tag{3.21}$$

which yields

$$\frac{\mathrm{d}\theta}{\mathrm{d}r} = \frac{\rho_0}{r\sqrt{n^2r^2 - \rho_0^2}}, \tag{3.22}$$

where ρ_0 is the integration constant independent of time, which turns out to be the impact parameter. An important relation for the latter is obtained by using the second equality of Eq. (3.19) in Eq. (3.22), thus obtaining

$$nr\sin i = \rho_0, \tag{3.23}$$

At the closest approach, $i = 90°$; thus

$$r_c = \frac{\rho_0}{n(r_c)}. \tag{3.24}$$

3.2.4 Optical Depth

The total optical depth is the sum of the local differential contributions along the path of the ray in consideration.

Using Eqs. (3.19) and (3.23), we obtain

$$\mathrm{d}s = \frac{n\, r^2}{\rho_0} \frac{\mathrm{d}\theta}{\mathrm{d}r}\, \mathrm{d}r. \tag{3.25}$$

Hence, using Eq. (3.22), the differential optical depth along the path is given simply by

$$\mathrm{d}\tau = \; e\, \mathrm{d}s = e \frac{n\, r}{\sqrt{n^2 r^2 - \rho_0^2}}\, \mathrm{d}r, \tag{3.26}$$

where the total volumetric absorption coefficient e, also known as the extinction coefficient, is used (see §3.2.6). Note that for the remainder of this chapter, e will not be used to denote the base of the natural logarithms.

Integrating Eq. (3.26), the optical depth for the ray's path through the atmosphere is given by

$$\tau_\lambda(\rho_0) = 2 \int_{r_c}^{\infty} \frac{e(r)\, n\, r}{\sqrt{n^2 r^2 - \rho_0^2}}\, \mathrm{d}r. \tag{3.27}$$

3.2.5 Index of Refraction

The refractivity $\nu = 1 - n$ (where n is the index of refraction) scales proportionally to the density of particles (Cox, 2000). Hence, only the contributions from hydrogen and helium are important ($f_H \approx 0.85$ and $f_{He} \approx 0.15$ are typical values for Jupiter or Saturn, where f refers to the number fraction of each constituent). Using the values from Cox (2000) for the refractivity at standard temperature and pressure (STP) conditions, we obtain

$$\nu_{\mathrm{STP}} = f_H \nu_{\mathrm{STP},H} + f_{He} \nu_{\mathrm{STP},He} \approx 6 \times 10^{-5}. \tag{3.28}$$

For a different density, ρ, the refractivity scales as

$$\nu = \frac{\rho\, \nu_{\mathrm{STP}}}{\bar{\mu}\, n_L}, \tag{3.29}$$

where n_L is Loschmidt's number and $\bar{\mu}$ is the mean molecular mass.

For the atmospheric conditions of relevance on HD 209458b, ν ranges from $\sim 10^{-4}$ to $\sim 10^{-11}$. Hence, a reasonable approximation is to assume that the index of refraction $n = 1 + \nu$ is equal to 1.

3.2.6 Extinction

In this and subsequent sections of this chapter, all quantities are expressed in terms of wavenumbers, $\bar{\nu}$, rather than wavelengths, as in

$$\bar{\nu} = \frac{1}{\lambda} \quad , \quad \bar{V} = \frac{1}{\Lambda}. \tag{3.30}$$

where Λ and $\bar{V}$ are respectively defined later as the center wavelength and wavenumber of a transition line. Wavenumbers are proportional to photon energy and give considerably simpler expressions than wavelengths.

The extinction coefficient, e (units of length^{-1}), is a measure of the fraction of light absorbed per unit distance traveled. The coefficient relates to the absorption cross section, σ (units of length^2), and opacity, κ (units of length$^2 \times$ mass^{-1}), through

$$e = \sigma \hat{n} = \kappa \rho, \tag{3.31}$$

where $\hat{n}$ is the number density and ρ is the mass density of the medium.

There are four main sources of extinction (or opacity, or absorption cross section): clouds, molecular scattering, collision induced absorption (CIA), and gaseous molecular transitions. Hence,

$$e = e_C + e_S + e_{CIA} + e_M. \tag{3.32}$$

Each of the terms is discussed below.

Clouds (e_C)

Strictly speaking, the opacity due to clouds is a type of scattering, but they will be considered separately due to their distinct effect.

Since we have a slant-path geometry, condensates can be modeled as a layer of infinite optical depth located at the level where the appropriate molecules are expected to condense. For close-in extrasolar planets, clouds made from iron and silicates (e.g., Mg_2SiO_4) are expected to form at pressures of a few tens of bars (Sudarsky et al., 2003, Fortney, 2005).

Scattering (e_S)

Scattered flux in §3.2.2 shows that Rayleigh scattering dominates over all other scattering sources. Cox (2000) gives an approximate expression for the Rayleigh scattering cross-section:

$$\sigma_R = 330\frac{\nu}{\lambda^4}\delta, \tag{3.33}$$

where $\delta < 1$ is the depolarization factor and λ is given in μm. Notice how the wavelength dependence implies that the cross section increases significantly as the wavelength decreases.

Hubbard et al. (2001) conclude that extinction due to scattering is insignificant compared with molecular extinction at radii larger than any practical R_s. Thus, scattering extinction was not implemented in the current version (3.3) of the model. However, the code was written so that the implementation could be done in the future without much inconvenience.

Collision-induced absorptions (e_{CIA})

Collision-induced absorption by H_2 pairs is significant in the IR. Borysow et al. (2001) compute CIA cross-sections from first principles. They provide a tabulated version* of their results, which `transit` interpolates to the required wavelength range and temperature. CIA from any other molecular pair (e.g., H_2-He) is several orders of magnitude smaller than between H_2 pairs, either because the cross-section is smaller or the numerical densities of the pairs are much lower.

Molecular absorptions (e_M)

After clouds, the most significant contributor to extinction in the atmospheres of close-in EGPs near $\tau_\lambda = 1$ (which defines the level at which the planet turns opaque) is molecular line absorption. This absorption is treated in detail in the next section.

3.2.7 Molecular Line Absorptions

Each bound-bound electronic transition appears as a spectral line with finite width. Each atom or molecule has a particular set of transitions, each with its particular strength and central wavenumber. It is thanks to that specific signature that it is possible to identify different components in an atmosphere just by analyzing the spectrum of light passing through the atmosphere.

At each wavenumber, `transit` sums the contributions from the line transitions of the relevant species. Leaving further details for Appendix C.2, the molecular extinction coefficient, e, as a function of wavenumber, $\bar{\nu}$, is given by

*http://www.astro.ku.dk/$\sim$ aborysow/programs/index.html

(Eq. C.15):

$$
\begin{aligned}
e_{M\bar{\nu}} &= \sum_{\{lu\}} e_{M\bar{\nu},lu} \\
&= \frac{\pi q_e^2}{m_e c^2} \sum_{\{lu\}} n_l \Psi(\bar{\nu}, \bar{V}_{lu}) f_{lu} \left[1 - \exp\left(-\frac{hc\bar{V}_{lu}}{k_B T}\right)\right],
\end{aligned}
\tag{3.34}
$$

where q_e and m_e are an electron's charge and mass, respectively; c, k_B, and h are the speed of light, Boltzmann, and Planck constants, respectively; and f_{lu} and T are the oscillator strength and temperature, respectively; and Ψ is the normalized profile shape described in detail below under *Line-broadening profile*. The sum is over all allowed combinations of upper and lower energy levels (u and l, respectively). Strictly speaking, one should sum over every single one of the transitions, but in practice their strength becomes insignificant some tens of Ψ-function full-widths-at-half-maximum (FWHM) from the center (i.e., 50 FWHMs from the line center, the profile is $\sim 4 \times 10^{-4}$ smaller than at the center). The sum can be restricted to those transitions at which the wavenumber center $\bar{V} = (E_u - E_l)/hc$ is close enough to the wavenumber, $\bar{\nu}$, under consideration.

The number density of atoms with available electrons in the energy level l is given by n_l. Assuming local thermodynamic equilibrium, Eq. (B.6) yields

$$
n_l = \frac{g_l \rho_{lu}}{m_{lu} Z_{lu}} e^{-\frac{\Delta E_l}{k_B T}},
\tag{3.35}
$$

where E_l is the energy at level l, ρ_{lu} is the mass density, Z_{lu} is the partition function, and m_{lu} is the molecular mass of the species responsible for that particular lu transition.

Using both Eqs. (3.35) and (3.34) we obtain a expression for the extinction coefficient, given by:

$$
e_{M\bar{\nu}} = \sum_{\{lu\}} \rho_{lu} \Psi(\bar{\nu}, \bar{V}_{lu}) \left(1 - e^{-\frac{hc\bar{V}_{lu}}{k_B T}}\right) \frac{\sigma'_{lu}}{m_{lu}},
\tag{3.36}
$$

where

$$\sigma'_{lu} = \frac{\pi e^2 g_l f_{lu}}{c^2 m_e} \left(\frac{1}{Z_{lu}} e^{-\frac{E_l}{k_B T}} \right). \tag{3.37}$$

Note that this latter quantity is not completely independent of atmospheric properties. The factor in parentheses depends on temperature and has been dealt with carefully in the model design. The oscillator strength and degeneracy ($g_l f_{lu}$ factor) can usually be obtained from tabulated empirical or theoretical data for the species, as discussed below under *About Water*.

Line-Broadening Profile

The line profile, Ψ, depends only on the distance to the central wavenumber. An accurate representation of the broadening of a single spectral line is given by the Voigt profile:

$$\Psi\left(\bar{\nu}, \bar{V}_t\right) = \int_{-\infty}^{\infty} D(\bar{\nu}', \bar{V}) L(\bar{\nu} - \bar{\nu}', \bar{V}) \, \mathrm{d}\bar{\nu}', \tag{3.38}$$

where D and L are the Doppler and Lorentz profiles, respectively. The former is the well known spectral broadening due to the motion of molecules. The latter is due to uncertainties in time that, according to the Heisenberg uncertainty principle, produce indeterminacy in the energy levels, which broadens the line shape. In contrast to the exact theory behind the Doppler profile, the Lorentz profile is just an approximation to significantly more complicated physics (e.g., Burrows and Volobuyev, 2003).

The Doppler and Lorentzian profiles are given by

$$D(\bar{\nu}, \bar{V}) = \frac{1}{\alpha_D} \sqrt{\frac{\ln 2}{\pi}} \, e^{-\ln 2 \left(\frac{\bar{\nu} - \bar{V}}{\alpha_D} \right)^2} \tag{3.39}$$

$$L(\bar{\nu}, \bar{V}) = \frac{\alpha_L}{\pi} \frac{1}{\left(\bar{\nu} - \bar{V}\right)^2 + \alpha_L^2}, \tag{3.40}$$

where α_L and α_D are the Lorentzian and Doppler FWHM, respectively. They are defined as (see Appendix C):

$$\alpha_D = \frac{\bar{V}}{c}\sqrt{\frac{2k_B T \ln 2}{m}} \tag{3.41}$$

$$\alpha_L = \Gamma_{nat} + \frac{\sigma_c}{\pi c}\sqrt{\frac{2k_B T}{\pi}}\sum_i n_i \sqrt{\left(\frac{1}{m_r} + \frac{1}{m_i}\right)}, \tag{3.42}$$

where m is the molecular (or atomic) mass of the species, and T and P are the ambient temperature and pressure, respectively. Appendix C.3.3 details the numerical approximation utilized to obtain the Voigt profile.

About Water

As detailed in §1.1, the target of this work is the detection of water molecules. A procedure typically employed in the modeling of atmospheric spectra for arbitrary molecules is to use widely available semi-empirical line databases like HITRAN*. Their tabulated values are then scaled to the desired atmospheric conditions.

However, a more specialized line database prepared by Kurucz (1999) was used, given the high temperatures expected for this planet. That database is an edited version from the theoretical water-line strengths obtained by Partridge and Schwenke (1997, P&S hereafter).

The database contains several files of sample FORTRAN programs, text data, and binary packed data. Only two files were used. Values of the partition function (Z_{lu}) for temperatures ranging from 10 to 6000 K are contained in the file `h2opartfn.dat`. The binary file `h2ofast.bin` contains 65,912,356 coded records of line information, each 8 bytes long. Each record contains 4 bytes of wave-

*HITRAN database. http://cfa-www.harvard.edu/HITRAN/

length information, 2 bytes of lower energy information, E_l, and 2 bytes of degeneracy times oscillator strength information, $g_l f_{lu}$.

3.3 The Code

The code, written in C, produces a planetary modulation spectrum using the radiative transfer physics described in the previous section. The code is called `transit` and it is available under the GNU General Public License from the DSpace* Internet archive or upon request from the author**.

In what follows, a `monospaced` font is used when referring to a specific option of the program. Version 3.3 of `transit` was used for the the analysis of this project, and that is the version described below.

`transit` has an extensive built-in help documentation (accessible using the option `-h` and shown in Appendix E.2) that describes all the possible options and switches. These can also be given in a configuration file (using the option `-p`); in this way it is possible to prepare several different parameter files that will permanently store the parameters of a given model spectrum.

This code was designed with the idea of modularity in mind: modifications or additions (e.g., adding flux contributions from other sources to Eq. (3.12), or adding another line database source for different species) could be done easily in the future with little code rewriting and, in most cases, none at all.

Figure 3.5 shows the structure of the main program. The following sections describe briefly its inputs, procedures, and outputs.

*http://dspace.library.cornell.edu/handle/1813/3209

**My permanent website: http://www.das.uchile.cl/∼ pato/sw/

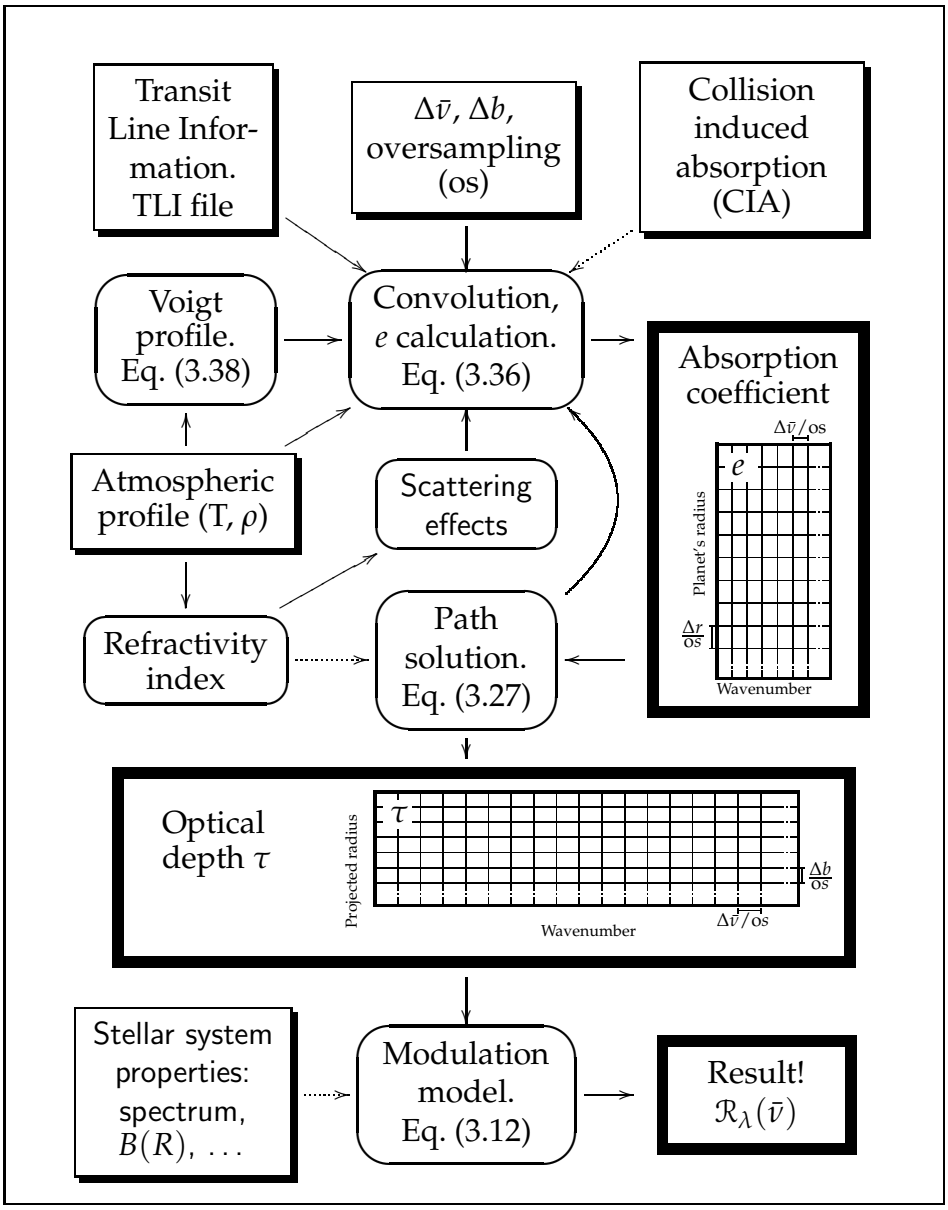

Figure 3.5: Modulation model diagram. Boxes with thick borders represent final or partial results, oval boxes represent procedures, and shadowed boxes represent input data. Dotted arrows represent connections that may or may not exist depending on user parameters. Sans serif font face represents stages that have not yet been implemented, but their eventual inclusion in the code should be straightforward. Omitted from this figure are several optional user inputs that control the code at different stages (e.g., output file name, how often the Voigt profile is recalculated, etc).

3.3.1 Inputs

There are only two required options that do not have meaningful default values: `--linedb`, which indicates the name of the data file containing the molecular information for each line transition in the `transit` line information (TLI) format, and `--atmfile`, which indicates the name of the data file containing the atmospheric planetary profile. Any other option (more than 60 so far) either has a default value or is not required. The built-in help (also Appendix E.2) gives details.

Below, each of the five inputs to `transit` (shadowed boxes in Fig. 3.5) is detailed.

TLI file

Relevant transit option: `--linedb`.

The TLI file is prepared by an auxiliary program in the `transit` package called `lineread`. Its structure appears in Figure 3.6. Because the formats of different databases (like HITRAN or P&S) vary widely, this auxiliary program was created to handle the task of mixing and sorting the line information from any number of different species in different databases by wavelength. Then, it outputs a data file in TLI format for `transit` to read. Currently, `lineread` is only able to read the water database of Partridge and Schwenke (1997) as distributed by Kurucz (1999).

Alternatively, `transit` can read an ASCII-TLI formatted file. This format was created to allow for quick editing by a user who wishes to test some cases with only a few spectral transition lines. A template of this format is available

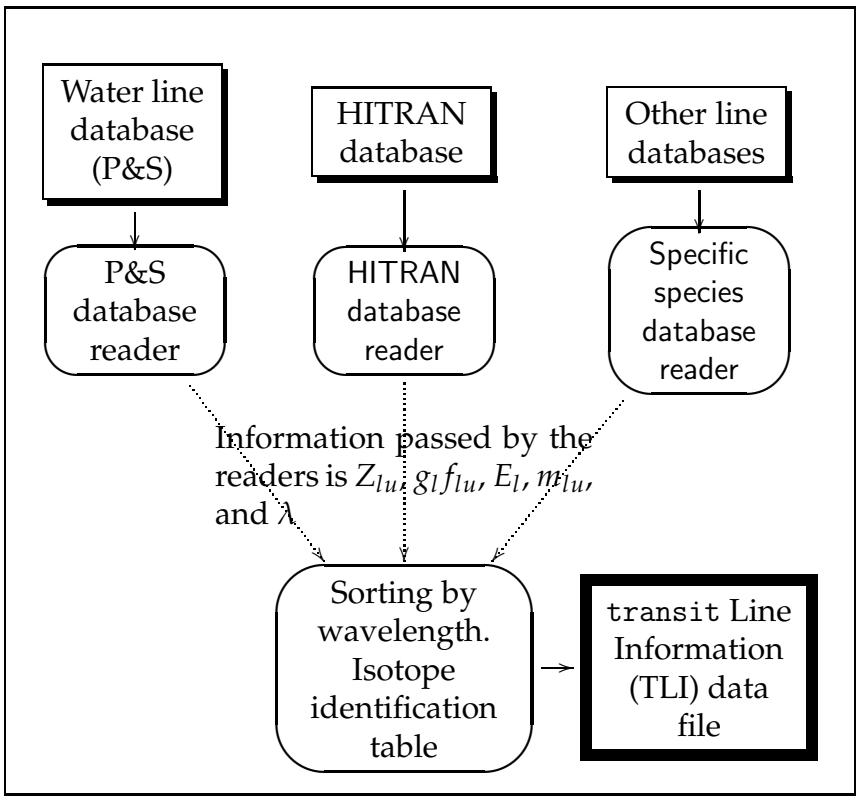

Figure 3.6: Structure of auxiliary program `lineread`, which produces a line information data file in the `transit` line information (TLI) format. Shape of boxes, arrows, and font type are as in Fig. 3.5. The final result is stored in a file that is input to `transit`. Note that none of the species is particularly required, but information from at least one of them has to be available

in the `transit` package.

Sampling parameters

Relevant `transit` options: `--wn-*`, `--wl-*`, `--rad-*`, `--ip-*`.

The user can specify the parameters regarding the wavenumber and planetary radius sampling. Because their values will greatly affect the running time of the code and the precision of the result, the appropriateness of the default values should be checked carefully.

Collision Induced Absorption (CIA)

Relevant `transit` option: `--cia`.

The program `transit` is able to read a list of tabulated cross-sections for a range of temperatures and wavenumbers, which is the file format in which Borysow et al. (2001) distribute their files.

Atmospheric profile

Relevant `transit` option: `--atmfile`.

The vertical temperature, pressure, and composition profiles for the atmosphere of the transiting planet need to be given to `transit` on each run. For this work, such information was procured from collaborators as described in §3.1. A plain-text file format template for the atmospheric data is available with the `transit` distribution (also shown in Fig. 3.7). The atmospheric profile file containing the model from Iro et al. (2005) is shown in Appendix E.1.

The first part of the atmospheric file consists of several configuration lines, each with its own identification, so that relative order does not matter. The second part contains tabulated temperature, pressure, radius, and composition for the different levels of the atmosphere.

Among the configuration options of this file are the choice of mass or number abundances for the tabulated composition; the use of multiplicative factors for the pressure, temperature and radius, so that any unit can be used; the use of a radius offset; and an easy way to change specific molecular abundances at each layer without changing the total density.

```
#Comments are ignored
#indication whether abundances below are by mass or number.
#Only one such line should exist, indicating abundances by
#mass or by number.
q mass
#or
q number

#Unit conversion.
z  <radius offset in same units as tabulated data>
ur <factor to convert radius to cm>
up <factor to convert pressure to dynes/cm2>

#i lines contain isotope information. Masses in AMU
i <mass1-name1>           <mass2-name2>
i <mass3name3>   <mass4-name4> <mass5-name5>

#an isotope starting with '!' is ignored but has to have
#a column below (used for reference to 'f' isotopes below)
i !<massi6-namei6>

#Lines starting with f contain isotopes to be obtained
#from other isotopes abundances.
#In the following example, the 7th isotope will have <fct>
#times the abundance of the 3rd isotope.
f <massi7-namei7> = <fct> <namei3>

#The special keyword 'other' as the reference isotope
#indicates that the reference abundance will be whatever
#is needed so that the abundances sum to 1.
#The line below sets the abundance of the 8th isotope to
#<fct> of the unaccounted atmosphere.
f <massi8-namei8> <fct> other

#From the first non-keyworded line everything is
#atmosphere info
<radius1> <press1> <temp1> <abund1,iso1> ... <abund1,iso6>
<radius2> <press2> <temp2> <abund2,iso1> ... <abund2,iso6>
.....
```

Figure 3.7: Sample portion of the atmosphere template file as found in the `transit` package

Stellar system properties

Using custom stellar system properties like a stellar spectrum, planetary thermal emission, or limb darkening for different transit geometries has not been enabled yet. Finding usable physical expressions under those conditions is beyond the scope of this work. However, routines able to handle these could be added to `transit` without much difficulty.

3.3.2 Procedures

For each wavenumber of the selected scale, the optical depth along a tangential path with a given impact parameter is computed using Eq. (3.27). The computation starts with an impact parameter, ρ_0, equal to the radius of the uppermost layer and descends into the atmosphere until the tangential optical depth rises above a certain user-defined limit (`--toomuch`). We find that that value should be at least 5 for convergent results. Each time this procedure reaches a radius whose extinction has not been computed, it calls the extinction-computing routine, which uses Eq. (3.32) to compute the extinction spectrum over the whole wavenumber range at the specified radius. This extinction spectrum is stored to avoid calculating it again when computing the optical depth at another wavenumber with an extinction at least as transparent. By using this on-demand approach, extinction for radii that are too deep in the atmosphere to be relevant for the modulation do not need to be computed.

Calculating the extinction from Eq. (3.32) for all contributions takes most of the runtime, as Eq. (3.36) needs to be computed for each of the line transitions. Furthermore, the Doppler FWHM (Eq. 3.41), and hence the Voigt pro-

file (Eq. 3.38), do not remain constant at each wavelength. Computing a new Voigt profile for each of the transitions is computationally too demanding (Appendix C.3.3). Therefore, a Voigt profile is computed once for the starting wavenumber and then is only recomputed when the width of the profile at the particular wavenumber has an error greater than a given fraction (`--maxratio`) of the computed profile width. The profile is computed in a wavenumber range that is a given number of times (`--nwidth`) the maximum of the Doppler and Lorentz widths.

Once the optical depth has been computed up to its maximum value at all wavelengths, the modulation, $\mathcal{R}_\lambda$, is computed using Eq. (3.12). With a modern desktop computer (e.g., 64-bit, 2 GHz CPU), a modulation spectrum with more than half a million wavenumber points in a range that includes over 20 million water lines takes a few hours to compute using the code `transit`.

3.3.3 Outputs

Relevant `transit` options: `--output`, `--outtoomuch`, `--outsample`, `--detailtau`, `--detailext`, `--detailcia`, `--outtau`.

The main output of `transit` is $1 - \mathcal{R}_\lambda$. However, the user can request several optional outputs: a file containing the lowest radius per wavenumber (beyond which extinction was not computed); a file summarizing all the sampling scales used for the different parameters; and detailed, per-radius values of extinction, optical depth, and CIA at specified wavenumbers. As an alternative to the transit modulation, the user can request the optical depth per wavenumber at a specified radius.

Figure 3.8 shows example modulation output at different wavelength reso-

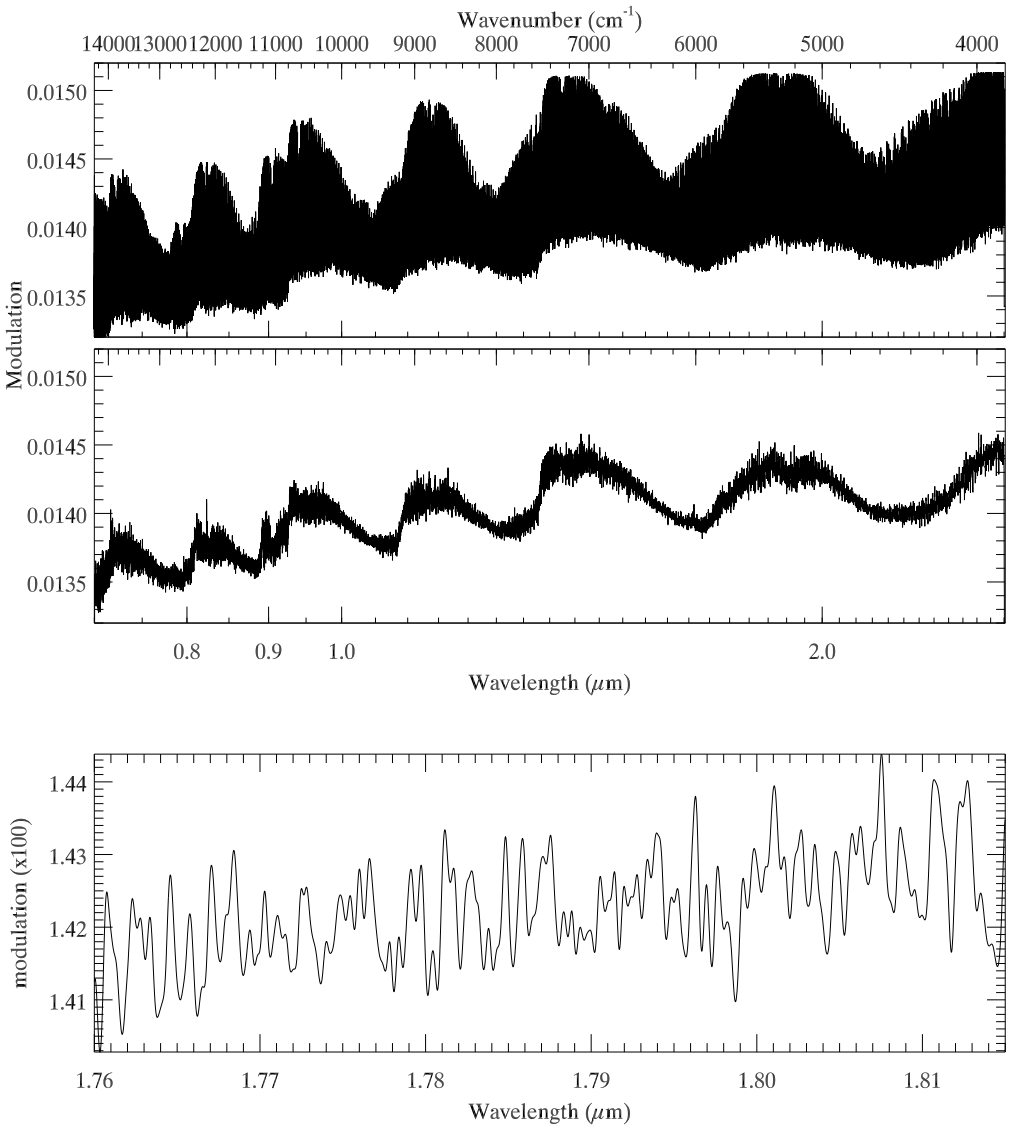

Figure 3.8: Example modulation models from `transit`. Top: Modulation with infinite (or natural) resolution for a large wavelength range. Middle: Same wavelength range but spectral resolution equivalent to the VLT observation. Bottom: Wavelength resolution and range equivalent to VLT observations, which is the signature this project is looking for in the data introduced in Chapter 4.

lutions and ranges.

The Data | 4

This chapter describes the telescope, instrument, and strategy chosen for the observations, the data reduction pipeline, and the algorithms employed to clean telluric features. It finishes with the analysis by comparison to the theoretical modulation.

4.1 Instrument and Setup

The data for this work were obtained with the Very Large Telescope (VLT) nicknamed "Antu" (or VLT-1) at the Paranal Observatory, which was built and is operated by the European Southern Observatory (ESO). The instrument used is ISAAC (Moorwood et al., 1998), a near-IR (1–5 μm) spectrograph. See Table 4.1 for a summary of the telescope properties and the relevant setup parameters of the instrument.

Observations of the planetary system were carried out on 4 non-consecutive nights. The first night was the only one without a transit event. That night serves as a control night against which to check our results.

The center of transit events for HD 209458b was found by propagating the period from an ephemeris time (Table 2.3, values from Knutson et al., 2006). The ephemerides must be corrected from heliocentric to geocentric transit times

Table 4.1: Telescope and instrument information

Telescope		Instrument Setup	
latitude	24°40′ S	wavelength range	1.75–1.82
longitude	70°25′ W	resolution	~ 3000
altitude	2 635 m	array size	1024×1024 pixels
aperture	8 m	nod strategy	ABBA
timezone	UT -4	integration time[a]	30 sec
		slit width	0.6″
		resolution element	1.6×10^{-4} μm

[a]per frame

to account for the time the light from the star takes to travel the projected Earth-Sun distance. The transit phase ranges from -0.5 to 0.5, with 0 being the center of the transit.

Two constraints on the selection of our observing nights were considered. First and foremost is the timing of the transit, and second is the airmass. In order to avoid strong telluric absorption and variability, the observations were limited observations to ~ 2 airmasses or less. Ideally, the center of the transit should occur at the lowest possible airmass; however, there are only about two transits per week, given the planetary period of ~ 3.5 days (thus at most 1 night per week). The degree of success in achieving these constraints for the four selected nights is shown in Fig. 4.1.

A nearby non-variable star (HD 210483, magnitude $V = 7.59$) was chosen as the calibrator. This star is only slightly brighter than the target star HD 209458 ($V = 7.65$), and has a similar spectral type. The idea was to use the calibra-

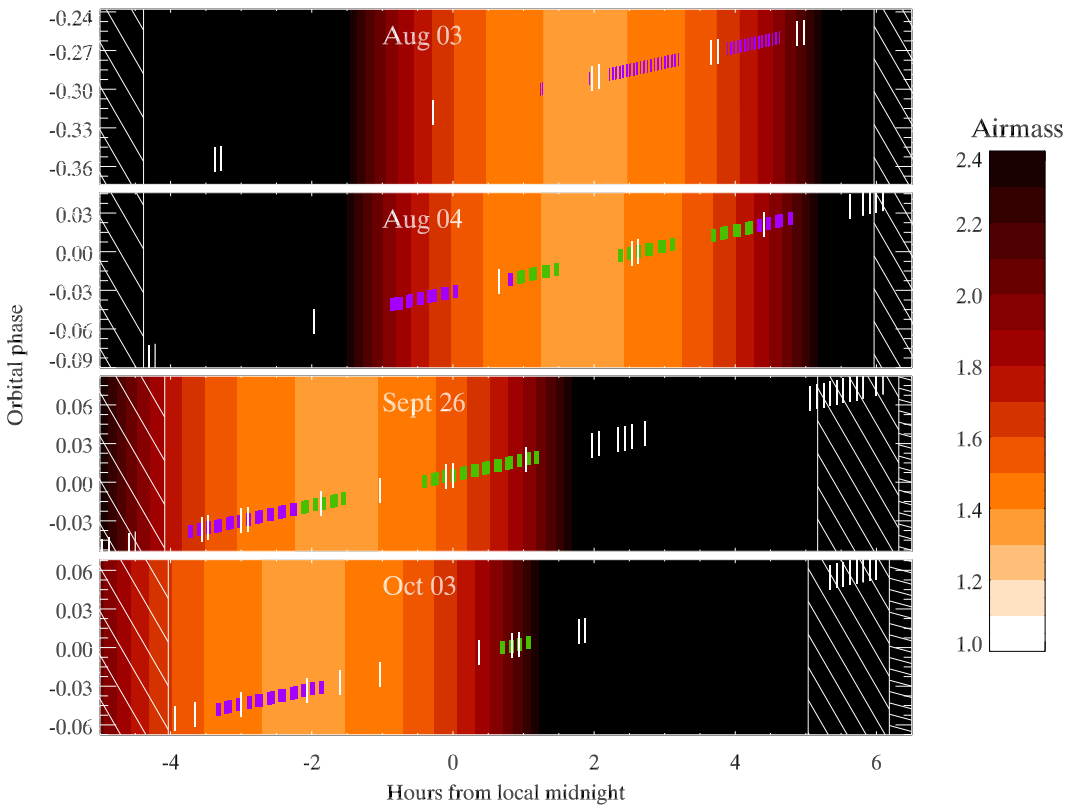

Figure 4.1: Distribution of observing time during the allocated nights. Each spectrum is indicated by a green bar or purple bar depending on whether the system was in transit or not, respectively. The boundaries of the line-filled areas indicate the evening and morning twilight. Background color is the airmass. White bars indicate the time at which flat fields were taken.

tor star to derive and correct for atmospheric effects such as the variable water column. However, early in the data processing stage it became clear that the wavelength scale shifted in the object data after each visit to the calibrator. They were probably due to small displacements of movable instrument parts. Furthermore, after considering the time spent acquiring and observing the calibrator star, the total time spent on HD 209458b was only about 15% of the total available time (see Table 4.2). Given the stability of modern telescopes and availability of new processing techniques, it is not recommended to use a calibrator star in future observations of this kind using large (slow) telescopes, unless the

calibrator can be observed simultaneously (see §5.3). Instead, it is better to avoid any movement of the telescope other than the minimum required to follow the star across the sky and to nod if necessary (see below). This approach has been demonstrated to freeze systematic errors and give a consistent dataset for an analysis such as this, where only the variation of the signal is of interest. (e.g., Deming et al., 2005a, who did not even nod).

Since the temperature in HD 209458b's atmosphere is significantly higher than that in the Earth's atmosphere, the spectral signature is different due to excited lines that appear only in the spectra of the close-in extrasolar planet's atmosphere. The wavelength range from ~ 1.75 to ~ 1.82 μm was chosen because it lies in the wings of a strong water vapor absorption band. Lacking a better algorithm to select the wavelength range (like the one proposed in §5.3), our team thought that the excited water lines in the extrasolar planet would be strongest near the band, while at the same time that range avoided the worst part of the highly variable telluric water absorption. However, as becomes clear in §5.3, the observing wavelength range was unnecessarily close to the absorption band. This unfortunate choice of wavelength, it is argued in §5.1, is what ultimately led to an unsuccessful detection of water in the atmosphere of HD 209458b.

At IR wavelengths, emission from the sky is very bright. At wavelengths longer than 3 μm it can even be several times the signal from most astronomical sources. A standard method to deal with this in IR spectroscopy is to nod the telescope along the slit length. The spectrum is received in two distinct regions of the array, identified as beams A and B. The nodding is repeated throughout the observations in the sequence ABBA. As explained in the next section, the AB image pairs can then be subtracted to remove, among other things, sky

Table 4.2: Summary of observations

Date in 2002	Minutes available[a]	Minutes observed[b]	Phase 0 airmass	Total frames	Average seeing
Aug 03	390	73.5	—	148	0.85
Aug 04	390	63.25	1.416	80	1.60
Sept 26	330	41.5	1.472	40	0.89
Oct 03	300	19.5	1.995	84	0.85

[a]number of minutes the planet was observable

[b]minutes available less the time spent on the calibrator or as telescope overhead

emission. The sky will only be successfully removed if the time between the frames obtained at the different positions is short enough that the sky remains relatively constant.

In the chosen wavelength range, the sky brightness is less than the object brightness, but the telescope was nodded anyway to be certain and to remove several other sources of systematic error, as detailed in §4.2.1. Furthermore, in order to prevent the sky from varying too much between beam positions, the integration time of each spectral frame was limited to 60 seconds. Flat fields were taken approximately every hour (see Fig. 4.1).

The observations are summarized in Table 4.2.

4.2 Data Reduction

The data were reduced in three main steps: frame correction and spectrum extraction, wavelength and flux calibration, and telluric correction. Shadowed frames in Fig. 1.6 indicate these stages. After going through this pipeline, the

data are ready to be compared with the output of the previous chapter's model, as described in §4.3.

All of the processes described in this section and the next were implemented in the Interactive Data Language (IDL, a product of Research Systems, Inc., Boulder, Colorado). The code is available under the GNU General Public License from DSpace* Internet archive or upon request from the author.

4.2.1 Frame Correction and Spectrum Extraction

Basic steps in any array data reduction pipeline are removal of the per-pixel baseline level and flat-fielding the image. Since the ABBA nodding strategy was employed, the spectral trace was located in different areas of the detector array for consecutive frames. In the position where the spectral trace A is, the frame B has sky, which is assumed to have the same level as it had when frame A was taken. Furthermore, both frames will have the same baseline levels (bias, dark current, telescope mirror's thermal emission) at the same pixel positions. Therefore, subtracting frame B from frame A yields the signal from the spectral trace A less the contribution from the sky and baseline levels. Likewise, a clean spectral trace B is obtained by subtracting frame A from frame B.

The expected spectrum modulation is of order $\sim 10^{-4}$ times the incoming stellar intensity (see §5.3). Hence, it is necessary to eliminate any systematic effect that could contribute noise even if its contribution is only a few percent of the stellar intensity. One such effect was a clearly visible fringe pattern present in the flat fields with an amplitude of a few percent (see Fig. 5.8). This pattern is due to reflections of light in the interior of the instrument. A new method to

*http://dspace.library.cornell.edu/handle/1813/3209

eliminate such a pattern from the array using the wavelet transform was developed during the course of this work (see §5.4 or Rojo and Harrington, 2006).

Several flat fields bracketed all our observations during each night (Fig. 4.1). Hence, there are three different ways of applying them: (1) the construction of one average flat field frame common for every object frame, (2) linearly interpolating the bracketing flat fields to the corresponding timing of the object frame, and (3) the use of the flat-field frame obtained closest in time to each object frame. In all cases, the flat-field frame is normalized before dividing it from the object frame. The last two methods gave consistently similar results and better results than the first method. Therefore, in what follows only the results obtained through the third method are shown.

Bad pixels in the data frame were identified by comparing median averages between neighboring pixels and between frames. These pixels were masked and not considered in any later analysis. Each clean, flat-fielded, sky-subtracted, two-dimensional (2D) frame was then processed through an optimal spectrum extraction algorithm developed by Dermody and Harrington (2006, in preparation)*, which is based on the algorithm of Horne (1986). This optimal extraction algorithm weights the spectral pattern in the 2D frame by an empirically fitted spatial profile. It also considers curvature of the spectral trace and returns the variance of the spectrum.

At this stage, the dataset contains 148, 80, 84, and 40 one-dimensional spectra for each night, respectively. Each spectrum has its accompanying variance, which is dominated by Poisson noise from the stellar signal. Each night is divided by beam position (A or B) for a total of 8 datasets. Throughout the calibra-

*http://oobleck.astro.cornell.edu/jh/ast/software.html

tion and analysis, each of them is treated independently. Only when obtaining an average correlation are the signals from different beams mixed (see §4.3.2).

4.2.2 Spectrum Calibration

An absolute flux calibration is not necessary because the aim is to find the modulation of the signal by comparing the in-transit with the out-of-transit spectra. It is thus safe to normalize each spectrum by dividing it by a constant, which was chosen as the average value of a third order polynomial fit to selected continuum windows. About 10 continuum windows were identified. This eliminates differences in flux due to changes in seeing that cause different amounts of star light to be blocked by the spectrograph's slit.

Wavelength was calibrated by comparing telluric lines that are common to the spectra in our dataset and a solar spectrum convolved to the correct spectral resolution. Hence, before obtaining a wavelength calibration it is necessary to find two quantities: the relative wavelength shift between spectra from the same night and beam, and the spectral resolution.

The relative shift was found by minimizing the root-mean-square (RMS) of the correlation (see §4.3.2 for details of this technique) between a reference spectrum and each of the other spectra shifted in intervals of 0.01 pixels for a range of two pixels in each direction. The resulting shift was never larger than half a pixel.

The spectral resolution of each spectrum was obtained by linearly fitting the spectrum with a convolved version of a telluric spectrum (T. Hewagama, private communication, see §4.2.3 under TCM-2). Using a Gaussian function as the convolution kernel and repeating the fit using different Gaussian widths al-

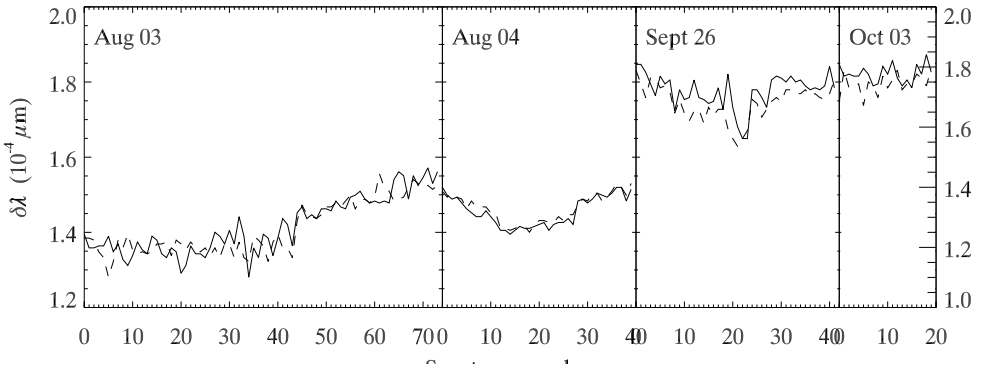

Figure 4.2: Empirically fitted values of spectral resolution for each spectrum through the night. Solid and dashed lines indicate spectrum in beams A and B, respectively. Differences between and within a night due to changes in atmospheric seeing are clearly visible. The width of the frame for each night is proportional to the number of spectra per night.

lows unequivocal identification of the width that produces the smallest RMS value; this width is $(1/\ln 2)$ times the spectral resolution of each spectrum. Figure 4.2 shows the spectral resolution obtained for each spectrum and beam on the different nights. General trends are attributable to variations in seeing.

The solar spectrum was derived from a high-resolution spectrum from the digital library of the National Solar Observatory* (Wallace et al., 1996) by convolving it down to the right spectral resolution. The average data spectrum was built by shifting all of the spectra to a common grid using spline interpolation.

The centers of common absorption lines were identified in wavelength values for the solar spectrum and in pixel position for our average data spectrum. Then, a second-order polynomial fit to the solar wavelength and the pixel position yielded the sought wavelength solution. Typical RMS errors in wavelength calibration are $\sim 0.3 \times 10^{-4}$ μm, much less than the typical $\sim 1.6 \times 10^{-4}$ μm spectral resolution of our dataset. Finally, before applying the wavelength solu-

*http://diglib.nso.edu/contents.html

tion to each spectrum, the wavelength solution is shifted back to the spectrum's original wavelength scale. In this way, each spectrum has a slightly different scale, but the interpolation errors associated with the use of a common wavelength scale are avoided.

4.2.3 Telluric Correction

This project consists of the search for water signature in an extrasolar planet atmosphere using ground-based observations; thus, it is evident that the process of cleaning the telluric water signature from our dataset is the most critical step for a successful result. If the telluric water signature were identical to the exoplanetary water signature, then there would be no hope of obtaining a meaningful result. However, since HD 209458b is a planet with much higher temperatures than our own, the spectral water signatures will be different due to the presence of excited lines in the hotter planet's atmosphere (see, for example, Figs. 5.4 or 5.5).

I experimented with three different telluric correction methods (TCMs): (1) telluric water spectra proportional to spectral variability; (2) synthetic water spectra from an atmospheric model; and (3) water spectra from average spectra. They are described below, while their efficacy is discussed in §5.3.

There are two sources of telluric absorption: one due to water molecules, which are not well mixed in the Earth's atmosphere and thus vary on timescales of minutes, and an absorption due to all the other molecules, which are well mixed and do not have a temporal variation. The latter varies only if the observations consist of following a celestial source as it moves across the sky; and hence, they are done through different lengths of atmosphere (different air-

masses). Since the airmass at which each spectrum was observed is known, the dry air absorption (along with the constant part of the water absorption) can be corrected by interpolation (Eq. 4.7). To correct the water spectrum, an estimate of the shape of the water spectrum is required and then the variable water absorption can be removed by finding how much of this telluric-water spectrum is present in each observed spectrum (Eq. 4.10). The three TCM methods differ in the choice of this telluric-water-spectrum estimate. A mathematical justification of the procedure described in this paragraph follows.

If $I_\star(\lambda)$ is the intensity from the stellar system above the Earth's atmosphere, then

$$I_t(\lambda, t) = L(t) I_\star(\lambda)\, e^{-\hat{\tau}_\oplus(\lambda,t) a(t)} \tag{4.1}$$

is the intensity received at the telescope, where $L(t)$ is the slit loss, a is the airmass, and $\hat{\tau}_\oplus$ is the telluric atmosphere's optical depth per airmass. The circumflex symbol ($\hat{}$) indicates a quantity given per unit airmass. Note that the airmass, $a(t)$, and the observed spectra, $I_t(\lambda, t)$, are the only known quantities in this equation at this time.

The optical depth can be separated into the contribution due to water vapor and the contribution due to dry air; such terms are indicated with the subscripts w and d, respectively. Adding a noise term, E, and indicating the dependence in time and wavelength explicitly yields

$$\begin{aligned}
\hat{\tau}_\oplus(\lambda, t) a(t) &= \left[\hat{\tau}'_w(\lambda, t) + \hat{\tau}_d(\lambda)\right] a(t) + E(\lambda, t) \\
&= \left\{\hat{\tau}_w(\lambda)\left[1 + \delta(t)\right] + \hat{\tau}_d(\lambda)\right\} a(t) + E(\lambda, t) \\
&= \hat{\tau}_w(\lambda)\delta(t)a(t) + \left[\hat{\tau}_w(\lambda) + \hat{\tau}_d(\lambda)\right] a(t) + E(\lambda, t) \\
&= \hat{\tau}_w(\lambda)\delta(t)a(t) + \hat{\tau}_c(\lambda)a(t) + E(\lambda, t),
\end{aligned} \tag{4.2}$$

where $\hat{\tau}_c = \hat{\tau}_w + \hat{\tau}_d$ incorporates the contributions from terms varying only with airmass. Also, the temporal variation of the water spectrum due to varying water column has been assumed to be a small perturbation (δ) from its average value. Then,

$$|\delta(t)\hat{\tau}_w| < |\hat{\tau}_c|. \tag{4.3}$$

It is also safe to assume that

$$|\delta(t)\hat{\tau}_w(\lambda)| \gg |E(t,\lambda)|, \tag{4.4}$$

or, in other words, that most of the temporal variation in the optical depth is due to variation of the amount of water vapor. The normalization of the spectra in §4.2.1 allows an extra constraint:

$$\begin{aligned} L(t) &\approx 1 \\ \ln L(t) &\approx 0. \end{aligned} \tag{4.5}$$

Using Eq. (4.2) in the logarithm of Eq. (4.1) yields

$$\ln[I_t(\lambda,t)] = \ln[L(t)] + \ln[I_\star(\lambda)] - \left[\hat{\tau}_c(\lambda) + \delta(t)\hat{\tau}_w(\lambda) + \hat{E}(\lambda,t)\right] a(t). \tag{4.6}$$

This equation contains additive terms that are easier to manipulate.

The error term, $\hat{E}(\lambda,t)$, and the slit term, $L(t)$, are ignored for the rest of this section due to Conditions (4.4), and (4.5).

Then, if Condition (4.3) is used in addition, Eq. (4.6) becomes a linear equation that can be fit in time (for each wavelength):

$$\underbrace{\ln\left[I_t(\lambda,t)\right]}_{Y_i(\lambda)} = \underbrace{\ln[I_\star(\lambda)]}_{T_0(\lambda)} \underbrace{-\hat{\tau}_c(\lambda)}_{+S_0(\lambda)} \underbrace{a(t)}_{X_i(\lambda)}, \tag{4.7}$$

where S_0 and T_0 refer to the slope and the intercept of this first fit. The index i refers to each spectrum. Note that it is not recommended to use T_0 to obtain

the value of $I_\star$, since the value of a fitted intercept is always less certain than the value of a fitted slope. Rearranging the terms, Eq. (4.6) becomes

$$\ln[I_t(\lambda,t)] - \hat{\tau}_c(\lambda)a(t) = \ln[I_\star(\lambda)] - \delta(t)\hat{\tau}_w(\lambda)a(t), \tag{4.8}$$

where all the terms on the left side are known.

The three methods described below (TCM-m, $m = 1, 2, 3$) obtain a spectrum, $P_m(\lambda)$, which is proportional to the optical depth such that

$$K_m(t)P_m(\lambda) = \hat{\tau}_w(\lambda)\delta(t)a(t). \tag{4.9}$$

Then, K_m can be found as the slope of a linear fit to Eq. (4.8):

$$\underbrace{\ln[I_t(\lambda,t)] - \hat{\tau}_c(\lambda)a(t)}_{Y_j(t)} = \underbrace{\ln[I_\star(\lambda)]}_{T_m(t)} \underbrace{-K_m(t)}_{+S_m(t)} \underbrace{P_m(\lambda)}_{X_j(t)}, \tag{4.10}$$

where S_m and T_m refer to the slope and the intercept for each of the TCMs. The index j refers to each wavelength channel.

Telluric Water Proportional to Spectral Variability: TCM-1

The RMS of the fit (σ_0) in Eq. (4.7) for each wavelength will give a measure of how variable water is in that channel. Due to Condition (4.3), it is possible to assume that the variability is due to the variable $\delta(t)$. Hence, σ_0 is proportional to τ_w. According to the quantities defined in Eq. (4.9):

$$P_1 = \sigma_0. \tag{4.11}$$

The leftmost frame from Fig. 4.3 shows an example dataset cleaned by this method. It is clear that not all telluric features are removed.

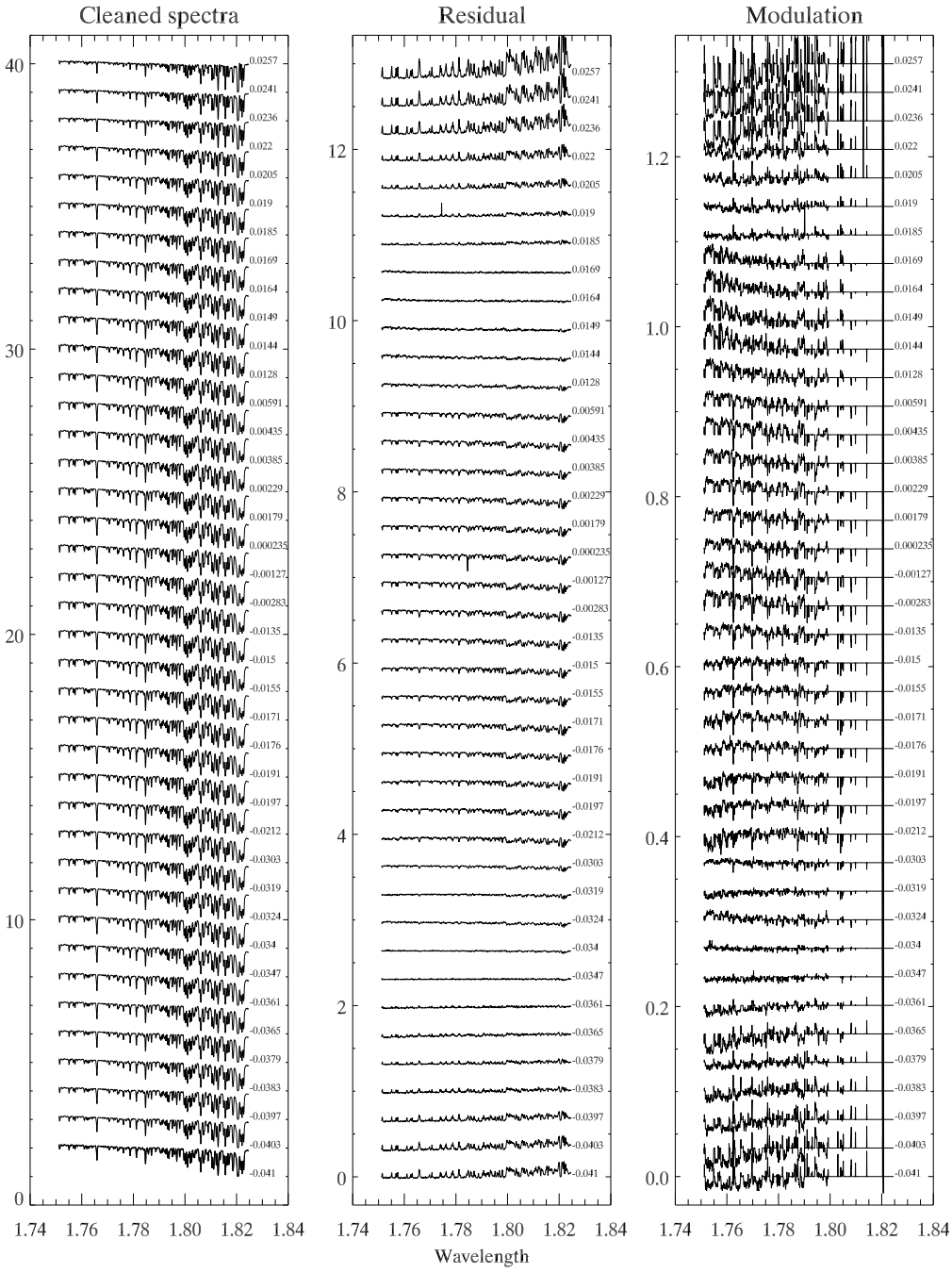

Figure 4.3: Example of telluric correction method 1. Spectra shown are from beam A observations on the night of Aug 4th, 2002. Orbital phase is shown next to each spectrum (transit occurs roughly from -0.02 to 0.02). Vertical arbitrary offsets are added to each spectrum for display. Left: Each spectrum after being corrected by TCM-1. Middle: Residual spectra (each spectrum from left frame after subtraction of the average spectrum). Right: Modulated spectra (each spectrum from leftmost frame after division by the average spectrum).

Synthetic Water Spectrum From Atmospheric Model: TCM-2

The second method simply consists of using molecular line information to create a synthetic water opacity spectrum (κ_w). Then, according to the quantities defined in Eq. (4.9):

$$P_2 = \kappa_w. \tag{4.12}$$

The telluric spectrum was provided by T. Hewagama (private communication). His model is based on the same principles described in §3 but for normal ray geometry. He uses standard composition, temperature, and pressure profiles for the atmosphere of the Earth, which are then adjusted to the altitude of the telescope. However, local weather variations have an effect on the atmospheric thermal profile, and thus it is not possible to use a model that reproduces exactly the actual telluric spectrum during the time of the observations.

The leftmost frame from Fig. 4.4 shows an example dataset cleaned by this method. Telluric features left with this method are different but have similar intensity than those left with the first method.

Water Spectra from Average Spectra: TCM-3

Following the approach of Richardson et al. (2003b), all the spectra are corrected to their minimum common airmass, $\bar{a}$, using the dry air spectrum obtained by the linear fit of Eq. (4.7):

$$\ln[I_{\bar{a}}(\lambda, t)] = \ln[I_t(\lambda, t)] - \ln[I_\star(\lambda)] + \hat{\tau}_c(\lambda)\bar{a}(t) \tag{4.13}$$

Next, each corrected spectrum is spline-interpolated to a common wavelength scale. An average corrected spectrum is then constructed from only those spectra corresponding to out-of-transit observations, $< \ln(I_{\bar{a}}) >$. If, as expected,

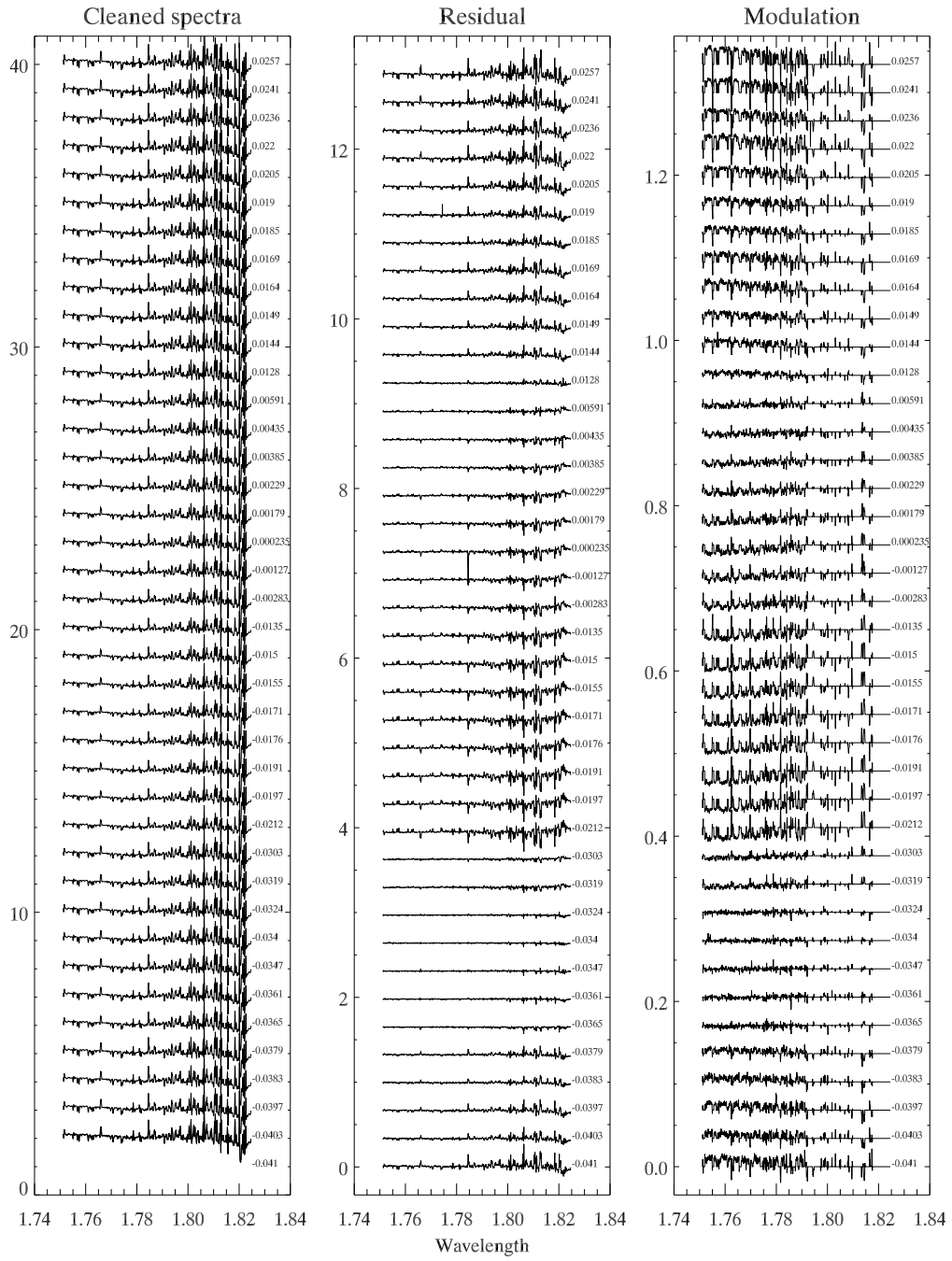

Figure 4.4: Example of telluric correction method 2. See caption in Fig. 4.3 for a description.

the strongest features in the corrected spectra are the telluric water-vapor absorption lines, then, as before

$$P_3 = < \ln(I_{\tilde{a}}) > . \tag{4.14}$$

The leftmost frame from Fig. 4.5 shows an example dataset cleaned by this method. No strong telluric features are visible.

4.2.4 Channel Masking

All three of the methods described above fail to remove the variability in the spectra completely; otherwise the center frames of Figs. 4.3–4.5 would be completely flat to the order of 10^{-4}. Hence, it is necessary to identify those wavelength channels whose intensity is still varying above a certain threshold, and mask them out from further analysis. To identify these channels, the spectra were first spline-interpolated to a common wavelength scale and then the standard deviation of the intensity was calculated at each of these common wavelength channels (σ_λ, Fig. 4.6). Those values that were bigger than n times the standard deviation of the per-wavelength standard deviation, σ_λ, were removed from further analysis (n was set by trial and error to 0.5). One extra channel on each side of each outlying region was also masked out to avoid the wings of the peaks in σ_λ.

Note that because each spectrum has a different wavelength scale, each spectrum possesses a different pixel mask. Sometimes different numbers of pixels were masked out between spectra from the same dataset (same night and beam). Typically, about 38% of each spectrum was masked out.

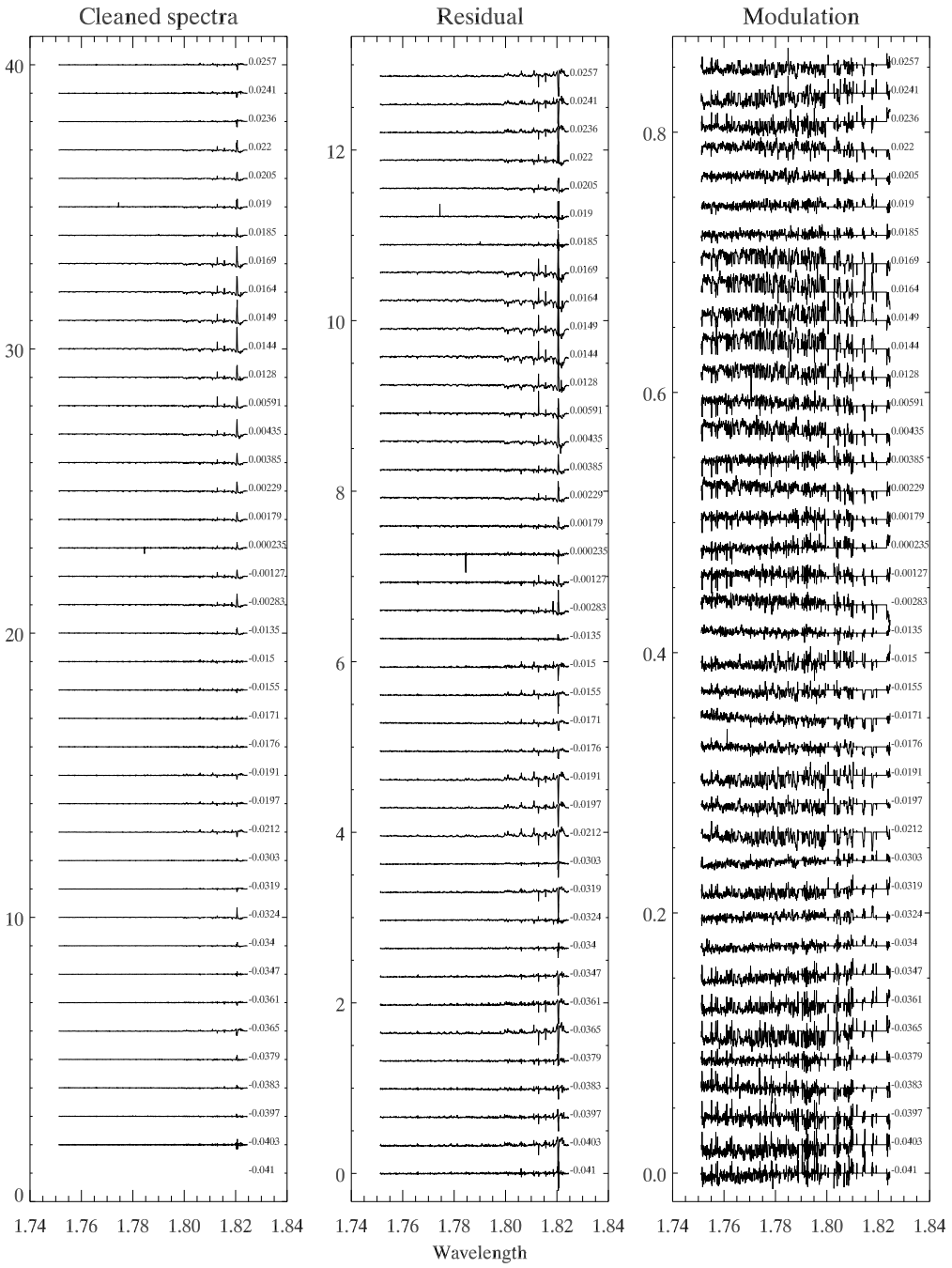

Figure 4.5: Example of telluric correction method 3. See caption in Fig. 4.3 for a description.

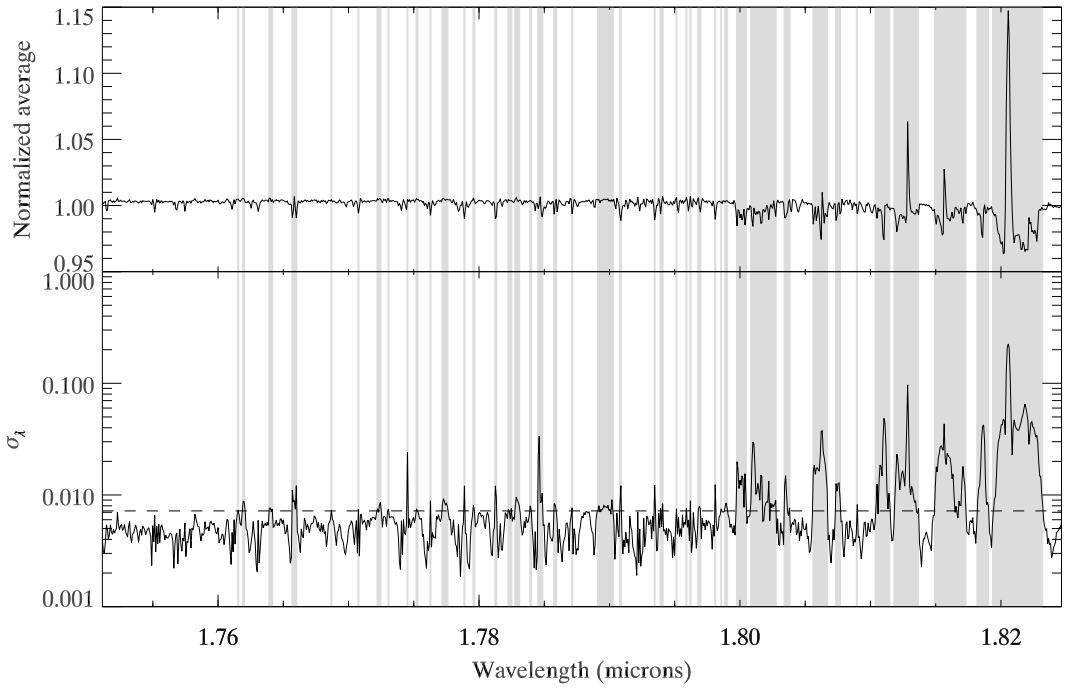

Figure 4.6: Average spectrum and standard deviation. Example prepared using beam A observations of Aug 4th, 2002, as processed by TCM-3. Grey regions indicate wavelength ranges that have been masked out from further analysis due to outlying values of σ_λ. Top: Average normalized spectrum. Bottom: Standard deviation per wavelength channel (σ_λ); vertical line indicates the limit above which wavelength ranges were masked out.

4.3 Analysis

This section describes how a cleaned spectrum (as returned after being processed by the procedure in the previous section) was converted into a modulation spectrum and then how it was compared with the theoretical modulation.

4.3.1 Modulation

Theoretically, the modulation spectrum (Eq. 3.1) is obtained by dividing each planetary system spectrum by the stellar spectrum. In practice, however, the modulation is obtained by dividing each spectrum by the out-of-transit average

spectrum. Because planetary thermal emission and scattering are minimal compared to stellar emission (see §3.2.2), this average spectrum is equivalent to the stellar spectrum.

Given that each reduced spectrum has not been interpolated to a common wavelength scale (see §4.2.2), there are three methods that could be applied to obtain a modulation spectrum:

1. Each spectrum is spline-interpolated to a reference wavelength scale. Then all spectra in the common scale are averaged. This average spectrum is then spline-interpolated back to the wavelength scale of each spectrum before dividing it.

2. The same average spectrum is obtained by spline interpolating each spectrum to a reference wavelength scale. However, the modulation is now obtained by dividing the spectra in the reference wavelength scale by the average spectrum. In this way, all the modulation spectra share a common wavelength scale.

3. An average spectrum is built for the wavelength scale of each of the spectrum by spline interpolating all the others to every particular scale. Then, each spectrum is divided by the average spectrum corresponding to its wavelength scale. This method has the greatest advantage in terms of having just one interpolation per modulated spectrum (furthermore, the interpolated spectra are averaged); however, it can be argued that this method does not give a common stellar spectrum but several stellar spectra (one per wavelength scale).

Using the correlation technique (to be introduced in the following section)

the use of the third method for the analysis in this work is justified (see Fig. 4.8).

4.3.2 Correlation

A standard method to assess similarity between the modulation model and the modulated spectra is to compute their correlation. Mathematically, the correlation ($\mathcal{C}$) between two arrays $\{X_i\}_{i\in[0,N]}$ and $\{Y_i\}_{i\in[0,N]}$ is defined as

$$\mathcal{C} = \frac{\sum_{k=0}^{N}\left(X_k - \bar{X}\right)\left(Y_k - \bar{Y}\right)}{\sqrt{\left[\sum_{k=0}^{N}\left(X_k - \bar{X}\right)^2\right]\left[\sum_{k=0}^{N}\left(Y_k - \bar{Y}\right)^2\right]}}, \tag{4.15}$$

where the barred variables are the averages of each array (or spectrum). The correlation value ranges from -1 to 1. Normalizing the correlation as above has one very important property: the correlation remains the same after an arbitrary linear transformation of any of the arrays. If the slope of the linear transformation is negative, then the correlation result will just change signs. A value of 1 or -1 thus indicates that the arrays are scaled versions of each other; on the other hand, a value of 0 indicates that the arrays are completely uncorrelated. Values in between indicate degrees of correlation.

The successful detection of the modeled modulation in the dataset is attained when the values of the correlation for the spectra corresponding to in-transit observations are clearly distinguishable from the values of the correlation for the spectra corresponding to out-of-transit observations.

Figure 4.7 shows the correlation values (solid lines), their averages, and their respective standard deviations for all the transit nights (see also Table 4.3). It is clear that no transit signature is detected: the in-transit ($|\text{phase}| \leq 0.0189$) correlation values are not distinguishable from the out-of-transit values. Implications of this result are discussed in §5.1.

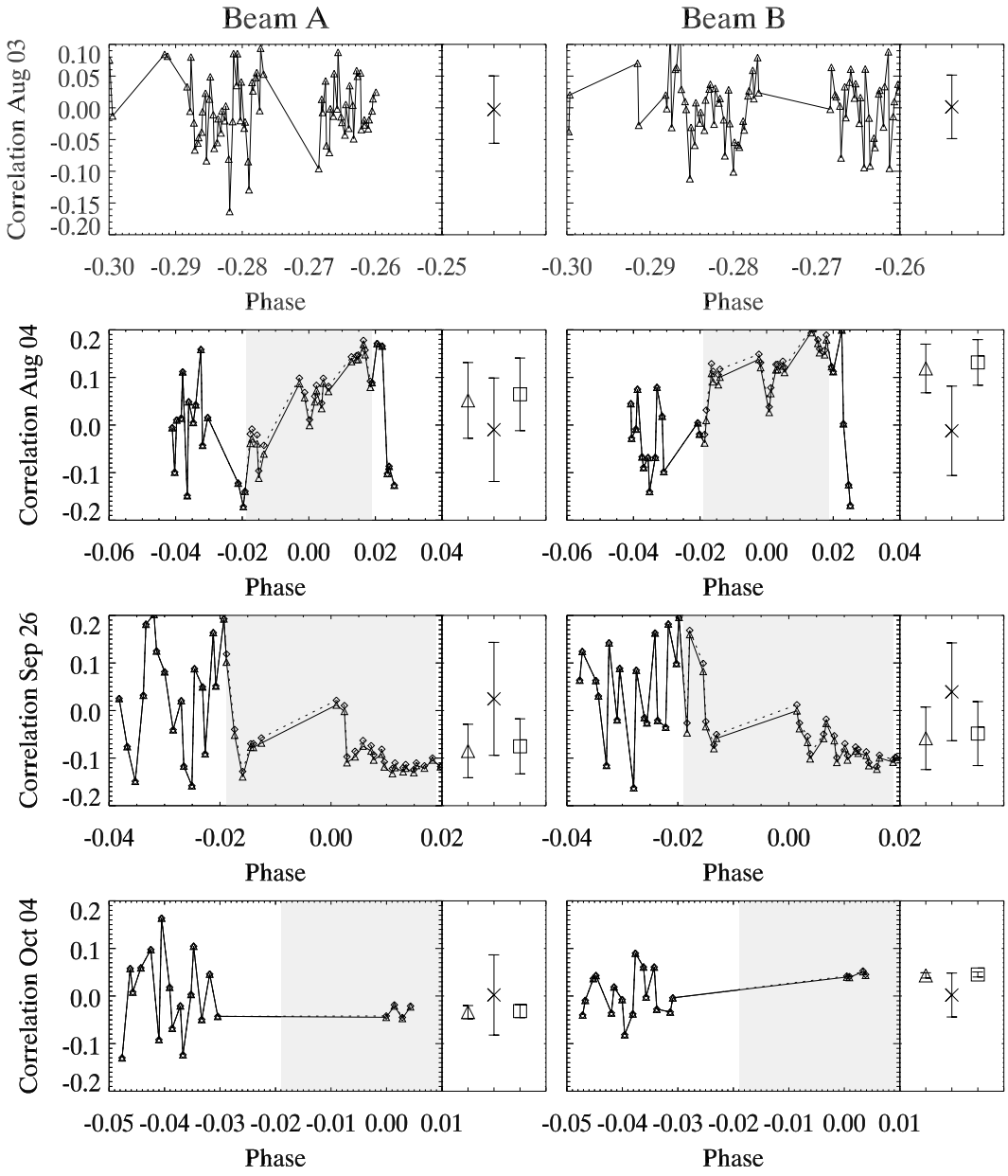

Figure 4.7: Correlations and their per-dataset averages. The left and right frames show the results for beams A and B, respectively. The left side of each frame shows the correlation values for the different spectra. The solid line indicates the results from the real data. The dotted line indicates the results for the synthetic data obtained by adding the modulation due to HD 209458b to the in-transit real data (see §4.4). On the right side of the frame, the symbols triangle, diamond, and square are the average correlation of the out-of-transit, in-transit-real, and in-transit-synthetic spectra, respectively. The standard deviation is indicated with error bars. The gray shaded area indicates the in-transit phases.

Table 4.3: Averages and standard deviations of the correlation for all the nights with a transit event.

Night	Beam	In-transit		Out-of-transit		Synthetic Transit	
		average	σ	average	σ	average	σ
Aug 04	A	0.0518	0.0796	-0.0098	0.1088	0.0645	0.0764
	B	0.1189	0.0511	-0.0122	0.0939	0.1316	0.0480
Sept 26	A	-0.0850	0.0562	0.0246	0.1187	-0.0752	0.0578
	B	-0.0584	0.0657	0.0393	0.1028	-0.0485	0.0672
Oct 03	A	-0.0339	0.0139	0.0022	0.0842	-0.0315	0.0138
	B	0.0434	0.0055	0.0022	0.0462	0.0453	0.0053
Total		0.0061	0.0215	0.0077	0.0389	0.0144	0.0212

Figure 4.8 compares the resulting correlations obtained from the three modulation methods described in §4.3.1. They are found equivalent, and thus only the results obtained by the third method (average spectra are built for each wavelength scale) are presented here.

Figure 4.9 presents the resulting correlation from the different nights using the three methods: TCM-1, TCM-2, and TCM-3. They all behave differently, but TCM-3 has the smallest scattering of values.

4.4 Tests with Synthetic Spectra

To test the sensitivity of the pipeline to exoplanetary water, a synthetic spectrum from `transit` was inserted only into the spectra that were taken during transit. This synthetic dataset was created by multiplying the appropriate spectrum by the modulation obtained from the model. The synthetic spectrum was

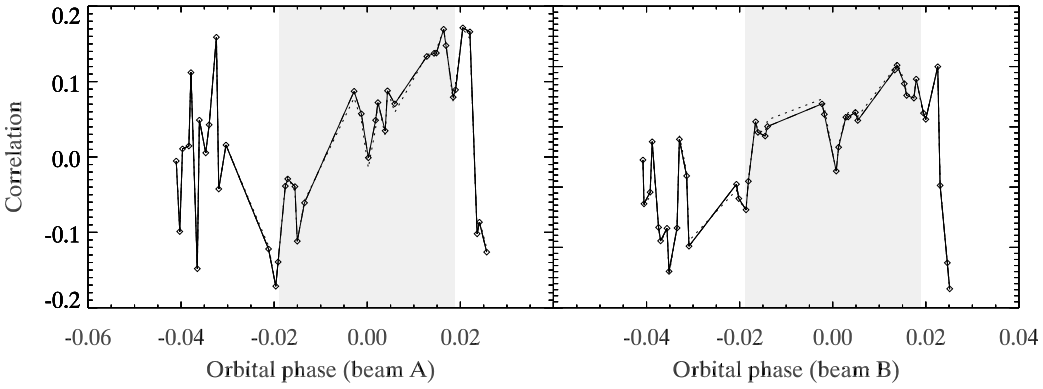

Figure 4.8: Comparison of modulation methods for the night of Aug 4th, cleaned by TCM-3. The left and right frames indicate beams A and B, respectively. Solid lines (with diamonds) indicate correlation results using the average spectrum in the reference wavelength scale spline interpolated to each frame's wavelength scale (method 1). Dotted lines are the correlation result obtained using the average spectrum and each frame spline interpolated to the reference wavelength scale (method 2). Dashed lines (which are undifferentiated from the solid lines for the most part) are obtained by using average spectra built for each of the wavelength scales (method 3).

then processed through all the calibration and telluric correction routines (see Fig. 1.6). Even though the resulting correlation is slightly different from what was obtained for the real, in-transit spectra, it is found that the out-of-transit and in-transit synthetic spectra are still undifferentiated (See rightmost two columns in Table 4.3 and dotted line in Fig. 4.7).

However, if the modulation is scaled (Appendix D.3) to that which would have been obtained from larger planets with differing atmospheric scale heights, the correlation values are found clearly distinguishable (Fig. 4.10). This confirms that the analysis strategy is effective and that it is able to differentiate water in a planetary system from the telluric water when the extrasolar system has a minimum size ratio between the planetary atmosphere and the star. Discussion about these minimum conditions is left to §5.2.

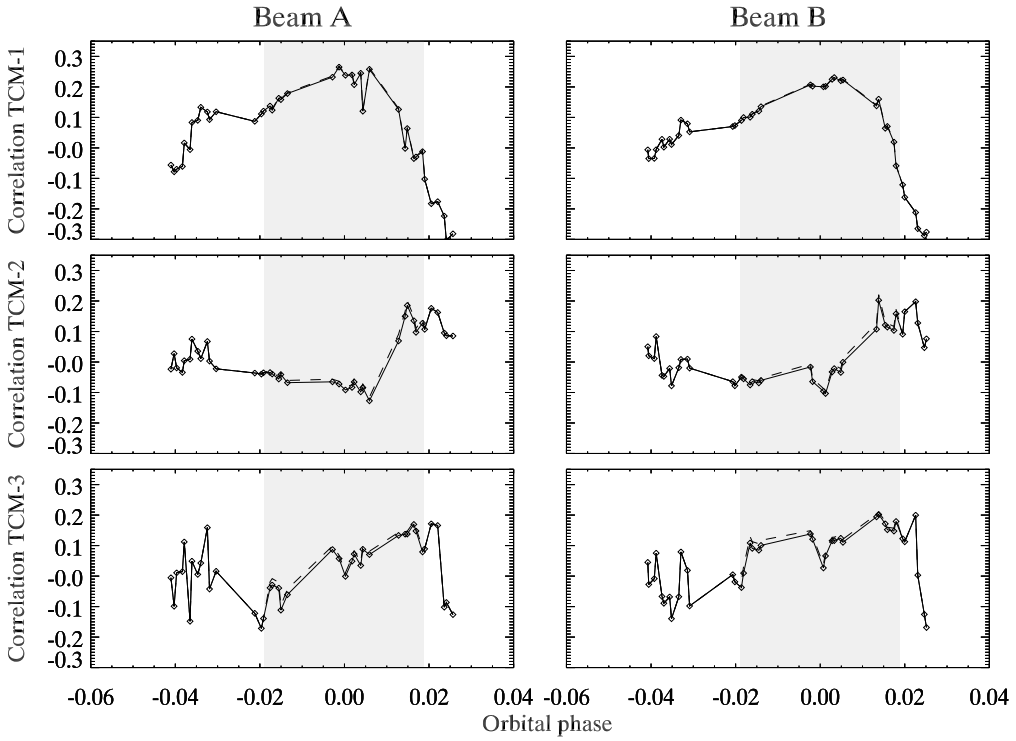

Figure 4.9: Comparison of telluric correction methods for real and synthetic data. The frames show the correlation obtained for the data of Aug 4th for each of TCM-1, TCM-2, and TCM-3, from top to bottom, respectively. Solid lines (with diamonds) indicate real data, while dotted lines indicate the result from the synthetic data. The left frames show the results from beam A and the right frames the results from beam B. Shaded area indicates in transit period.

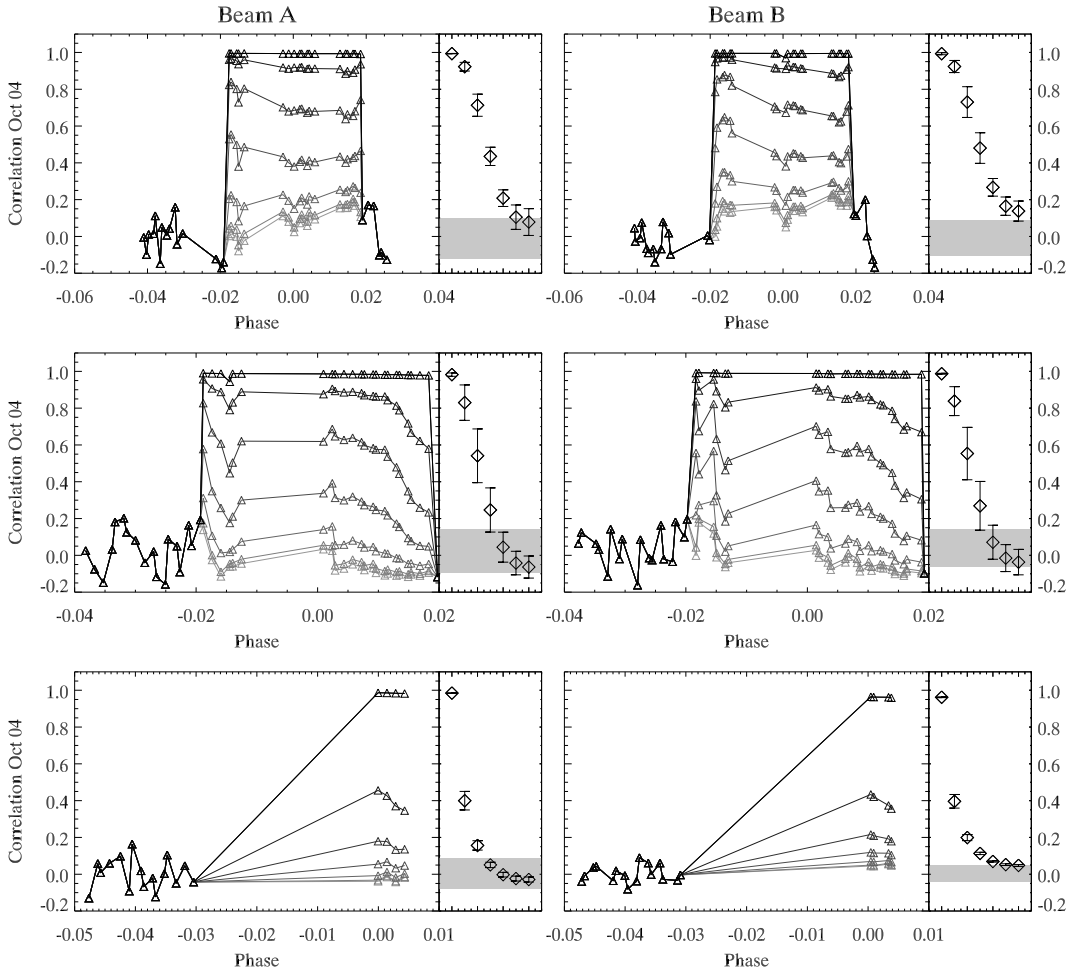

Figure 4.10: Correlation tests with synthetic spectra for TCM-3. The other telluric correction methods show the same behavior. The left and right frames show the result for beams A and B, respectively. The left side of each frame shows the correlation values for the different spectra. The different synthetic curves correspond to transiting planets of different scaled radii and atmospheric scale heights (the parameters for each of these curves, except the topmost one, are shown in Fig. 5.1; more information is given in that caption). The bottom curve corresponds to results from HD 209458b's real data and not a synthetic dataset. The right side of each frame shows the average in-transit correlation values.

Results | 5

Important results from this work include the significance of the non-detection of water, analysis on the limits for this detection, new methods developed to optimize future observations, and the new method to remove fringes from flat fields using wavelets. The latter has been reported in a paper accepted by The Astrophysical Journal (Rojo and Harrington, 2006); hence, a copy of that paper is included at the end of this chapter.

5.1 Non-Detection of Water

This section discusses the significance of the null result and address the circumstances under which a detection would have been possible.

Table 4.3 clearly shows that none of the nights exhibit any significant detection of water in the atmosphere of HD 209458b. Furthermore, the failure to recover the signal after injecting a synthetic modulation, as described in §4.4, implies that even if water were present in HD 209458b, the analysis would not have detected it (rightmost two columns in Table 4.3).

Why did this work not detect HD 209458b's atmosphere while other groups did? To this date, all the other successful detections have been through the observation of bulk IR thermal emission (Charbonneau et al., 2005, Deming et al.,

2005b, 2006, Harrington et al., 2006) or the analysis of strong and isolated lines of atoms in the visible and ultraviolet region of electromagnetic spectrum (Charbonneau et al., 2002, Vidal-Madjar et al., 2003, 2004, see §2). Molecules like water, on the other hand, lack strong, single-lined features; their spectral signatures consist of many relatively weak lines blended together that appear mostly in the IR region of the electromagnetic spectrum. Furthermore, IR detectors are not as efficient as optical CCDs and there are more noise sources (like thermal emission from the telescope itself). Other efforts to this date to detect molecules have only yielded upper limits (Richardson et al., 2003b, Deming et al., 2005a). Nonetheless, even those measurements do not face the extra difficulty associated with measurements of water using ground-based telescopes: water has the most variable abundance in the Earth's atmosphere, while all the other molecules are well mixed and stable.

This variable telluric water signature is embedded in every spectrum obtained from ground based observations. However, because the signature of water from the extrasolar atmosphere is expected to be different (see §4.2.3 and Fig. 5.5), a successful correction of telluric water at high-wavelength resolutions was expected. Differences in the correlation values per night obtained with the different telluric correction methods (Fig. 4.8) hint that they do not share the same effectiveness in removing telluric features, despite each of them having a reasonable justification. Thus, at least two of them are not totally reliable in eliminating telluric water spectra without affecting the exoplanetary signature. In the previous chapter, §4.4 demonstrated that the pipeline is functional and that the analysis is not sensitive to the presence of water in a synthetic dataset. Hence, the only explanation left for the null result is that the chosen wavelength

range has too much variable telluric water, which is overwhelming any signal there may be from the modulation: a minute error in the correction of telluric spectra (in any of the TCMs) implies that the exoplanetary water signature is completely lost. This problem was exacerbated due to the average ~ 1.6 airmass (Fig. 4.1) in the observations.

5.2 Limits on Sensitivity

This section explores the use of analytical approximations to extrapolate the sensitivity estimates from §4.4 to planets with different values of scale height, H, and the radius of the most-transparent wavelength in a given range, r_1.

The approximations include isothermal, cloudless atmospheres with similar composition among the planets. Under those circumstances (see Appendix D.3) it is found that

$$\Delta\mathcal{R}_\lambda \propto \frac{r_1 H}{R_\star^2}, \tag{5.1}$$

where $\Delta\mathcal{R}_\lambda = \mathcal{R}_{high} - \mathcal{R}_{low}$ is the range in modulation between the most ($\mathcal{R}_{low}$) and the least ($\mathcal{R}_{high}$) transparent wavelengths in the given range, and $R_\star$ is the radius of the star.

Therefore, the values of the modulation extremes can be calculated according to

$$\begin{aligned} \mathcal{R}_{low} &= \left(\frac{r_1}{R_\star}\right)^2 \\ \mathcal{R}_{high} &= \mathcal{R}_{low}\left(1 + 2aH/r_1\right), \end{aligned} \tag{5.2}$$

where a is the proportionality constant, which is obtained by using $\mathcal{R}_{low}$ and $\mathcal{R}_{high}$ from the reference atmosphere, in this case HD 209458b's.

Once the extreme values are obtained, the reference modulation spectrum is linearly transformed to coincide with the new extreme values. This modified spectrum is then used to build the synthetic spectrum and obtain correlations as described in §4.4.

Detection level $\mathcal{D}$ is defined as

$$\begin{aligned} \mathcal{D} &= \left| \frac{\bar{\mathcal{R}}_{\mathrm{T}} - \bar{\mathcal{R}}_{\mathrm{oT}}}{\sigma} \right| \\ &= \left| \frac{\bar{\mathcal{R}}_{\mathrm{T}} - \bar{\mathcal{R}}_{\mathrm{oT}}}{\sigma_{\mathrm{oT}} + \sigma_{\mathrm{T}}} \right|, \end{aligned} \tag{5.3}$$

where each night has been separated between in-transit (T) and out-of-transit (oT) spectra only (results from beams A and B have been combined). $\bar{\mathcal{R}}_{\lambda}$ represents the average correlation value and σ is the standard deviation of the correlations.

Figure 5.1 shows a contour plot where the surface boundaries represent constant detection confidence levels $\mathcal{E}$. Plots like this are specific to the conditions of each observing night, but planets with different characteristics can be easily located on it. All of the known transiting planets are below the 1-σ confidence level for the data obtained with the atmospheric conditions of Aug 04.

An important result of this work comes from bringing together the automated data reduction routines described in §4 and the routines to make Fig. 5.1. Future observations of newly discovered extrasolar planets could, using these routines, effectively obtain a confidence level estimate for the atmospheric conditions of each particular observation within hours of finishing it.

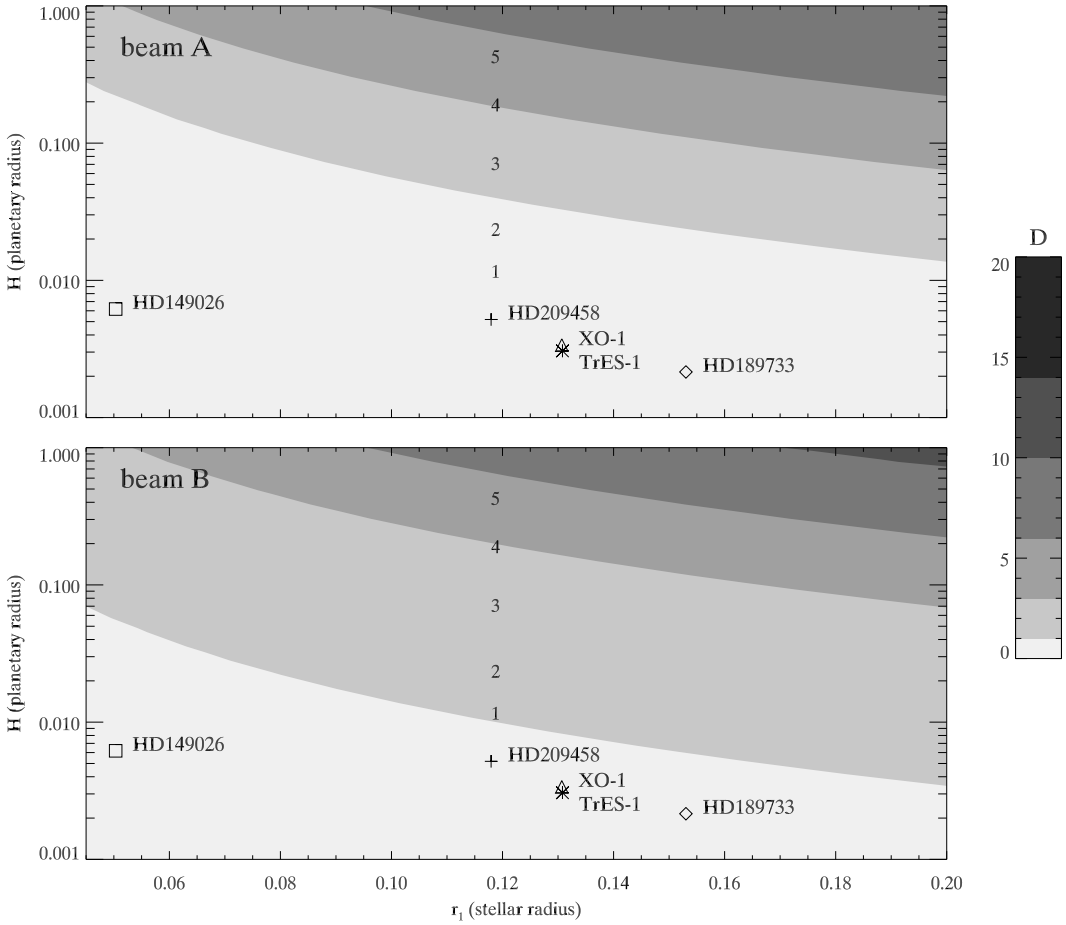

Figure 5.1: Contour plots of the detection level $\mathcal{D}$ for each of the nights of August 2002 using TCM-3. The top and bottom frames show the result for the different beams. The solid diamond indicates the position of the reference system, HD 209458b. A cross indicates indicates HD 209458b, a square indicates HD 149026b, a diamond indicates HD 189733b, an asterisk and a triangle (which appear overlapped) indicate TrES-1 and X0-1b, respectively. The numbers from 1 to 5 indicate the scaling parameters for the different synthetic datasets of Fig. 4.10, from top to bottom, respectively. In Fig. 4.10 the uppermost curve is beyond the scale of this plot.

5.3 Selection of Parameters for Future Observations

This section discusses how to apply the experience of this work to improve future observations that attempt measurements of exoplanetary atmospheres.

As argued in the previous sections, the main problem for this work was too much telluric variability. This problem obviously disappears if using space telescopes. However, their instrumentation and availability are very limited; in today's space telescopes, there are no spectrographs that have yet detected atmospheric water on an extrasolar planet.

For future ground-based observations, there are three points that must be considered carefully to improve the results:

1. Observe the planetary system through less variable telluric water. There are two measures that can be taken to ensure the least possible telluric water: to choose the right time and to choose the right telescope. The latter implies using telescopes located in dry climate locations, at high altitudes, and with a geographic latitude near the object's declination. The choice of time is very restricted because the transit events occur at regular periods of typically a few days long. Plots like the one in Fig. 5.2 can be used to investigate the best possible time for observations.

2. Simultaneously observe a non-variable star as a calibrator. Ideally, such a star will exist so close to the planetary system that both could be placed in the spectrograph's slit simultaneously. If they are not that close, then there are two issues to consider (other than that they might be experiencing different telluric conditions): overhead time due to pointing and movable pieces in the telescope. The former refers to the time the telescope requires

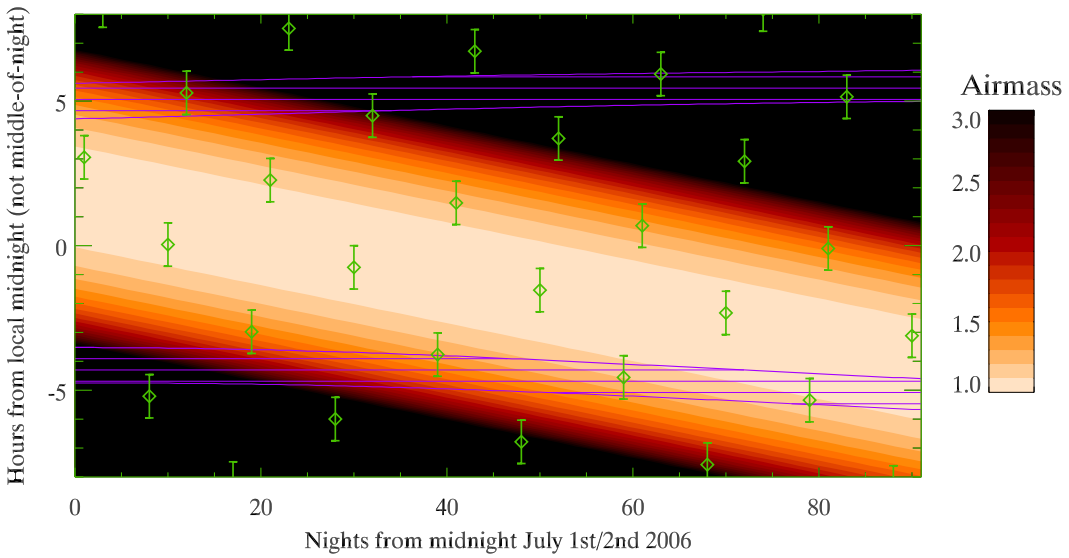

Figure 5.2: Diagram to help in the selection of the best observable transit events. The diamonds indicate the center of the transit events for HD189733b; vertical error bars indicate transit span (ephemeris of Bakos et al., 2006). The configuration is as observed from Mauna Kea, Hawaii. Solid contour boundaries indicate airmass. Blue line-filled regions indicate the morning and evening twilights.

to move between objects and, if applicable, tune its optics. In telescopes up to about 5 m in diameter, it is easy to find a calibrator star close enough that much less than one minute will be lost per slew. However, for large modern telescopes with complex optics, the time required from the start of motion to stability can be greater than 10 minutes (and likewise when going back to the planetary system).

The second issue, movable pieces, is also very important. At the VLT (and Keck, Deming et al., 2005a), sometimes when the telescope returned from the calibrator, the correlation had suffered a discontinuity with respect to the value it had before due to wavelength shift. This, however, has not been observed with all spectrographs.

3. Choose a wavelength range with less telluric variation. An original but

simple technique was developed to estimate the wavelength range with the best chance of success. This technique uses the variability of the telluric signature (mainly telluric water) and that the amount of variability is proportional to the absorption coefficient at the particular wavelength. The lack of techniques like this when choosing the wavelength range for the observations of this work is the main reason why the chosen wavelength range was not the best one.

Since the wavelength range is relatively small for the large-scale structures to be observed (see, for example, the saw-tooth-like modulation in the middle plot of Fig. 3.8), the effort is given to detect only the modulation contrast between close-by pixels. Hence, a boxcar-filtered version of the modeled modulation is first subtracted from the modeled modulation. The filtered version should be smooth enough to contain minimal variation between neighboring wavelength channels. Then, the resulting spectrum is multiplied by a telluric absorption spectrum (empirical or modeled). Over-plotting the spectrum from before and after the multiplication by the telluric absorption allows simultaneous visualization of the amplitude of the modulation at different wavelengths and the absorption by telluric water (see Fig. 5.3). Repeating this simple procedure for different spectral resolutions or ranges gives an indicator for the best combination of wavelength and resolution, one that has little absorption while at the same time has a modulation range within sensitivity requirements.

The minimum SNR that the observations require to succeed is one that can resolve the contrast between neighboring wavelength channels at the chosen resolution. For example, for HD 209458b's water in the region around

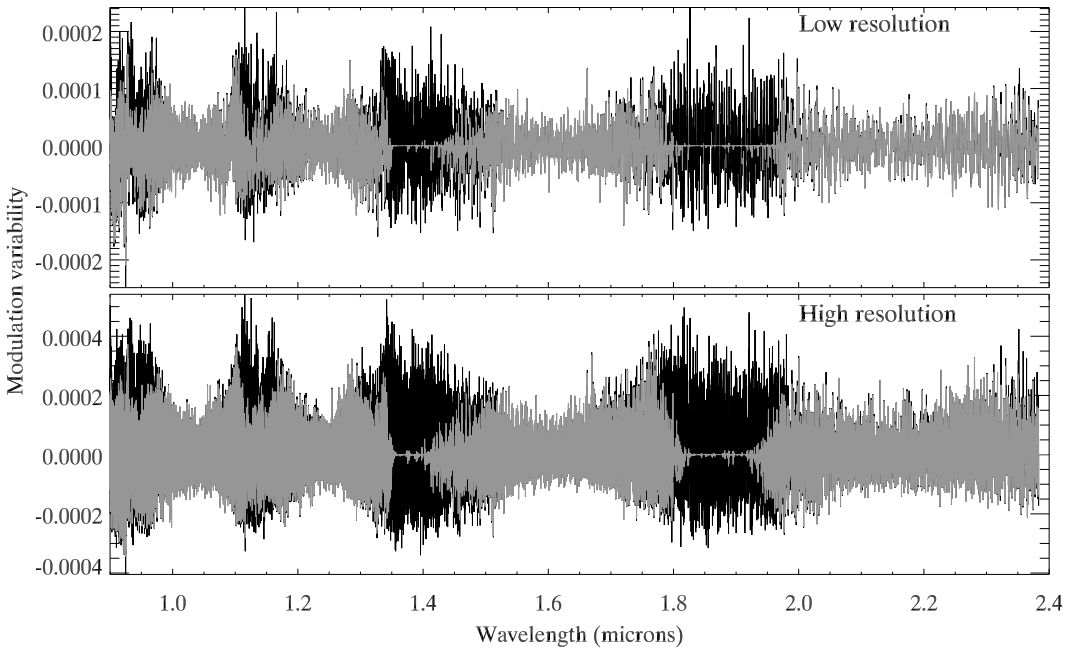

Figure 5.3: Black lines indicate the modulation spectrum after having a boxcar-filter version of itself subtracted. Red lines show the same spectrum after being multiplied by the telluric absorption. The best candidate ranges for a successful observation have a large enough modulation between adjacent wavelengths while at the same time being modified by telluric absorption as little as possible. The bottom frame has a resolution of $\lambda/\Delta\lambda \approx 25\,000$ (equivalent to NIRSPEC at the Keck telescope), the top frame has a resolution of $\approx 3\,000$ (equivalent to ISAAC).

1.6 μm (see Fig. 5.3), the typical contrast of 10^{-4} requires a cumulative SNR* of several times 10^4.

The signatures of other telluric molecules are not variable since they are well mixed in the atmosphere. Although it will then be easier to spot the differences between in-transit and out-of-transit spectra if searching for these molecules, this technique can still be applied to reduce the variability.

*Cumulative SNR is obtained after adding the contribution of all spectra and wavelength channels.

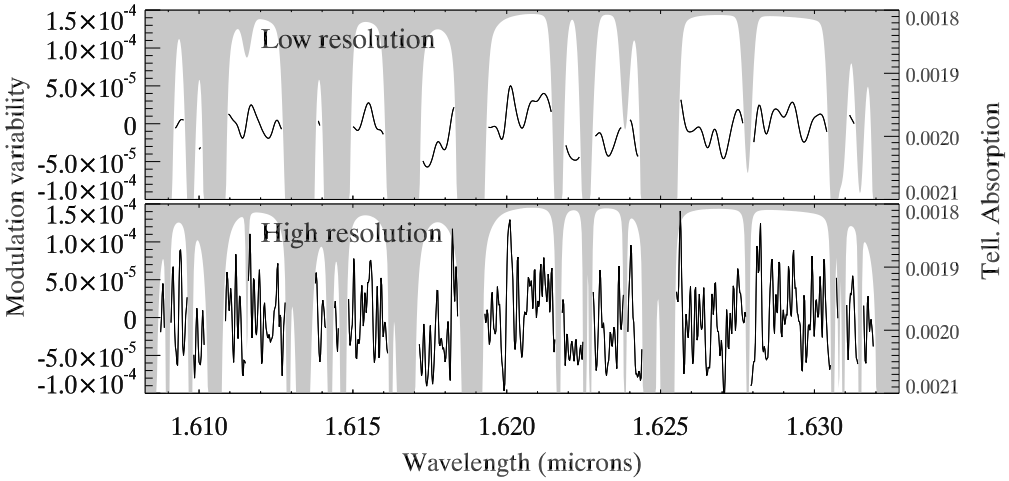

Figure 5.4: Telluric absorption in the 1.6-μm window in a wavelength range appropriate for one order of NIRSPEC at the Keck telescope. The telluric absorption (border of solid grey surfaces, right axis scale) and the exoplanetary water lines (solid lines) are at the same wavelength resolution. The data in the top and bottom frames have resolutions of $\approx 3\,000$ and $\approx 25\,000$, respectively.

This work presents the best result with the data in hand, which were obtained with an unfortunate choice of telescope and wavelength. The telescope was located in the southern hemisphere, while the planetary system is in the northern hemisphere. The wavelength range (around ~ 1.8 μm) was located where there is already too much telluric absorption (see Fig. 5.3 or the close-up in Fig. 5.4). Instead, observations should have been centered around ~ 1.6 μm, where the modulation amplitude is not much smaller than around 1.8 μm but where there is much less telluric absorption (see, for example, Fig. 5.5).

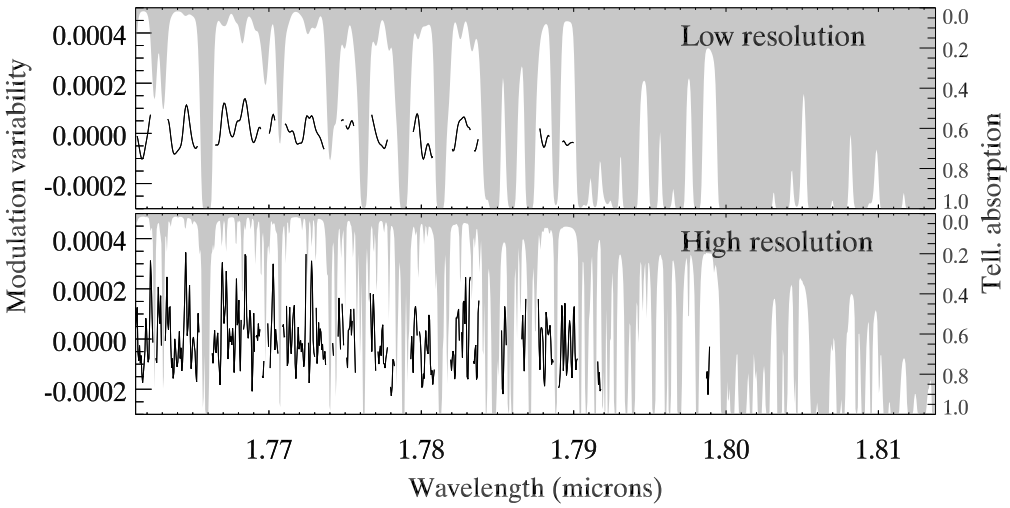

Figure 5.5: Telluric absorption in the wavelength range equivalent to the observations obtained for this work (border of solid gray surfaces, right axis scale) and the exoplanetary water lines (solid lines) at the same wavelength resolution. Note that the telluric absorption is much stronger in this wavelength range than in the range of Fig. 5.4. The data in the top and bottom frames have resolutions of $\approx 3\,000$ and $\approx 25\,000$, respectively.

5.4 A Method to Remove Fringes from Images Using Wavelets

Copy of Paper Submitted to ApJ on November 14, 2005. Accepted on May 20, 2006.

Patricio M. Rojo

516 Space Sciences Building, Center for Radiophysics and Space Research
Cornell University, Ithaca, NY 14853-6801

Departamento de Astronomía, Universidad de Chile, Casilla 36-D,
Santiago, Chile

pato@das.uchile.cl

and

Joseph Harrington

326 Space Sciences Building, Center for Radiophysics and Space Research
Cornell University, Ithaca, NY 14853-6801

current address: Department of Physics, University of Central Florida,
Orlando, FL 32816-2385

jh@physics.ucf.edu

Abstract

We have developed a new method that uses wavelet analysis to remove interference fringe patterns from images. This method is particularly useful for flat fields in the common case where fringes vary between the calibration and object data. We analyze the efficacy of this method by creating fake flats with fictitious fringes and removing the fringes. We find that the method removes 90% of the fringe pattern if its amplitude is equal to the random noise level and 60% if the

fringe amplitude is $\approx 1/10$ of the noise level. We also present examples using real flat-field frames. A routine written in IDL that implements this algorithm is available from the authors and as an attachment to this paper.

Subject headings: methods: data analysis — technique: image processing

5.4.1 Introduction

The current class of telescopes with primary mirrors larger than $\sim$8 m in diameter allows researchers to attain an unprecedentedly high signal-to-noise ratios. In addition, ever-increasing computer capabilities have permitted quantitative analyses able to distinguish trends weaker than the noise level. This has not only allowed observations of fainter objects, but also observations of weak sources spatially indistinguishable from a bright source, such as the spectrum of an extrasolar planet orbiting a main-sequence star. In such cases, systematic errors that would not have been of importance when analyzing the bright source are of concern when considering the fainter source. Previously ignored systematic errors thus require algorithms able to correct them.

One such systematic effect is the appearance of fringes in data arrays. The strength of these fringes varies from instrument to instrument; we have seen it range from less than 1/10 of the noise amplitude to roughly 5 times the noise amplitude.

Fringe correction methods found in the literature are either specific to the instrument or assume a global fringe period (e.g., Malumuth et al. 2003a,b, Mellau and Winnewisser 1995). The latter correction type makes uses of Fourier filtering, a technique that is less than satisfactory in the common case where the pattern's period or amplitude varies over the image. Another common ap-

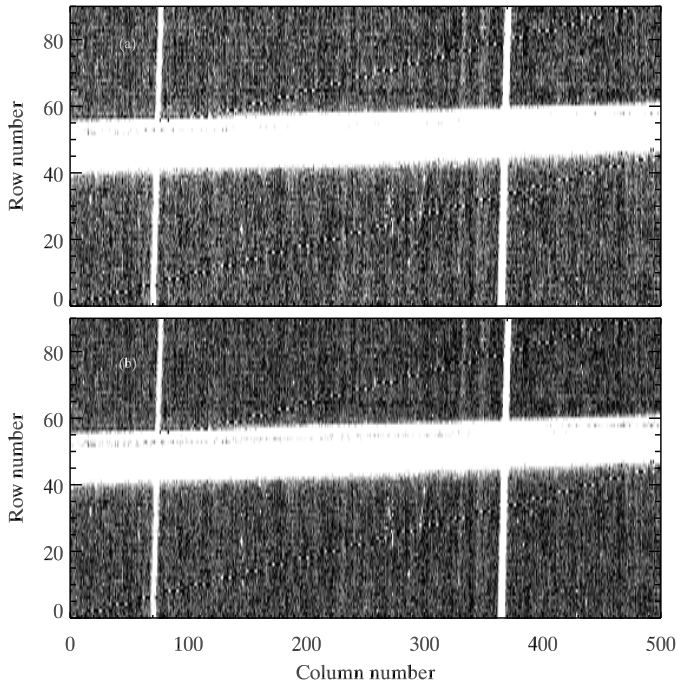

Figure 5.6: Failure of flat field to correct fringes. *Top*: Debiased spectrum frame. *Bottom*: Spectrum frame after flat field and bias correction. The fringe pattern is still visible. These images are subsections of a spectrum frame obtained with NIRSPEC at the Keck telescope. The horizontal white pattern is the spectrum's trace. The bright, white, vertical lines are the sky emission lines.

proach has simply been to ignore the fringes in the hope that division of the debiased data array by the flat field frame will eliminate the pattern, which is supposed to remain the same. However, flat fields and object frames do not always share the same fringe pattern because flexure and variations in the illumination geometry can change the pattern's amplitude or period even on short timescales (Figs. 5.6 and 5.7). Therefore, flat-field division could add a second set of fringes rather than correct the first set.

Here we present an algorithm to clean two-dimensional (2D) arrays that uses the wavelet transform, a local spectral technique (e.g., Starck and Murtagh 2002,

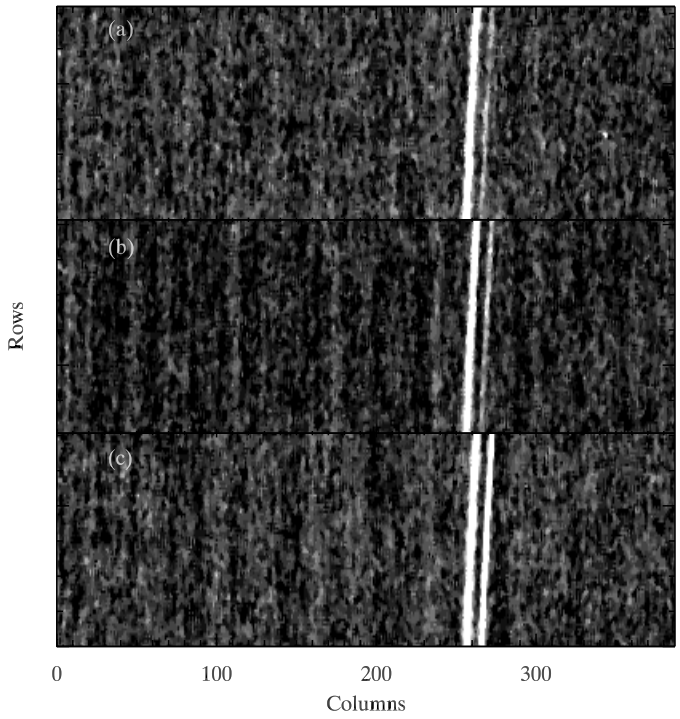

Figure 5.7: Fringe variation in consecutive frames. Shown are subsections of sky frames taken with NIRSPEC on the Keck II telescope (45 s integration). The fringe pattern can be seen varying between these frames. Panels a, b, and c were taken in consecutive order.

Torrence and Compo 1998*). Making use of the wavelet transform's linearity property, the algorithm isolates the fringe pattern in wavelet space, does an inverse transform, and then obtains a clean image by subtracting the reconstructed fringe pattern. The challenge is to do this correctly in the presence of noise. The algorithm presented here is not tuned to any specific data set and has been tested on flat-field frames from ISAAC (Moorwood et al., 1998) at the Very Large Telescope (VLT) and NIRSPEC (McLean et al., 1998) at the Keck telescope.

The algorithm also provides the framework for an extension to remove fringes from object frames by interpolating the fringe pattern over spectra or point sources. Such an extension requires the design of another algorithm to interpo-

*See http://atoc.colorado.edu/research/wavelets/

late fringe parameters, which is beyond the scope of the present work. Thus, our method improves the quality of extracted data when the fringes in the flat fields differ from the fringes in the data, but will not solve the problem completely if the fringes in the data array are significant. We show that there are many cases where the fringes change between arrays obtained at different times.

We implemented our algorithm in IDL (a product of Research Systems, Inc., Boulder, Colorado). The package (defringeflat) includes tutorial documentation. It is available under the GNU General Public License from our Web sites* and as a tar file in the electronic edition of this paper.

Section 5.4.2 gives a mathematical model of fringe formation. Section 5.4.3 describes the algorithm. Section 5.4.4 discusses performance in the presence of noise. Finally, §5.4.5 discusses an applied example, summarizes the benefits and limitations, and presents our conclusions.

5.4.2 Fringes

Fringes are produced by the interference of light reflecting between parallel surfaces in an instrument. They appear in many detectors of visible and infrared light. If we ignore multiple reflections, a mathematical formulation (Rieke, 2003) for the total intensity of light (I_a) received on the position x, y of the detector array is given by

$$I_a(x,y) = I_n(x,y) + I_r(x,y) + 2\sqrt{I_n(x,y) I_r(x,y)} \cos \psi(x,y), \qquad (5.4)$$

*See http://www.das.uchile.cl/∼pato/sw/ or
http://physics.ucf.edu/∼jh/ast/software.html

where I_n is the non-reflected intensity, I_r is the reflected intensity, and ψ is the phase difference between the two beams. We choose the x coordinate such that

$$\psi(x,y) = 2\pi x/P(x,y) + \xi(x,y), \tag{5.5}$$

where P and ξ are the period and phase of the fringe's pattern, respectively. Let I_i be the incoming intensity before interaction with the instrument. Then, $I_r(x,y)$ is proportional to the intensity incident at a nearby position:

$$I_r(x,y) = a(x+\delta x, y+\delta y) I_i(x+\delta x, y+\delta y), \tag{5.6}$$

where δx and δy are small displacements and the factor a includes reflectivity. Note also that $a \ll 1$. If we can assume that the incoming intensity field and the reflection geometry are homogeneous on very short spatial scales, then $a(x+\delta x, y+\delta y) I_i(x+\delta x, y+\delta y) \approx a(x,y) I_i(x,y)$. On the other hand, the non-reflected intensity (I_n) is proportional to the incoming intensity (I_i) in the same coordinate, thus $I_n(x,y) = b(x,y) I_i(x,y)$. Due to energy conservation, the proportionality constant $b(x,y)$ is restricted by the previous assumption to comply with

$$a(x,y) + b(x,y) = s(x,y), \tag{5.7}$$

where $s(x,y) \lesssim 1$ accounts for losses due to scattering and absorption. Omitting the dependence on x and y for clarity, we find for each position

$$\begin{aligned} I_a &= bI_i + aI_i + 2I_i\sqrt{ab}\cos\psi & (5.8)\\ &= I_i\left[s + 2\sqrt{ab}\cos\left(2\pi x/P + \xi\right)\right] & (5.9)\\ &= I_i\left[s + F\right], & (5.10) \end{aligned}$$

where

$$F = 2\sqrt{ab}\cos\left(2\pi x/P + \xi\right) \tag{5.11}$$

is the oscillating fringe term. When interacting with the detector array, Eq. 5.10 is modulated to obtain the detected intensity I_d. Including detection noise, the modulation is given by

$$I_d = I_i \eta \left[s + F \right] + \epsilon, \tag{5.12}$$

where ϵ, which varies rapidly between pixels, includes all noise sources and η includes quantum efficiency, and pixel collecting area, among other factors. On the other hand, η can be decomposed as

$$\eta = \eta_0 + \eta_r, \tag{5.13}$$

where η_0 is the smoothly varying component and η_r is the rapidly varying component, which includes uncorrelated differences between the sensitivities of neighboring pixels. Typically, $\eta_r \ll \eta_0$. Bringing it all together, we obtain

$$I_d = I_i \eta s + \epsilon + I_i \eta_r F + I_i \eta_0 F. \tag{5.14}$$

Our algorithm makes use of the linearity property of wavelets to find and subtract the term $I_i \eta_0 F$, which is the predominant contributor at the period of the fringe pattern. The other terms will only contribute in that frequency to a background level in the amplitude of the wavelet transform. This background is considered in our algorithm (see step 2 in §5.4.3).

Then, ηs can be corrected through flat-fielding to get the sought intensity I_i with a modified noise $\bar{\epsilon}$ given by

$$\bar{\epsilon} = \epsilon + I_i \eta_r F. \tag{5.15}$$

With typical values, $I_i \eta_r F \ll \epsilon$.

Table 5.1: Steps of the Defringing Algorithm

0...	Original image with fringe	Fig. 5.8
1...	*For each row*	
	Compute enhanced row	Fig. 5.9
	Compute wavelet transform	Fig. 5.10
2...	*For each pixel in row*	
	Fit fringe transform's profile	Fig 5.11
3...	*For the whole array*	
	Smooth fit parameters (optional)	Fig. 5.12
4...	*For each row*	
	Reconstruct wavelet array	Fig. 5.10
	Inverse transform	Figs. 5.10, 5.13
	For the whole array	
	Subtract fringe pattern to obtain clean image	Fig. 5.14

5.4.3 Algorithm

The main steps in our procedure are listed in Table 5.1. Figures 5.8 – 5.14 illustrate the steps of the algorithm using an example flat field. Their captions contain details regarding the example array, while the main text only refers to the algorithm in general. The example flat field is included in the defringeflat package.

All array borders whose values are not consistent with the image must be cropped. The fringes are allowed to have several different patterns, which do not need to look like straight lines. There are only two requirements. First, the period (P) of the fringe term (eq. [5.11]) should change smoothly across the ar-

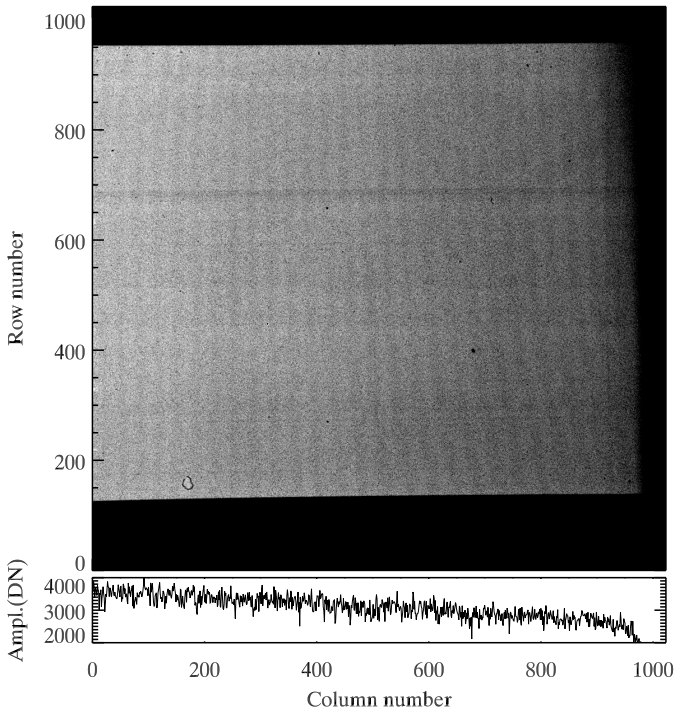

Figure 5.8: *Top*: Sample image with fringes. This flat field was obtained with the ISAAC instrument at the VLT. Each of the numeric parameters indicated in the captions from Figs. 5.8 to 5.14 were found to be the most appropriate for this particular example, but will need to change for different images. Columns 901–1024 and rows 0–149 and 951–1024 were vignetted and thus were cropped before analysis. Periodicity can be estimated by eye at ~ 40 pixels in the center of the image. *Bottom*: Middle (512th) row.

ray; and second, only on a per-row basis, the period must be at least several pixels, but it must also have at least a few oscillations per row. To attain the second condition it is acceptable to rotate the image by 90°. There are no constraints on how the phase ξ can change across rows or the range over which P can vary. Hence, the algorithm can handle many patterns that do not look like plane waves, such as patterns resembling wood grain.

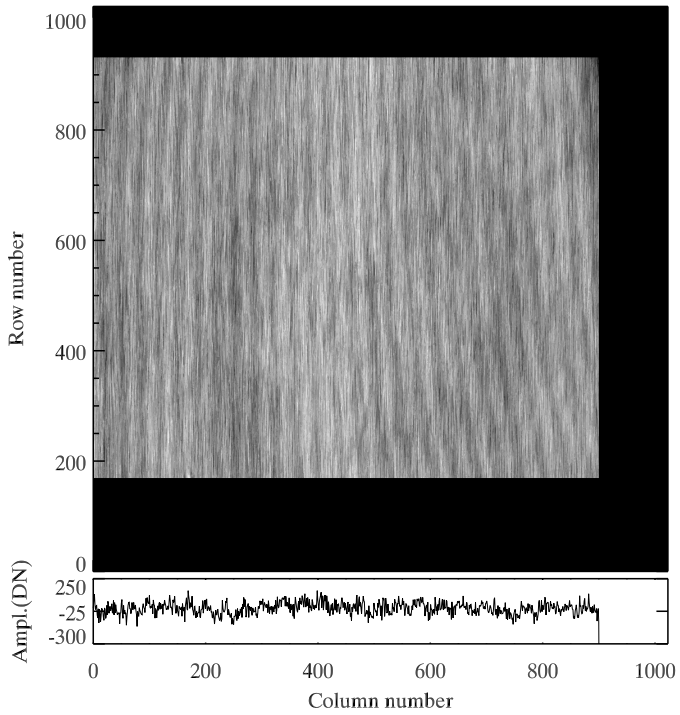

Figure 5.9: *Top*: Enhanced rows. Each pixel of the array in Fig. 5.8 is first replaced by the median average of the 41 closest pixels in the vertical direction. A polynomial fit to each row is then subtracted. The fringe pattern is enhanced and some bad pixels are removed. Note that the usable data area is reduced by 20 rows on the top and bottom because of the averaging. *Bottom*: Middle (512th) row.

Step 1: Enhanced Row and Wavelet Transform

For each image row we combine several surrounding rows to suppress random noise and remove bad pixels. To do this, we replace each pixel in the row with the median of a $1 \times n$ sub-image centered on the pixel and traversing n rows (the bin width). We then subtract a polynomial fit from the median-averaged row to obtain an "enhanced row" (Fig. 5.9). This subtraction significantly diminishes the large-period (low-frequency) oscillations of each row (and their corresponding wavelet amplitudes), allowing the next step to proceed more efficiently.

We then compute the wavelet transform of each enhanced row. The result

for each row is a two-dimensional, complex array, whose two dimensions are column number and period. There are several real and complex wavelet bases to choose from, but step 2 of this algorithm requires a complex basis because real bases are not able to separate phase from amplitude information. For this particular example, we used the Morlet wavelet because its functional form is the familiar quantum-mechanical wave packet

$$\Psi(t) = \pi^{-1/4} e^{-t^2/2 - i\omega_0 t}, \tag{5.16}$$

which makes it well suited for smoothly varying periods. Here, t and ω_0 are non-dimensional. For the Morlet basis, ω_0 is the only parameter; it dictates the minimum number of oscillations per row. The Morlet basis also has the advantage of being compact in the frequency domain.

In addition, the accompanying code allows the user to choose from several other popular wavelets as they could be better suited for particular data. Steps 2 and 3 are computed over the complex array amplitudes (the wavelet array). The phases of the complex array must be stored for use in step 4.

Step 2: Parametric Fit of Fringe Transform

At the period of the fringe pattern, the wavelet array will contain a prominent "fringe transform" pattern traversing the columns. Its amplitude depends on the amplitude of the fringe pattern (Fig. 5.10). This algorithm's success rests on our ability to distinguish this feature from the background noise level of the wavelet array. The fringe transform may vanish for particular columns, but it should be clearly distinguishable in most of each wavelet's array. Improved sampling in period can be obtained by interpolation or by decreasing the spacing between discrete scales in the wavelet transform. A compromise should

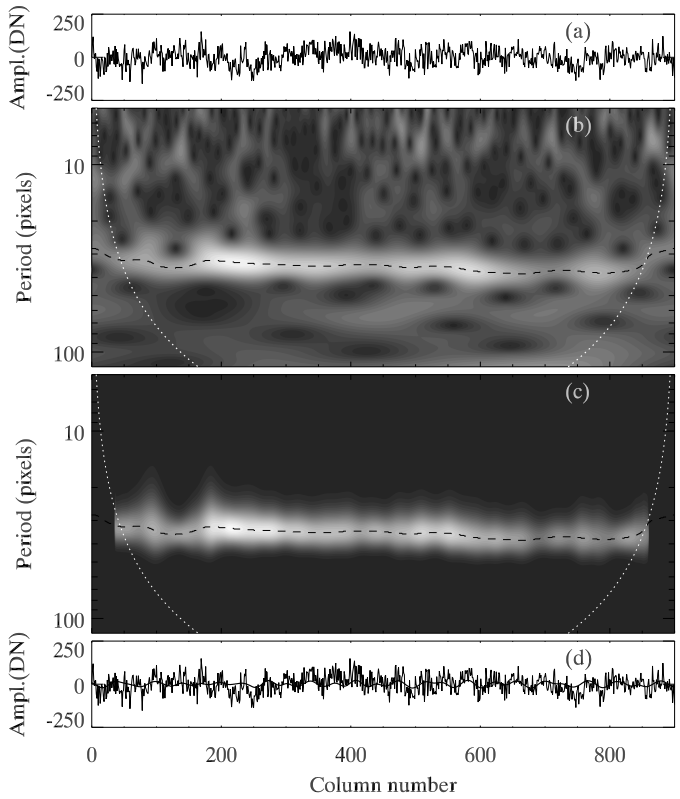

Figure 5.10: Wavelet transform of an enhanced row. In the center plots, the dotted line marks the COI; wavelet values below this boundary should not be trusted. The dashed line shows the fitted trace. (*a*) Middle enhanced row of Fig. 5.9. (*b*) Amplitude of the Morlet wavelet transform of (*a*). The wavelet is interpolated in period by a spline from the period sampling of the transform, and the fringe transform, a coherent pattern corresponding to a fringe with a period of 35 pixels, is clearly visible. (*c*) Reconstructed fringe transform using a Gaussian fit (cf. Fig. 5.11). (*d*) Fringe pattern after applying an inverse wavelet transform to (*c*), plotted over the input data.

be chosen; the latter approach is more accurate but demands more computer resources.

We next either extract or fit the fringe transform's amplitude versus period for a given column (Fig. 5.11). Starting from a reference column, the fringe profile is isolated by finding the first local minima on both sides of the reference period. Then one method is chosen to represent the profile within the minima: either we use the actual data within the minima (the "trueshape" method) or

a parametric function can be fitted to the profile. Only the latter approach will allow execution of the optional step 3. The value of the profile must be zero outside the fringe transform. Inside, on the other hand, it is recommended that the fringe transform profile exclude a background level (attributable to non-fringe image components, see discussion in §5.4.2). The highest point in the profile is used as the new reference period for the next column. The procedure is repeated for the whole fringe transform, extending in both directions from the reference column to the cone of influence (COI) boundary, beyond which the wavelet values are significantly contaminated by edge effects.

To fit the profile we have experimented with plain Gaussian fits with variable center (Gaussian with Variable Center, "GVC") and Gaussian functions in which the center is fixed at the maximum height (Gaussian with Fixed Center, "GFC"). Both Gaussian alternatives were considered without a constant background parameter (*noback*), and with this parameter. In the latter case, the background value can be kept or not when reconstructing ("keep" and "nokeep" respectively). In total, we have implemented six parametric fitting methods (that can be smoothed or not in step 3) and two trueshape fits (nokeep and keep), for a total of 14 fitting methods. The Gaussian shape was chosen not only because it is a natural choice to fit a peak, but also because it is the frequency-domain representation of the Morlet wavelet. The relative fringe-removal efficiency of these fits and of trueshape is discussed in §5.4.4.

Step 3: Optional Parameter Smoothing

If a functional parametric fit was used in the previous step, one can reduce the effects of noise by forcing the reconstructed fringe's parameters to vary

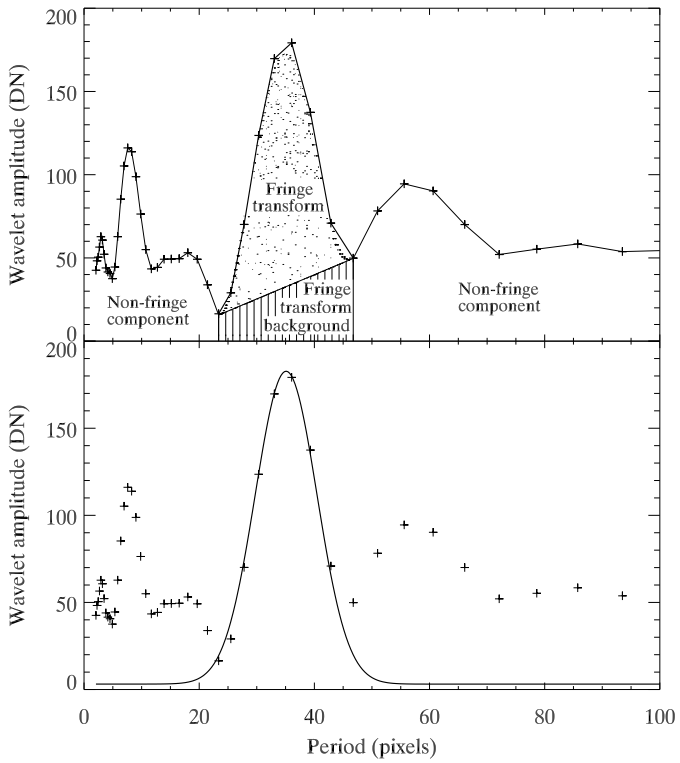

Figure 5.11: Cross–section along a column of the wavelet array. *Top*: Components diagram. Crosses are the amplitude of the wavelet points. The data points surrounding the region labeled as "fringe transform" are exactly what the true-shape method would reconstruct or what the parametric functions will fit. The region labeled "fringe transform background" is attributable to non-fringe components; in some of the tests it was used for the wavelet reconstruction (keep) and in some it was not (nokeep). *Bottom*: Gaussian fit (with background) to the region between the minima. Crosses are as above, and the solid line is the fitted profile.

smoothly. After repeating steps 1 and 2 for every row, a 2D array is obtained for each of the fitted parameters. First, we "patch" each of the parameter arrays by finding outliers beyond a given number of standard deviations from the neighborhood median and replacing them by that median value. Then, we smooth the array with a boxcar filter. Figure 5.12 shows an example.

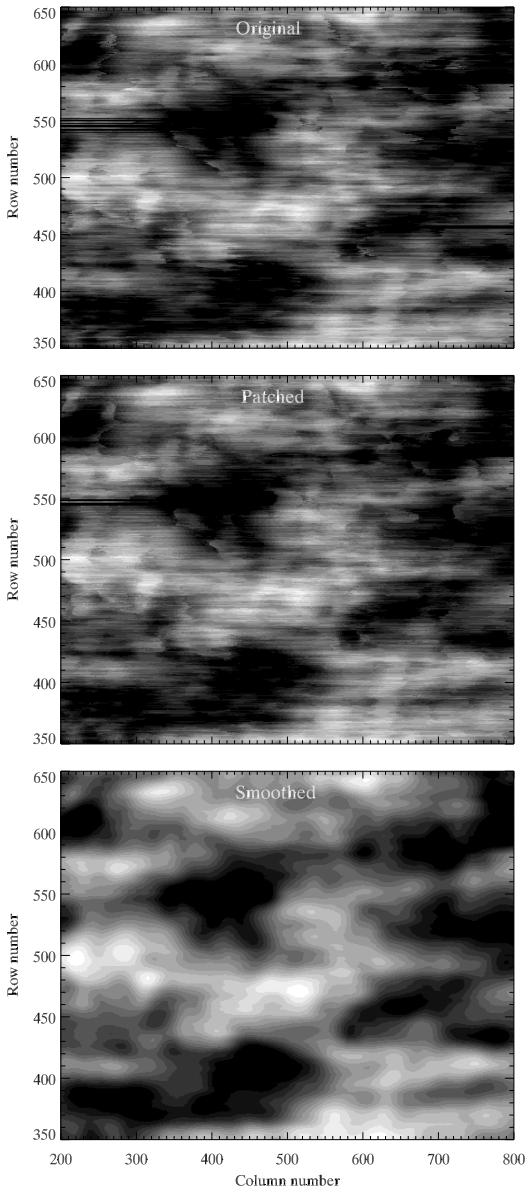

Figure 5.12: Gaussian height parameter smoothing. *Top*: Gaussian fit height parameter for central portion of example image. *Middle*: Parameter after replacing all values more than $\pm 1.5\,\sigma$ from the local median level with that level (patched array). *Bottom*: Patched array after smoothing with a 19 pixel boxcar filter. This procedure is repeated for each of the other Gaussian fit parameters.

Step 4: Reconstruction of the Fringe Pattern

We next evaluate the parameters to obtain the fringe's wavelet amplitudes (Fig. 5.10). Far from the reconstructed fringe transform the amplitude must be zero because any non-zero value there will cause unwanted noise in the reconstructed fringe. In particular, if a keep method is chosen, the reconstructed amplitude is set to zero outside the local minima. Finally, we apply an inverse wavelet transform to the reconstructed wavelet amplitude and the corresponding complex phases (see step 1).

We repeat these steps for every row to obtain the image's isolated-fringe pattern (Fig. 5.13). Due to the optional smoothing, the method to obtain the enhanced rows, and the COI boundary, the recovered-fringe pattern will have smaller borders than the original image. The fringe pattern can now be subtracted from the original image (Fig. 5.14). Figure 5.15 shows another example of this algorithm for a flat field from NIRSPEC at Keck.

5.4.4 Performance Tests

The ratio of fringe-pattern amplitude to the pixel-to-pixel variation (or noise) level varies among different instruments. We tested the algorithm's performance at different noise levels by using a synthetic image consisting of a fringe pattern, a background intensity, and random noise with a Gaussian distribution that mimics pixel-to-pixel flat-field variations and photon noise.

The fringe pattern was created using an analytic function that mimics the oscillating pattern in our example image. Its functional form is

$$F(x,y) = A\sin(\nu(x,y)x + \phi(y)), \tag{5.17}$$

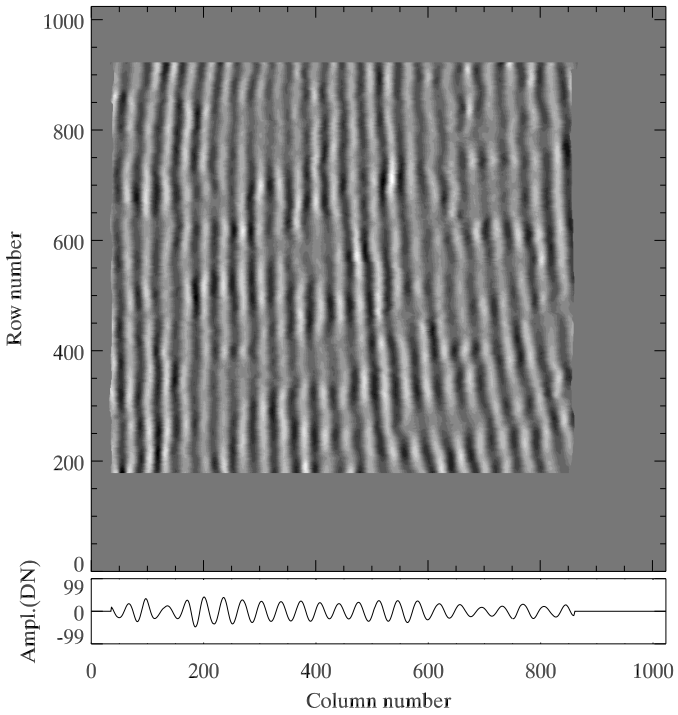

Figure 5.13: *Top*: Reconstructed fringe pattern (cf. Fig. 5.10, *bottom*). *Bottom*: Middle (512th) row.

where x and y are the position indices in the array, $\phi(\ldots)$ and $\nu(\ldots)$ are linear functions fit to the phase and frequency, respectively, of our example's fringe pattern, and A is the amplitude. For these tests we keep the amplitude constant, but there is no reason for A to be constant in a real image, nor is there any reason for a non-constant amplitude to adversely affect our algorithm. The background level is a double-linear function in both the x- and y-directions and has an edge taper.

We define noise strength as the standard deviation of the Gaussian noise divided by the standard deviation of the noiseless fringe pattern ($2^{-1/2}A$, due to its sinusoidal nature). Figure 5.16 shows the fraction of remnant fringe after running the algorithm on simulated data with different fitting functions and varying noise strength. The remnant fringe level is not strongly dependent on noise

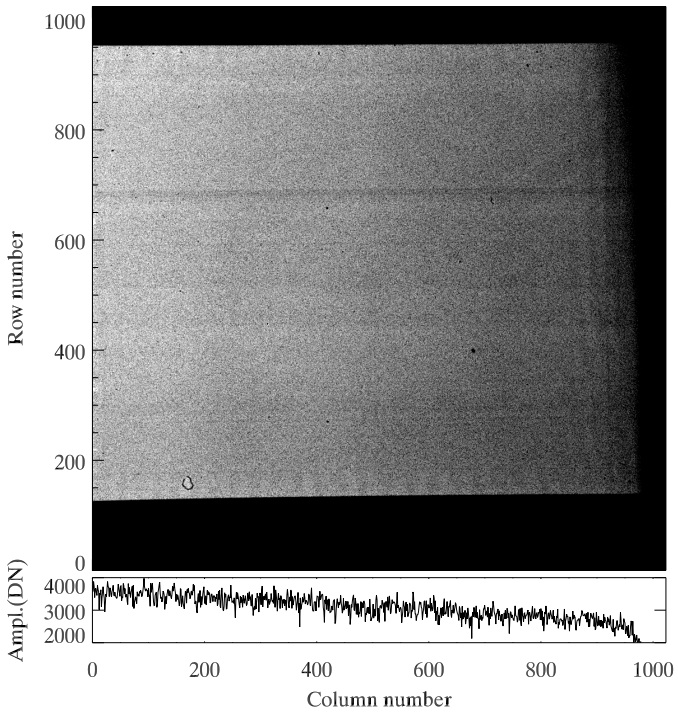

Figure 5.14: *Top*: Cleaned image: flat field of Fig. 5.8 minus the fringe pattern of Fig. 5.13. Note that some of the edges remain uncorrected (see text). *Bottom*: Middle (512th) row.

strength and all methods show very similar behavior with slight numerical differences when the noise strength is below ≈ 8. However, GFC consistently gives the best results in all cases, even improving when smoothing at high noise levels. Most of the methods remove over 95% of the fringe at noise strength of ≈ 0.5 and over 55% at a noise strength of ≈ 9 (equivalent to Fig. 5.8's noise strength). The plot in Figure 5.16 (bottom) confirms the intuitive result that the method yields better absolute results for smaller initial fringe amplitudes.

Figure 5.17 shows the effect of varying the bin width. If the width is too small when computing the enhanced row, the noise is insufficiently suppressed. For low noise, a bin width that is too large will begin to average out the fringe.

The algorithm is limited by the degree to which the analytic profile fitting

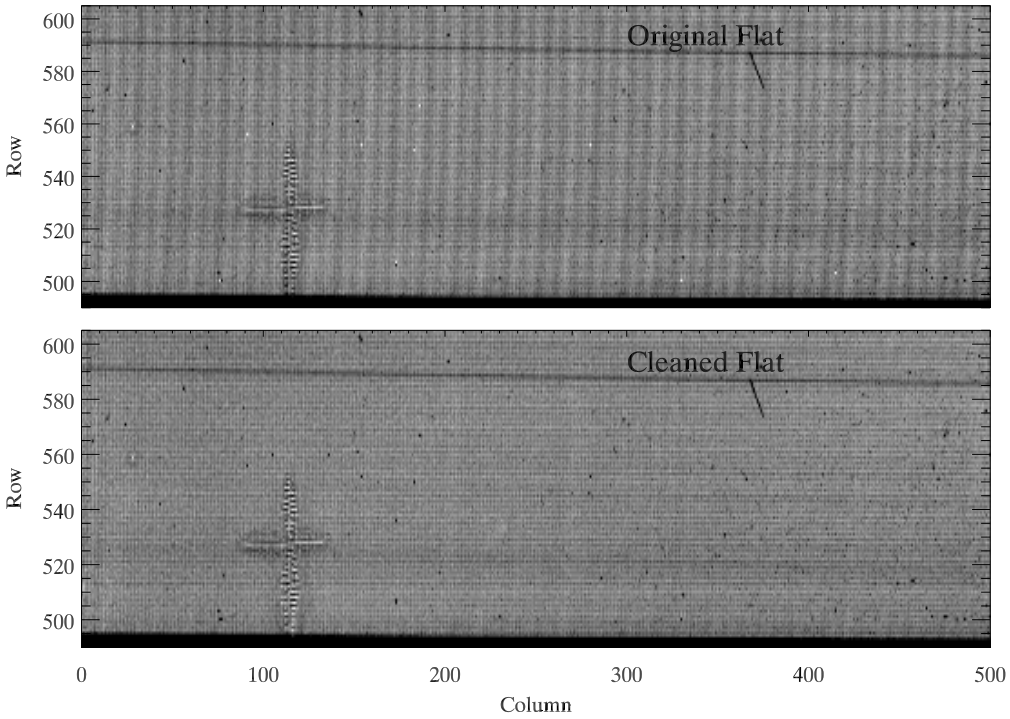

Figure 5.15: Example of fringe removal from a second instrument. The frames present a portion of a debiased flat-field frame from one order of the high-resolution NIRSPEC spectrograph at the Keck II telescope. *Top*: Original flat field. *Bottom*: Same flat field defringed by our method. The algorithm had to be applied twice; once for a fringe of period $\sim$ 20 pixels and then for a fringe of period $\sim$ 40 pixels.

function mimics the data. Figure 5.18 shows an example of a difficult profile, which gives very different fits when using the different fitting functions. Another source of error is the potential for the algorithm to miss the correct trace in the presence of high noise in the wavelet array (Fig. 5.19). Also, the reconstructed fringe pattern is smaller than the input data due to the factors listed in step 4. For the example of Figure 5.8, this area is $\approx$ 85% of the cropped input image, or over 90% if only considering the pixels lost for each surviving row, on average.

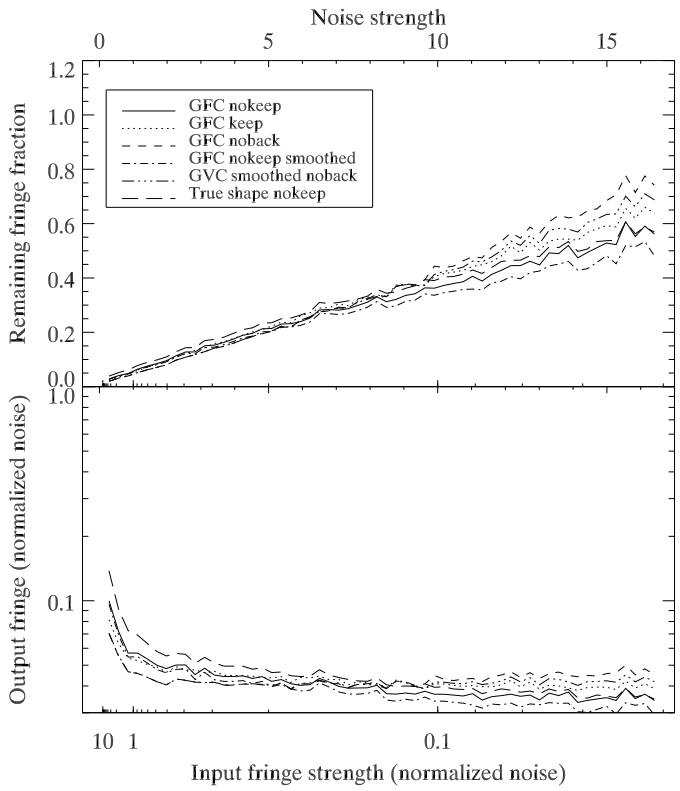

Figure 5.16: Remaining fringe for varying noise strengths. Only 6 of the 14 methods are shown above, for clarity. Omitted methods are similar to plotted methods and fall within the range of traces shown. The two nokeep methods give the best results. In general, all methods give similar results for low noise strength, but smoothed nokeep methods are better for high noise strength. *Top*: Fraction of fringe remaining. *Bottom*: Absolute fringe remaining when noise level is scaled to 1.

5.4.5 Discussion and Conclusions

Seeking a signal from a faint source that is spatially indistinguishable from a bright source is a long-standing observational challenge. Systematic errors that would have been unimportant when analyzing only the bright source are of concern when considering the fainter source. Hence, those errors must be reduced either in the instrument design or in the data analysis. To that effect, we have developed a general algorithm to remove fringe patterns from imag-

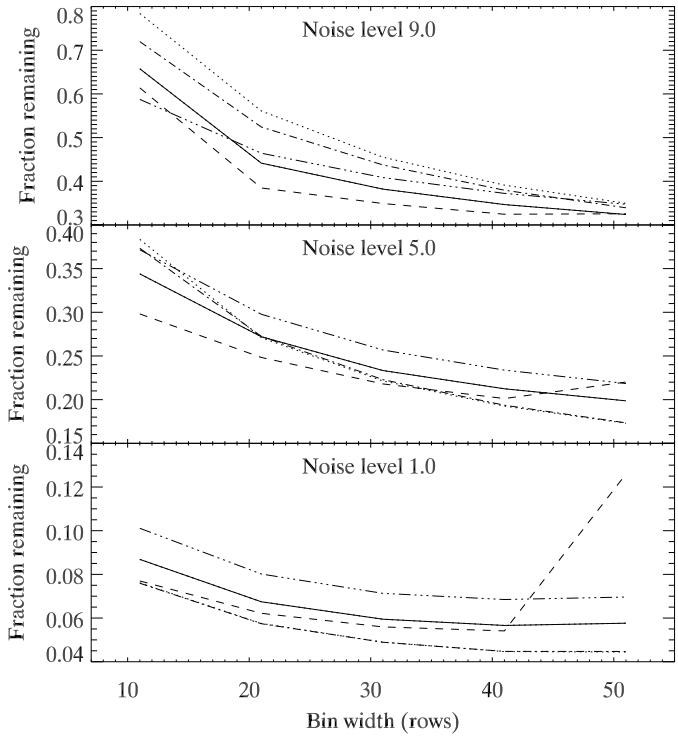

Figure 5.17: Remaining fringe for different enhanced-row bin widths. The panels show the same synthetic fringe pattern as Fig. 5.16 at three selected noise levels. Line styles are the same as in Fig. 5.16.

ing data such as flat-field frames while preserving other patterns. Cleaning flat fields is especially useful when the fringe pattern varies between them and the object data.

Consider the particular example of trying to detect the spectral modulation of an extrasolar planet as it transits its star using an instrument like ISAAC at the VLT. The equivalent noise strength for a flat field of this instrument is ≈ 9. On the other hand, no fringe was detected on the object frames up to a level equivalent to a noise strength of ≈ 1.5. Hence, according to Figure 5.16, removing the fringe in the flat fields through our method would reduce the systematic noise in the data frame by at least 40%. Considering the flat-field intensity, this translates into residual noise in the data frame $\approx$ 0.25% of the intensity of the

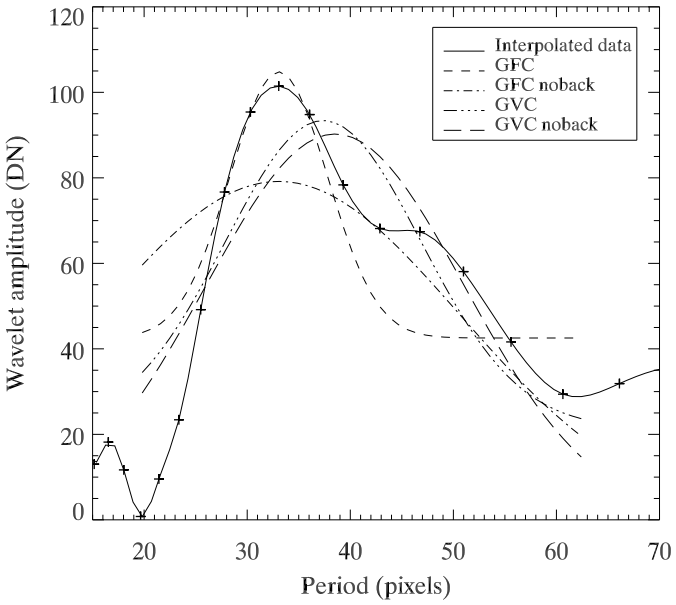

Figure 5.18: Different fitting methods applied to a profile with a complicated shape. Such shapes are due to noise and are the main limiting factor for this algorithm. This profile comes from the fringe transform for row 798, column 627 of our example array. Crosses show the data points, while the solid line is the interpolated profile. Other lines are explained in the key. The profiles are only fitted within the local minima at both sides of the reference period.

star. A typical molecular spectral variation is still below that level, of order 10^{-4} times the stellar intensity. However, it will now be easier to use the constancy of the planetary signal over many frames to attain the required sensitivity.

There are three main limitations of this algorithm when applied to a flat field. First, the shape of a fringe in wavelet space may be much more complicated than any reasonable fitting function, resulting in a partially corrected fringe. Second, to be able to follow the trace, the change in the fringe's period must be smooth. Finally, there is a region along the borders where the fringe pattern cannot be recovered.

The algorithm could be improved by finding a parameter-space interpolation mechanism that would allow defringing of object frames. Also, a method

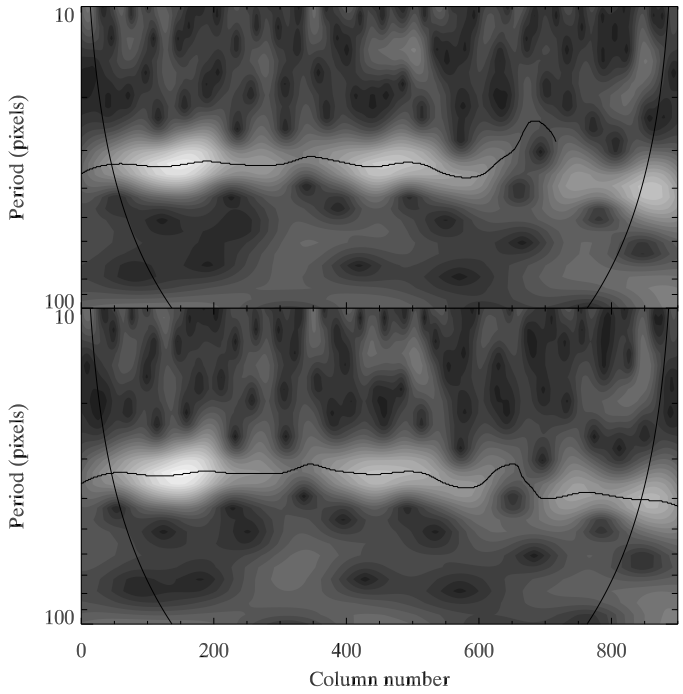

Figure 5.19: Example of missed trace. *Top*: Wavelet array from row 798 of Fig. 5.9. Around column 650 the trace goes in the wrong direction, towards a short period, and disappears around column 720. *Bottom*: Wavelet array from row 799 of Fig. 5.9. The array is similar to the top plot, but now the trace is correct through the last column. Patching in step 3 is likely to correct cases like this.

could be found to fit the entire fringe transform pattern simultaneously in the 3D wavelet space of row, column, and period. The 2D wavelet transform may be more appropriate for this approach.

Our IDL implementation of this algorithm and its documentation appear as an electronic supplement to this article. Updated versions are available on our Web sites or by e-mail request.

This material is based on work supported by the National Aeronautics and Space Administration under grant NAG5-13154 issued through the Science Mission Directorate. The example flat field was obtained from public archives of the

European Southern Observatory. Data presented herein were obtained at the W. M. Keck Observatory from telescope time allocated to the National Aeronautics and Space Administration through the agency's scientific partnership with the California Institute of Technology and the University of California. The Observatory was made possible by the generous financial support of the W.M. Keck Foundation. We also wish to thank the referee for insightful comments on the manuscript.

Facilities: VLT:Antu (ISAAC), Keck:II (NIRSPEC)

Conclusions and Future Work

6

The current work describes an attempt to detect water in the atmosphere of HD 209458b through transit spectroscopy. The data reduction processes, the development of a theoretical model for the modulation, and how we compared the model with the data using correlation were described in detail. Several new techniques and procedures (including the new method to correct fringes, Rojo and Harrington, 2006) were developed during this work and have been explained in detail. The computer routines are available under the GNU General Public License (GNU-GPL) at the DSpace* Internet archive or upon request from the author**.

Mainly due to the unfortunate choice of observing parameters and the incidental telluric conditions, it is concluded that the data analysis is not sensitive to the presence of water in the atmosphere of HD 209458b. This was confirmed by the analysis of a synthetic dataset that included the signal from a theoretical model. However, by scaling the results, limits were placed on planetary system configurations that could have yielded a successful detection of atmospheric water from our observing parameters and telluric conditions. It is found that none of the 10 known transiting planets would have been detectable.

*http://dspace.library.cornell.edu/handle/1813/3209

**My permanent website: http://www.das.uchile.cl/∼ pato/sw/

In addition, there is a discussion of the many improvements that can be considered for future observations of this kind. These include: airmass and timing constraints, the simultaneous observation of a calibrator star, and a new method to find the optimal wavelength range. All the experience gained in this project will be applied to conduct and analyze new observations of transiting planets. New observations of HD 209458b and HD 189733b are being planned with a more appropriate wavelength range and resolution, and using more stringent airmass constraints for the observations.

Physical Constants | A

Quantity	Symbol	Value	Units
Planck	h	6.626068×10^{-27}	erg s
Maxwell-Boltzmann	k_B	1.380658×10^{-16}	erg K^{-1}
Gravitational constant	G	6.67259×10^{-8}	cm^3 g^{-1} s^{-2}
Loschmidt number	n_L	2.6868×10^{19}	cm^{-3}
Gas constant	R	8.3145×10^{7}	erg K^{-1} mol^{-1}
Electronic charge	e	$4.8032068 \times 10^{-10}$	esu
H_2O molec. diam.	r_{H_2O}	3.2×10^{-10}	cm
atomic mass unit	m_u	$1.6605402 \times 10^{-24}$	g
Astronomical Unit	AU	1.49598×10^{13}	cm
Parsec	pc	$3.08568025 \times 10^{18}$	cm
Solar radius	$R_\odot$	6.95508×10^{10}	cm
Jupiter radius	R_J	6.9911×10^{9}	cm
Earth radius	$R_\oplus$	6.378×10^{8}	cm
Solar mass	$M_\odot$	1.989×10^{33}	g
Jupiter mass	M_J	1.898×10^{30}	g
Earth mass	$M_\oplus$	5.97×10^{27}	g

Some Well-Known Physics | B

This appendix will briefly summarize some well established physical knowledge that was referenced in this work.

This appendix is prepared because in the literature, the same names have been given to quantities that have been defined in several different ways.

B.1 Energy Related Quantities

Light traveling through space can be quantified in terms of its energy per unit time. In particular, for spectroscopy we need to use energy per unit time per unit wavelength ($\mathrm{d}E_\lambda / \mathrm{d}t$), or equivalently, per unit time per unit frequency ($\mathrm{d}E_\nu / \mathrm{d}t$).

The quantities most commonly used are specific intensity and flux. The former is defined as the amount of energy that traverses a unit area per unit time, per unit wavelength, in a given direction (per unit solid angle). If this area is not oriented normal to the direction of the incoming energy (say, at an angle θ), then there is a geometric factor $\cos\theta\,\mathrm{d}A$ to the amount of energy that traverses this area $\mathrm{d}A$. Hence, we can write

$$\mathrm{d}E_\lambda = I_\lambda \cos\theta\,\mathrm{d}A\,\mathrm{d}t\,\mathrm{d}\Omega, \tag{B.1}$$

where I_λ is defined as the specific intensity and $\mathrm{d}\Omega$ is the differential solid an-

gle.

Flux is similar to intensity, but it is defined as the energy per unit time that traverses a unit area (independently of direction). Hence, we can obtain it by integrating intensity over solid angle (note that the $\cos\theta$ orientation factor must be present)

$$\begin{aligned} \mathrm{d}f_\lambda &= I_\lambda \cos\theta \, \mathrm{d}\Omega \\ &= I_\lambda \cos\theta \sin\theta \, \mathrm{d}\theta \, \mathrm{d}\phi. \end{aligned} \tag{B.2}$$

The following expressions for flux will be derived for an arbitrary spherical celestial body (star or planet) that is projected onto a disk. If the object is at a distance d from the Earth and R indicates the distance to the center of the disk, we obtain

$$\begin{aligned} f_\lambda &= \int_0^{2\pi} \int_0^{\pi} \underbrace{I_\lambda}_{I_{0\lambda} B_\lambda(R)} \underbrace{\sin\theta}_{\frac{R}{d}} \underbrace{\cos\theta \, \mathrm{d}\theta}_{\frac{\mathrm{d}R}{d}} \, \mathrm{d}\phi \\ &= I_{0\lambda} \frac{2\pi}{d^2} \int_0^{R_M} B_\lambda(R) R \, \mathrm{d}R, \end{aligned} \tag{B.3}$$

where R_M is the radius of the disk, $B_\lambda(R)$ is the limb-darkening law, and $I_{0\lambda}$ is the intensity at the center if the disk. The last two quantities are used in this work with or without explicitly indicating the λ subscript. In the above expression we have used the approximation that

$$\sin\theta \approx \tan\theta = \frac{R}{d}, \tag{B.4}$$

since the object is far away from us.

To consider a limb-darkening law is only the first-order approximation to the non-homogeneity of the projected surface of a celestial body. A more detailed treatment would include sunspots, hot spots, and clouds, among others. However, they have no simple analytical expressions.

Limb darkening can be understood as follows: due to the spherical geometry of the star, a ray closer to the limb of the disk would have to emerge from a shallower depth than a ray closer to the center of the disk if they were to traverse the same amount of material. Consequently, a ray coming from the limb is produced in less deep layers of the atmosphere; less deep also means colder; therefore, it is less intense (and redder). Thus, limb darkening only depends on the projected radius, R, of the disk.

B.2 Maxwell-Boltzman Distribution

Acoording to classical physics, an atomic system in equilibrium obeys the Boltzmann distribution (also called the Maxwell-Boltzmann distribution), which relates the equilibrium number density between two energy levels, and is given by

$$\frac{\bar{n}_u}{\bar{n}_l} = \frac{g_u}{g_l} \exp\left(-\frac{\Delta E_{ul}}{k_B T}\right), \tag{B.5}$$

where g_i and $\bar{n}_i$ are the degeneracy and the equilibrium population number of level i, and ΔE_{ul} is the energy difference between the upper, u, and lower, l, energy levels. In the case of electronic levels of an atom, $\Delta E = h\nu$.

If one wants to compare the number density of a particular energy level, l, with the total number density, N, one can use Eq. (B.5) to obtain

$$\begin{aligned}
\frac{\bar{n}_l}{N} &= \frac{\bar{n}_l}{\sum_i \bar{n}_i} = \frac{1}{\sum_i \frac{\bar{n}_i}{\bar{n}_l}} \\
&= \frac{1}{\sum_i \frac{g_i}{g_l} \exp\left(-\frac{\Delta E_{il}}{k_B T}\right)} \\
&= \frac{g_l}{Z} \exp\left(-\frac{E_l}{k_B T}\right),
\end{aligned} \tag{B.6}$$

where Z is the partition function given by

$$Z = \sum_i g_i \exp\left(-\frac{E_i}{k_B T}\right). \tag{B.7}$$

The Maxwell-Boltzmann distribution also predicts a velocity distribution of particles: the number of particles with velocity components between $[v_x, v_x + \mathrm{d}x]$, $[v_y, v_y + \mathrm{d}y]$ and $[v_r, v_r + \mathrm{d}r]$ (r coordinate is along the line of sight, while x and y define a plane perpendicular to it) is given by

$$f(\vec{v})\,\mathrm{d}v_x\,\mathrm{d}v_y\,\mathrm{d}v_r = \bar{N}\left(\frac{m}{2\pi k_B T}\right)^{\frac{3}{2}} \exp\left(-\frac{m(v_x^2+v_y^2+v_r^2)}{2k_B T}\right)\mathrm{d}v_x\,\mathrm{d}v_y\,\mathrm{d}v_r, \tag{B.8}$$

where k_B is the Boltzmann constant and $\bar{N}$, m, v, and T are the number, mass, velocity, and temperature of the particles, respectively. The velocity distribution along any single coordinate is obtained by integrating the other two. For example, the normalized velocity distribution along the line-of-sight direction (r) is given by

$$\begin{aligned} f(v_r)\,\mathrm{d}v_r =& \frac{1}{\bar{N}}\int_{v_z}\int_{v_y} f(\vec{v})\,\mathrm{d}v_x\,\mathrm{d}v_y\,\mathrm{d}v_r \\ =& \left(\frac{m}{2\pi k_B T}\right)^{\frac{1}{2}} \exp\left(-\frac{mv_r^2}{2k_B T}\right)\mathrm{d}v_r. \end{aligned} \tag{B.9}$$

The mean velocity can be obtained by changing to spherical coordinates ($\mathrm{d}v_x\,\mathrm{d}v_y\,\mathrm{d}v_r = \sin\phi\, v^2\,\mathrm{d}\phi\,\mathrm{d}\theta\,\mathrm{d}v$), and weighting the velocity modulus with the distribution, obtaining

$$\begin{aligned} <v> =& \iiint v f(\vec{v})\,\mathrm{d}v_x\,\mathrm{d}v_y\,\mathrm{d}v_r \\ =& 4\pi\left(\frac{m}{2\pi k_B T}\right)^{\frac{1}{2}}\int_0^\infty \exp\left(-\frac{mv^2}{2k_B T}\right) v^3\,\mathrm{d}v \\ =& \sqrt{\frac{8k_B T}{\pi m}}. \end{aligned} \tag{B.10}$$

One can extend this result to find the relative velocity of molecules with masses m_1 and m_2, respectively. Assuming that both species independently follow a Maxwell-Boltzmann velocity distribution, one finds that the square of the relative velocity of the average velocities is given by

$$\begin{aligned} ||v_{12}||^2 &= ||< v_1 > \hat{v}_1 - < v_2 > \hat{v}_2||^2 \\ &= ||< v_1 > \hat{z} - < v_2 > (\hat{x}\sin\theta\cos\phi + \hat{y}\sin\theta\sin\phi + \hat{z}\cos\theta)||^2 \\ &= \frac{8k_B T}{\pi}\left(\frac{\sin^2\theta}{m_2} + \left(\frac{1}{\sqrt{m_1}} + \frac{\cos\theta}{\sqrt{m_2}}\right)^2\right). \end{aligned} \tag{B.11}$$

where $\hat{v}_1$ is aligned with the z-axis.

Averaging over the relative direction of the averages, θ, we obtain

$$< ||v_{12}||^2 > = \frac{8k_B T}{\pi}\left(\frac{1}{m_1} + \frac{1}{m_2}\right), \tag{B.12}$$

One can thus say that the average relative velocity between any species 1 and 2 is given by

$$\sqrt{< ||v_{12}||^2 >} = \sqrt{\frac{8k_B T}{\pi}\left(\frac{1}{m_1} + \frac{1}{m_2}\right)}. \tag{B.13}$$

B.3 Einstein's Coefficients

The probability of electronic transitions in atoms is dictated by their quantum-mechanical properties. The Einstein coefficients are an elegant way to refer to those probabilities.

The definitions of the Einstein coefficients used in this section are akin, but not identical, to what Rybicki and Lightman (1979) used. Note, for example, that the definitions differ considerably from those used by Goody and Yung (1989).

Without loss of generality, in the following discussion we will consider two electronic levels at two different energy levels. The level with greater energy will be referred to as the upper level, u, and the other as the lower level, l.

There are three possible kinds of transitions, each one of them involving the emission or absorption of a photon with frequency

$$\nu_0 = \frac{1}{h}\left(E_u - E_l\right) \tag{B.14}$$

with respect to the rest frame of the atom itself, where h is Planck's constant. Differing (for clarity) from the approach of both Goody and Yung, and Rybicki and Lightman, the following discussion addresses a single, static atom. Not worrying about effects like the Doppler shift of the radiation field allows us to work with monochromatic radiation.

The three kinds of transitions and Einstein Coefficients are

- *Spontaneous emission*: An electron can spontaneously go from an upper to a lower level. If $\mathrm{d}\Omega$ is a unit solid angle, then it will undergo this transition emitting a photon in a certain direction with a probability per unit of time given by

$$\Gamma_{spon-abs} = A_{ul}\,\mathrm{d}\Omega \quad \left[\sec^{-1}\right]. \tag{B.15}$$

- *Induced emission*: An electron can decay from an upper to a lower energy level after resonance with an incoming electromagnetic wave at the appropriate frequency. The probability of this per unit time is given by

$$\Gamma_{ind-abs} = B_{ul} I_\nu\,\mathrm{d}\Omega \quad \left[\sec^{-1}\right], \tag{B.16}$$

  where I_ν is the incoming radiation's intensity.

- *Induced absorption*: An electron can be excited from a lower to an upper level by absorbing a photon of the right frequency. The probability of this happening per unit of time is given by

$$\Gamma_{ind-em} = B_{lu} I_\nu \, \mathrm{d}\Omega \quad \left[\sec^{-1}\right] \tag{B.17}$$

In local thermodynamic equilibrium (LTE) conditions, we need the number of transitions out of a state to equal the number of transitions into that same state. Hence, considering only two states*, we have

$$\bar{n}_l B_{lu} \bar{I}_\nu \, \mathrm{d}\Omega = \bar{n}_u B_{ul} \bar{I}_\nu \, \mathrm{d}\Omega + \bar{n}_u A_{ul} \, \mathrm{d}\Omega, \tag{B.18}$$

where all the barred quantities refer to LTE amounts. Solving for I_ν yields

$$\begin{aligned} \bar{I}_\nu &= \frac{\bar{n}_u A_{ul}}{\bar{n}_l B_{lu} - \bar{n}_u B_{ul}} \\ \bar{I}_\nu &= \frac{\frac{A_{ul}}{B_{ul}}}{\frac{\bar{n}_l}{\bar{n}_u}\frac{B_{lu}}{B_{ul}} - 1}. \end{aligned} \tag{B.19}$$

Using Eq. (B.5), we obtain

$$\bar{I}_\nu = \frac{\frac{A_{ul}}{B_{ul}}}{\frac{g_l}{g_u}\frac{B_{lu}}{B_{ul}} e^{-h\nu/k_B T} - 1}. \tag{B.20}$$

Finally, by requiring Eq. (B.21) to be equal to the fundamental blackbody intensity function in local thermodynamic equilibrium (the Planck function):

$$B_\nu = \frac{2h\nu^3/c^2}{e^{-h\nu/k_B T} - 1}. \tag{B.21}$$

*Eq. (B.18) should hold even when there are one or more intermediate states of transition. However, I have not found information in the literature addressing that problem.

we obtain:

$$g_u B_{ul} = g_l B_{lu} \tag{B.22}$$

$$A_{ul} = \frac{2hv^3}{c^2} B_{ul}, \tag{B.23}$$

where g_i is the degeneracy of the i-th electronic level and c is the speed of light.

Hence, it turns out that only one of the previous three Einstein Coefficients is truly independent.

Note that the previous relations do not depend on temperature, nor on any other environmental quantity. In fact, the Einstein coefficients are an inherent characteristic of the atoms independent of changing environments.

B.4 Applied Time Dependent Perturbation Theory in QM

Time-dependent perturbation theory in quantum mechanics (Sakurai, 1994, p. 325) predicts that the first order approximation of the transition probability from a state l to a state u in a length of time, t, is given by

$$\mathtt{w}_{l\to u} = \left| \frac{1}{\hbar} \int_0^t \left\langle l \left| e^{-iH_0 t/\hbar} V e^{-iH_0 t/\hbar} \right| u \right\rangle \, \mathrm{d}t \right|^2, \tag{B.24}$$

where V is the perturbation term and H_0 is the time-independent term of the Hamiltonian, H.

Eigenfunctions of H_0 are represented by the kets $\{|i>\}_i$. Hence,

$$e^{-iH_0 t/\hbar} |u\rangle = e^{-iE_u t/\hbar} |u\rangle \tag{B.25}$$

$$e^{-iH_0 t/\hbar} |l\rangle = e^{-iE_l t/\hbar} |l\rangle, \tag{B.26}$$

where E_u and E_l are the energies (eigenvalues) associated with the respective level (eigenfunction). Therefore

$$\mathtt{w}_{l\to u} = \left| \frac{1}{\hbar} \int_0^t V_{lu} e^{-i\omega_{lu} t} \, \mathrm{d}t \right|^2, \tag{B.27}$$

where $\omega = 2\pi\nu = \frac{1}{\hbar}\left(E_u - E_l\right)$.

The discussion below will only apply this theory to interactions with a radiation field. In that case

$$\begin{aligned} H &= \left[\left(c\mathbf{p} - e\mathbf{A}\right)^2 + m_e^2 c^4\right]^{1/2} + e\phi \\ &\approx \frac{\mathbf{p}^2}{2m_e} - \frac{e}{m_e c}\mathbf{A}\cdot\mathbf{p} + \frac{e^2|\mathbf{A}|^2}{2m_e c^2} + e\phi, \end{aligned} \tag{B.28}$$

where $\mathbf{p}$ is the quantum mechanical (QM) momentum operator, $\mathbf{A}$ and ϕ are the electric- and magnetic-potential operators, and e is the electron charge. The previous equations have also used the non-relativistic approximation (ignoring the constant mass) and made use of the Coulomb gauge ($\nabla\cdot\mathbf{A} = 0$).

The first and fourth terms in the previous Eq. (B.28) are independent of time, while the third term is much smaller than the second term for photon densities greater than* 10^{25} cm^{-3} (Rybicki and Lightman, 1979, p. 268). Therefore, the only time-dependent term to associate with potential energy, V, is

$$V = -\frac{e}{m_e c}\mathbf{A}\cdot\mathbf{p}. \tag{B.29}$$

One can assume that

$$\mathbf{A}\left(\mathbf{r}, t\right) = \mathbf{A}\, e^{i\frac{2\pi}{\lambda}\hat{\mathbf{n}}\cdot\mathbf{r}}, \tag{B.30}$$

where λ and $\hat{\mathbf{n}}$ are the radiation wavelength and its direction. Hence, one obtains

$$\begin{aligned} V_{lu} &= \langle l\,|V|\,u\rangle \\ &= -\frac{e\mathbf{A}(\mathbf{t})}{m_e c}\cdot\left\langle l\left|\, e^{i\frac{2\pi}{\lambda}\hat{\mathbf{n}}\cdot\mathbf{r}}\mathbf{p}\,\right|\, u\right\rangle. \end{aligned} \tag{B.31}$$

*Note that the photon density at the surface of a Sun-like star is 10^{12} cm^{-3}.

One can simplify even more. If one uses a dipole approximation of the exponential

$$e^{i\frac{2\pi}{\lambda}\hat{\mathbf{n}}\cdot\mathbf{r}} = 1 + i\frac{2\pi}{\lambda}\hat{\mathbf{n}}\cdot\mathbf{r} + \frac{1}{2}\left(i\frac{2\pi}{\lambda}\hat{\mathbf{n}}\cdot\mathbf{r}\right)^2 + \quad \ldots, \tag{B.32}$$

and keeps only the first term*; one can then have

$$\begin{aligned}
\left\langle l \left| e^{i\frac{2\pi}{\lambda}\hat{\mathbf{n}}\cdot\mathbf{r}}\mathbf{p} \right| u \right\rangle &\approx \langle l \left|\mathbf{p}\right| u\rangle \\
&= \frac{m_e}{i\hbar}\langle l \left|[\mathbf{r}, H_0]\right| u\rangle \\
&= \frac{m_e}{i\hbar}\langle l \left|\mathbf{r}H_0 - H_0\mathbf{r}\right| u\rangle \\
&= \frac{m_e}{i\hbar}\left(E_u - E_l\right)\langle l \left|\mathbf{r}\right| u\rangle \\
\langle l \left|\mathbf{p}\right| u\rangle &= \frac{m_e}{i\hbar e}\left(E_u - E_l\right)\mathbf{d}_{lu},
\end{aligned} \tag{B.33}$$

where $[,]$ is the conmutator operator (c.f. Eq 2.2.19 of Sakurai, 1994) and $\mathbf{d}_{lu} = e\langle l \left|\mathbf{r}\right| u\rangle$ is the electric dipole operator.

Using Eqs. (B.31) and (B.33) in Eq. (B.27) yields

$$\begin{aligned}
\mathtt{w}_{l\to u} &= \left| -\frac{E_u - E_l}{i\hbar^2 c}\mathbf{d}_{lu}\cdot\int_0^t \mathbf{A}(\mathbf{t})\, e^{-i\omega_{lu}t}\,\mathrm{d}t \right|^2 \\
&= \frac{4\pi^2\omega_{ul}^2\left|A(\omega_{ul})\right|^2}{\hbar^2 c^2}\left|\mathbf{d}_{lu}\cdot\hat{\epsilon}\right|^2,
\end{aligned} \tag{B.34}$$

where $\hat{\epsilon}$ is the orientation of the electric field such that $\mathbf{A} = A\hat{\epsilon}$ and

$$A(\omega_{lu}) = \frac{1}{2\pi}\int_0^t \mathbf{A}(\mathbf{t})\, e^{-i\omega_{lu}t}\,\mathrm{d}t \tag{B.35}$$

will also be a valid Fourier transformation if we assume that t is big enough to effectively cover the whole frequency range in consideration.

*Justified because $r\frac{1}{\lambda} \sim a_0\frac{\Delta E}{\hbar c} \sim Z\alpha/2 \ll 1$ for moderate values of atomic number Z, where $a_0 \sim 1$Å and $\alpha = e^2/\hbar c \approx 1/137$ is the fine-structure constant.

An average value of the dipole operator over all directions would be given by

$$\begin{aligned}\left\langle |\mathbf{d}_{lu}\cdot\hat{\epsilon}|^2 \right\rangle &= \frac{1}{4\pi}\int |\mathbf{d}_{lu}\cdot\hat{\epsilon}|^2 \,\mathrm{d}\Omega \\ &= |d|^2\,\frac{1}{2}\int_0^{\pi}\cos^2\theta\sin\theta\,\mathrm{d}\theta \\ &= \frac{1}{3}|d|^2. \end{aligned} \tag{B.36}$$

It is useful to express $A(\omega_{lu})$ in Eq. (B.34) in terms of the intensity (I_ν). For that, two results from classical electrodynamics (e.g., Jackson, 1999) are used:

$$\mathcal{E}_t = -\frac{1}{c}\frac{\partial A_t}{\partial t} \tag{B.37}$$

$$\frac{\mathrm{d}E}{\mathrm{d}\mathcal{A}\,\mathrm{d}t} = \frac{c}{4\pi}\mathcal{E}_t^2, \tag{B.38}$$

where subindex t refers to time dependency, E to energy, $\mathcal{A}$ to area, $\mathcal{E}$ to electric field, and A to the electromagnetic vector potential. The latter is the classical equivalent to the operator A used in the previous QM discussion.

Basic Fourier-transform properties allow one to write Eq. (B.37) as:

$$\mathcal{E}_\omega = -\frac{i\omega}{c}A_\omega, \tag{B.39}$$

where now the subindex ω indicates that the functions depend on angular frequency.

Meanwhile, integrating Eq. (B.38) over time yields

$$\frac{\mathrm{d}E}{\mathrm{d}\mathcal{A}} = \frac{c}{4\pi}\int_{-\infty}^{\infty}|\mathcal{E}_t|^2\,\mathrm{d}t. \tag{B.40}$$

Parseval's theorem for Fourier transforms says that

$$\int_{-\infty}^{\infty}\mathcal{E}_t^2\,\mathrm{d}t = 2\pi\int_{-\infty}^{\infty}|\mathcal{E}_\omega|^2\,\mathrm{d}\omega. \tag{B.41}$$

Furthermore, Eq. (B.40) integrates an even function over ω. Hence, one can add a factor of 2 and integrate from 0 to ∞, instead. This gives

$$\frac{\mathrm{d}E}{\mathrm{d}\mathcal{A}} = c \int_0^\infty |\mathcal{E}_\omega|^2 \, \mathrm{d}\omega$$

or

$$\frac{\mathrm{d}E}{\mathrm{d}\omega \, \mathrm{d}\mathcal{A}} = c|\mathcal{E}_\omega|^2. \tag{B.42}$$

Then, using this result with Eq. (B.39) and Eq. (B.1), which is the definition of I_ν (remembering that $\omega = 2\pi\nu$ and orienting the observing surface normal to the ray, $\theta = 90^\circ$), gives

$$\frac{1}{2\pi} I_\nu \, \mathrm{d}\Omega \Delta t = \frac{\omega^2}{c} |A_\omega|^2, \tag{B.43}$$

where Δt is any arbitrary amount of time if one assumes a constant intensity.

In particular, if Δt is the time t used in the QM derivation in the first part of this section, bringing together Eqs. (B.36) and (B.43) into Eq. (B.34) yields

$$\mathtt{w}_{l \to u} = \frac{2\pi}{3\hbar^2 c} \, |d_{lu}|^2 \, I_\nu \, \mathrm{d}\Omega \Delta t. \tag{B.44}$$

This quantity is 4π times smaller than the expression in Equation (10.27) of Rybicki and Lightman (1979). However, this difference arises because they work with solid-angle-averaged intensities, while this work uses ray intensities. The factor, 4π, disappears in Eq. (B.44) but reappears in Eq. (C.7); hence, in both works the resulting expression for the extinction coefficient (cf. Eq. C.12) is the same.

B.5 Uncertainty Relations

Despite the extensive use and renown they have, the Heisenberg uncertainty relations have, at times, been misused in the literature and defined with several

different constants.

The correct position-momentum uncertainty relation is

$$\Delta x \Delta p \geq \frac{1}{2}\hbar \tag{B.45}$$

where the Δ quantities are uncertainties in the value of position and momentum, and $\hbar$ is Planck's constant divided by 2π.

An analogous relation for energy-time uncertainties is

$$\Delta E \Delta t \geq \frac{1}{2}\hbar. \tag{B.46}$$

In the literature these two relations have been mistakenly used with h instead of $\hbar$, or without the $1/2$ factor.

B.6 Hydrostatic Equilibrium

The balance between the pressure and the gravity forces at each layer of a planet or star is known as hydrostatic equilibrium. If the upper and lower boundaries of a parcel floating in an atmosphere are identified as 1 and 2, respectively. Then, the difference in forces, F, due to the pressure, P, alone would be

$$|F_p| = A(P_2 - P_1) = A\,\delta P, \tag{B.47}$$

where A is the parcel's horizontal area. The weight of the parcel, on the other hand, is its mass times the force of gravity, g. If the distance between the layers is δz, then the force due to gravity is

$$|F_g| = \rho\, A\, \delta z\, g, \tag{B.48}$$

where ρ is the parcel's density.

The equilibrium is attained when all acting forces cancel each other. If one ignores the centripetal force due to the planet's rotation, the only two relevant forces introduced above act in opposite directions. Then, for an infinitesimally small distance, δz,

$$\frac{\mathrm{d}P}{\mathrm{d}z} = -\rho g. \tag{B.49}$$

Equation (B.49) is known as the hydrostatic equilibrium equation.

Equation B.49 can be solved for an ideal gas in the outer atmosphere of a Jupiter-sized planet, where the gravity remains constant. The equation of state in such case is given by

$$P = \rho k_B T \frac{1}{\bar{\mu}}, \tag{B.50}$$

where $\bar{\mu}$ is the average molecular weight and T is the temperature. Hence, one can rewrite the hydrostatic equilibrium equation as

$$\frac{\mathrm{d}P}{P} = -\frac{\bar{\mu} g}{k_B T}\mathrm{d}z \tag{B.51}$$

and solve for pressure integrating from the reference layer ($z = 0$, $P = P_0$):

$$P(z) = P_0 e^{-z/H}, \tag{B.52}$$

where $H = \frac{k_B T}{\bar{\mu} g}$ is known as the *scale height*, a quantity that indicates how extended an atmosphere is.

Line Profile | C

A spectral line has a definite strength and a finite width. Both qualities depend on several enviromental factors, which are discussed in this Appendix.

The discussion in this chapter will use the semi-classical formulation of radiation theory. The atom will be treated quantum-mechanically but will interact with a classical radiation field.

C.1 Radiation Basics

Photons interact with atoms in four ways: spontaneous emission, induced emission, induced absorption (induced extinction), and scattering. The latter will be dealt with separately in §3.2.6. The first two interactions refer to an electron decaying from a higher energy level to a lower one and thus emitting a photon of frequency $\nu = (E_u - E_l)/h$. This decay can be produced either through a self-produced relaxation or through an incoming electromagnetic wave at the right frequency to produce resonance and force the transition. In contrast, induced absorption refers to an electron going to a higher energy level by absorption of an incoming photon with the right frequency.

The energy emitted and absorbed per unit volume, $\mathrm{d}V$, solid angle, $\mathrm{d}\Omega$,

frequency range, $\mathrm{d}\nu$, and time, $\mathrm{d}t$, are given respectively by

$$\mathrm{d}E_{\mathbf{em}} = j_\nu \Psi(\nu)\,\mathrm{d}V\,\mathrm{d}\Omega\,\mathrm{d}\nu\,\mathrm{d}t \tag{C.1}$$

and

$$\mathrm{d}E_{\mathbf{abs}} = e^{\mathrm{ind}}_{\nu,j} \Psi(\nu) I_\nu\,\mathrm{d}V\,\mathrm{d}\Omega\,\mathrm{d}\nu\,\mathrm{d}t, \tag{C.2}$$

where I_ν is the incoming radiation, j_ν is the emission coefficient, $e^{\mathrm{ind}}_{\nu,j}$ is the induced absorption (or extinction) coefficient, and $\Psi(\nu)$ is the normalized Voigt profile. The latter will be discussed in Appendix C.3.3. The subindex j indicates that the quantity refers to the extinction coefficient of only the spectral line in consideration. The total extinction coefficient at a particular wavelength is given by the sum of contributions from each of the individual lines.

The previous expressions can be related to quantum properties of the atoms, are represented by the Einstein coefficients, A_{ul}, B_{ul}, and B_{lu} (Appendix B.3).

Since spontaneous emission occurs isotropically, each photon will have, on average, an energy $\frac{1}{4\pi}h\nu = \frac{1}{4\pi}(E_u - E_l)$ per unit solid angle. If n_u is the number density of atoms with an available electron in the upper level and thus $n_u A_{ul}\,\mathrm{d}t$ is the number density of emitted photons in an interval of time, $\mathrm{d}t$, then

$$\mathrm{d}E_{em} = n_u A_{ul} \frac{h\nu}{4\pi} \Psi(\nu)\,\mathrm{d}V\,\mathrm{d}\Omega\,\mathrm{d}\nu\,\mathrm{d}t \tag{C.3}$$

is an alternate expression to Eq. (C.1) for spontaneous emitted energy. Comparing, one obtains that the emission coefficient in terms of the atom properties is

$$j_\nu = \frac{h\nu}{4\pi} n_u A_{ul} \Psi(\nu). \tag{C.4}$$

Similarly, for the extinction coefficient one finds that the number density of electronic transitions triggered by the incoming radiation in a time interval $\mathrm{d}t$

is $I_\nu n_l B_{lu}\,\mathrm{d}t\,\mathrm{d}\Omega$; thus

$$e^{\mathrm{ind}}_{\nu,j=lu} = h\nu n_l B_{lu}\Psi(\nu), \tag{C.5}$$

where the line index, j, is identified with the particular upper and lower energy level combination (lu).

Why use the superscript "ind"? It turns out that the induced emission is proportional to the incoming intensity (and thus is more akin to induced extinction than spontaneous emission). Hence, it is better to consider the induced emission as a negative extinction such that the full extinction coefficient is given by

$$e_{\nu,lu} = h\nu\Psi(\nu)(n_l B_{lu} - n_u Bul). \tag{C.6}$$

Using Eqs. (B.22) and (B.23) and Boltzmann's Eq. (B.5) yields

$$e_{\nu,lu} = h\nu n_l B_{lu}\Psi(\nu)\left(1 - \frac{n_u}{n_l}\frac{\bar{n}_l}{\bar{n}_u}\,e^{-\frac{hc\bar{\nu}}{k_B T}}\right), \tag{C.7}$$

where the barred $\bar{n}_i$ refers to the number density of atoms with electrons populating level i whenever there is local thermodynamic equilibrium (LTE).

C.2 Line Strength

How does one obtain expressions for A_{ul}, B_{ul}, and B_{lu}? First, note that Eq. (B.23) indicates that it is necessary to find an expression for only one of them.

An expression for B_{lu} is found by noting that

$$\Gamma_{ind-em}\Delta t = \mathtt{w}_{l\to u}, \tag{C.8}$$

where Γ_{ind-em} is the transition rate as defined by Eq. (B.17) and $\mathtt{w}_{l\to u}$ is the transition probability for an interval of time Δt as defined by Eq. (B.44). Hence,

$$B_{lu} I_\nu\,\mathrm{d}\Omega\Delta t = \frac{2\pi}{3\hbar^2 c}\left|d_{lu}\right|^2 I_\nu\,\mathrm{d}\Omega\Delta t. \tag{C.9}$$

Solving for B_{lu}, one finally obtains

$$B_{lu} = \frac{2\pi}{3\hbar^2 c} |d_{lu}|^2 . \tag{C.10}$$

If the upper and lower levels are degenerate, one obtains the total Einstein coefficient by summing over all upper degenerate levels and averaging over the degenerate lower levels:

$$B_{lu} = \frac{2\pi}{3\hbar^2 c} \frac{1}{g_l} \sum_l \sum_u |d_{lu}|^2 , \tag{C.11}$$

where g_l is the degeneracy of the lower level. From Eq. (C.7),

$$e_{\nu,lu} = \frac{4\pi^2 \nu_{lu} n_l}{3hc} \Psi(\Delta\nu) \frac{1}{g_l} \sum_l \sum_u |d_{lu}|^2 \left(1 - \frac{n_u}{n_l} \frac{\bar{n}_l}{\bar{n}_u} e^{-\frac{h\nu_{lu}}{k_B T}} \right) , \tag{C.12}$$

where the subscript lu to the frequency symbol (ν_{lu}) indicates that it refers to the central wavelength of the line.

Now, reordering, the extinction coefficients are

$$e_{\nu,lu} = \frac{\pi e^2 n_l}{m_e c} \Psi(\Delta\nu) f_{lu} \left(1 - \frac{n_u}{n_l} \frac{\bar{n}_l}{\bar{n}_u} e^{-\frac{h\nu_{lu}}{k_B T}} \right) \tag{C.13}$$

where f_{lu} is the absorption oscillator strength, defined as

$$f_{lu} = \frac{4\pi m_e \nu_{lu}}{3\hbar g_l e^2} \sum |d_{lu}|^2, \tag{C.14}$$

where the sum is performed over all upper and lower levels.

To obtain the extinction coefficient as a function of wavenumber rather than frequency, one divides the previous equation by the speed of light.

Finally, assuming that the atmosphere is in LTE, such that $n_i = \bar{n}_i$, yields

$$e_{\bar{\nu},lu} = \frac{\pi e^2 n_l}{m_e c^2} \Psi(\Delta\nu) f_{lu} \left(1 - e^{-\frac{h\nu_{lu}}{k_B T}} \right) . \tag{C.15}$$

Line strength, which is sometimes referred to in the literature, is defined as

$$S = \int_0^\infty e(\nu, lu) \, \mathrm{d}\nu = \frac{\pi e^2 n_l}{m_e c} f_{lu} \left(1 - \frac{n_u}{n_l} \frac{\bar{n}_l}{\bar{n}_u} e^{-\frac{h\nu_{lu}}{k_B T}} \right) . \tag{C.16}$$

Note that the oscillator strength f_{lu} is defined as such, because if it were equal to 1 (and discarding the term for induced emission), one would recover the result of a classical treatment of radiation as an oscillation, where the total cross section is given by

$$\int_0^\infty e(\nu, lu)\,\mathrm{d}\nu = \frac{S_{\text{class}}}{n_l} = \frac{\pi e^2}{m_e c}. \tag{C.17}$$

C.3 Line Broadening

The two most important broadening factors are Doppler and Lorentz broadening, which combine together to form the commonly used Voigt profile.

C.3.1 Doppler Broadening

A photon emitted from a particle with a non-zero radial velocity with respect to the observer is received at a different wavelength from that at which it would have been received if the radial velocity were zero. This shift of observed wavelength, $\Delta\lambda$, (or wavenumber, $\Delta\bar{\nu}$) is related to the velocity, v, by

$$v = c\frac{\Delta\lambda}{\Lambda_0} = c\frac{\Delta\bar{\nu}}{\bar{V}}. \tag{C.18}$$

If the particles in an atmosphere are in equilibrium, then one can assume that they will follow a Maxwell-Boltzmann velocity distribution (Eq. B.9). However, only the radial velocity of the particle will affect the line profile. Integrating over the two orthogonal velocity directions one obtains the Doppler velocity distribution, D, given by

$$\bar{D}(v_r)\,\mathrm{d}v_r = \frac{c}{\bar{V}}\frac{1}{\alpha_D}\sqrt{\frac{\ln 2}{\pi}}\,e^{-\ln 2\left(\frac{\bar{\nu}}{c}\frac{v_r}{\alpha_D}\right)^2}\,\mathrm{d}v_r, \tag{C.19}$$

where the bar indicates that it is given as a function of velocities and

$$\alpha_D = \frac{\bar{V}}{c}\sqrt{\frac{2k_B T \ln 2}{m}} \tag{C.20}$$

is the Doppler FWHM.

Alternatively, expressing the Doppler broadening in terms of wavenumber shift yields

$$D(\bar{\nu}, \bar{V})\,\mathrm{d}\bar{\nu} = \frac{1}{\alpha_D}\sqrt{\frac{\ln 2}{\pi}}\, e^{-\ln 2|\bar{\nu}-\bar{V}|^2/\alpha_D^2}\,\mathrm{d}\bar{\nu}. \tag{C.21}$$

C.3.2 Lorentz Broadening

The Lorentz profile is in reality the convolution of two effects: collision among particles and finite lifetime of the energy levels that produce a natural broadening.

This section mostly outlines the procedures utilized by Mihalas (1978, chap. 9) for the derivation of the Lorentz profile. It will omit some calculations that the reader can find in Mihalas's book.

Natural Damping Broadening

As depicted by Einstein's A_{ul} coefficient, an electron will not stay at the same excited energy level forever. Instead, it will relax to a level of lower energy through the emission of a photon. This implies an uncertainty in time which, using the Heisenberg uncertainty relation (Eq. B.46), in turn implies an uncertainty in energy, or a natural broadening of the spectral line.

In a system with only two levels, Einstein's A_{ul} coefficient can also be considered as the reciprocal of the upper level lifetime. Hence, a dampened monochro-

matic wave with wavenumber, $\bar{\nu}_{ul}$, is represented by the function

$$\phi_{\text{damping}} = u_u(\mathbf{r})\, e^{-(\mathrm{i}\,\frac{2\pi}{c}\bar{\nu}_{ul} + A_{ul}/2)t}, \tag{C.22}$$

where c is the speed of light and u_u is the upper level's spatial wave function, of unimportant value in this case.

The Fourier transform of Eq. (C.22) is the natural damping emission profile

$$j_{\bar{\nu}} = \frac{cA_{ul}}{8\pi^3} \frac{1}{(\bar{\nu} - \bar{V})^2 + \left(\frac{cA_{ul}}{4\pi}\right)^2}. \tag{C.23}$$

Now, considering that both the upper and lower level of the transition can decay to several even-lower levels, the following normalized natural damping line profile is obtained

$$L_{\text{nat}}(\bar{\nu}, \bar{V}) = \frac{\Gamma_{\text{nat}}}{\pi} \frac{1}{(\bar{\nu} - \bar{V})^2 + \Gamma_{\text{nat}}^2}, \tag{C.24}$$

where Γ_{nat} is the natural decay rate given by

$$\Gamma_{\text{nat}} = \frac{c}{2\pi} \frac{1}{2} \left(\sum_{i<l} A_{li} + \sum_{j<u} A_{uj} \right), \tag{C.25}$$

where A_{mn} are the Einstein coefficients for spontaneous emission from level m to n. Note that the fraction $c/2\pi$ appears in the decay rate because the units are wavenumbers.

Collision Broadening

At this point, only the Weisskopf approximation for classical impact collision broadening is considered. There are several improved approximations, which would render more accurate profiles when modeling the far wings of spectral lines (Burrows and Volobuyev, 2003); however, for the narrow water lines relevant for this work, utilizing the Weisskopf approximation suffices.

Improved theories include, among others, the Lindholm approximation, approximations to a statistical view of the collisions, and even an accurate quantum mechanical calculation (refer to sections 9-3, 9-4, and 9-5 of the book by Mihalas, 1978, and the paper by Burrows and Volobuyev).

Lorentz was the first to consider an atom to be a radiating oscillator that undergoes an instantaneous change in phase during encounters with radiating particles. If the unperturbed time between collisions is T, then a monochromatic emitted wavetrain, $f(t) = \exp(i\omega_0 t)$ has as its Fourier transform

$$F(\omega, T) = \int_0^T e^{i(\omega_0 - \omega)t}\, \mathrm{d}t = \frac{\exp[i(\omega - \omega_0)T] - 1}{i(\omega - \omega_0)}. \tag{C.26}$$

Note that the energy spectrum of the above equation is given by the well known relation

$$E(\omega, T) = \frac{1}{2\pi} F(\omega)\bar{F}(\omega), \tag{C.27}$$

where $\bar{F}$ is the complex confugate of F.

However, obtaining a mean energy spectrum requires a weighted average over all possible collision times, T. The weight would be given by the probability of collision in the particular time interval. If $\bar{T}$ is the mean time between collisions, then

$$W(T)\, \mathrm{d}T = e^{-T/\bar{T}}\, \mathrm{d}T/\bar{T} \tag{C.28}$$

is the probability that two collisions will take place between times T and $T + \mathrm{d}T$.

Hence, a mean, normalized energy spectrum is given by

$$\begin{aligned} E(\omega) =& \frac{1}{2\pi} \int_0^\infty \bar{F}(\omega, T) F(\omega, T)\, e^{-T/\bar{T}} \frac{\mathrm{d}T}{\bar{T}} \\ =& \frac{\Gamma_{\mathrm{col}}}{\pi} \frac{1}{(\bar{v} - \bar{V})^2 + \Gamma_{\mathrm{col}}^2}, \end{aligned} \tag{C.29}$$

where

$$\Gamma_{\mathrm{col}} = \frac{1}{2\pi c} \frac{1}{\bar{T}}. \tag{C.30}$$

Note that Eq. (C.29) has the same shape as Eq. (C.24); this kind of function is known as a Lorentz profile function. The convolution of these two profiles is simply

$$L(\bar{v}, \bar{V}) = \frac{\alpha_L}{\pi} \frac{1}{(\bar{v} - \bar{V})^2 + \alpha_L^2}, \tag{C.31}$$

where

$$\alpha_L = \Gamma_{\text{col}} + \Gamma_{\text{nat}}. \tag{C.32}$$

Or, in words, a convolution of two or more Lorentz profiles is another Lorentz profile with a width that is the sum of the width of every profile being convolved.

To obtain an estimate of the mean time between collisions, $\bar{T}$, note that, by definition, the mean free path, $\mathcal{L}_{\text{mfp}}$, is such that

$$\mathcal{L}_{\text{mfp}} \sigma_c n_T = 1, \tag{C.33}$$

where σ_c is the collision cross section and n_T is the number density of particles. Alternatively, the mean free path is also the time between collisions multiplied by a mean relative velocity.

If the impactors are different molecules, an average relative velocity can be obtained by a weighted average of the relative velocity with respect to each kind (Eq. B.13). The weight has to be proportional to the likeliness of impacting each kind. A good approximation is that the likeliness of impacting particle i is proportional to the its number density (n_i). Hence,

$$\frac{1}{\bar{T}} = \frac{1}{n_T} \sum_i n_i \sigma_c n_T v_i = \sigma_c \sqrt{\frac{8 k_B T}{\pi}} \sum_i n_i \sqrt{\left(\frac{1}{m_r} + \frac{1}{m_i} \right)}. \tag{C.34}$$

Finally, one obtains the Lorentz width,

$$\alpha_L = \Gamma_{nat} + \frac{\sigma_c}{\pi c}\sqrt{\frac{2k_B T}{\pi}}\sum_i n_i \sqrt{\left(\frac{1}{m_r} + \frac{1}{m_i}\right)}. \tag{C.35}$$

As an acceptable approximation, one can use the classical molecular area as the collision cross section and disregard natural width.

C.3.3 Voigt Profile

The line profile that incorporates Doppler and collisional effects is known as the Voigt profile. It is obtained by convolving Eq. (C.21) for the Doppler broadening profile and Eq. (C.31) for the Lorentz broadening profile. Explictly,

$$\Psi\left(\bar{\nu}, \bar{V}\right) = \int_{-\infty}^{\infty} D(\bar{\nu}', \bar{V}) L(\bar{\nu} - \bar{\nu}', \bar{V})\, \mathrm{d}\bar{\nu}'. \tag{C.36}$$

Several numerical methods have been devised for a quick computation of this function. An excellent review of early methods is presented by Armstrong (1967). However, the method selected for this work is somewhat newer and is described by Pierlushi et al. (1977).

With an appropiate choice of variables, the Voigt function can be expressed as

$$\Psi(x, y) = \frac{y}{\pi}\int_{-\infty}^{\infty} \frac{e^{-t^2}}{y^2 + (x - t)^2}\, \mathrm{d}t, \tag{C.37}$$

or even

$$\Psi(z = x + \mathrm{i}\, y)) = \Re\left[e^{-z^2}\left(1 - \mathrm{erf}(-\mathrm{i}\, z)\right)\right], \tag{C.38}$$

where $x = (\ln 2)^{1/2}(\bar{\nu} - \bar{V})/\alpha_D$, $y = (\ln 2)^{1/2}\alpha_L/\alpha_D$ and $\Re[w]$ refers to the real part of the complex number w.

As described by Pierlushi et al., the quadrant $x, y \geq 0$ is divided into three regions and the following approximated functions are used in each of them. The mathematical expansions were taken from Abramowitz and Stegun (1965).

- *Region I:* rectangle delimited by $x \in [0, 3]$ and $y \in [0, 1.8]$. In this area, the result is the combination of the exact expression

$$e^{-z^2} = e^{-(x^2-y^2)} \left(cos(2xy) - \mathrm{i}\, \sin(2xy)\right) \tag{C.39}$$

and the infinite series:

$$\mathrm{erf}(-iz) = \frac{2}{\sqrt{\pi}} \sum_{n=0}^{\infty} \frac{(-1)^n}{n!(2n+1)} (-\mathrm{i}\, z)^{2n+1} \tag{C.40}$$

$$= \frac{2}{\sqrt{\pi}} (y - \mathrm{i}\, x) \sum_{n=0}^{\infty} \frac{(x^2 - y^2 + \mathrm{i}\, 2xy)^n}{n!(2n+1)}. \tag{C.41}$$

The series is truncated according to the empirical relation

$$n = \begin{cases} 15 & \text{if } x < 1 \\ \lceil 6.842x + 8 \rceil & \text{otherwise.} \end{cases} \tag{C.42}$$

- *Region II* is the area contained by $x \in [3, 5]$ or $y \in [1.8, 5]$ (a 5×5 square less the area of the Region I). Here, the following asymptotic approximation is utilized:

$$\Psi_{\mathrm{II}} = \mathcal{R}\left[\mathrm{i}\, z \left(\frac{0.46131350}{z^2 - 0.19016350} + \frac{0.09999216}{z^2 - 1.78449270} + \frac{0.002883894}{z^2 - 5.52534370}\right)\right]. \tag{C.43}$$

- *Region III* is everything else in the first x, y quadrant (where both are positive). It is also an asymptotic expression:

$$\Psi_{\mathrm{III}} = \mathcal{R}\left[\mathrm{i}\, z \left(\frac{0.51242424}{z^2 - 0.2755510} + \frac{0.05176536}{z^2 - 2.7247450}\right)\right]. \tag{C.44}$$

Why use these old approximations given the much more advanced computer capabilities available today? It is not because of speed, but rather due the roundoff errors that would be incurred otherwise. As shown by Pierlushi et al. (1977), the RMS deviation from the exact solution given these approximations is no bigger than 10^{-5}.

Mathematical Details

D

Selected expressions relevant to this work that do not have a trivial mathematical deduction are detailed in this appendix.

D.1 Bending Angle

In the problem of a light ray passing through an atmosphere as described in §3.2.3, notice that the only absolute reference for an angle is one that can be taken with respect to the distance of closest approach: the vector $\mathbf{r_c}$ in Fig. 3.4.

Then, if ϕ indicates the angle that can be used to follow the direction of the ray in an absolute form, then

$$\phi = \theta + i + K, \tag{D.1}$$

where θ and i are defined in §3.2.3 and K is an arbitrary offset. The derivative of Eq. (3.23) yields

$$\frac{\mathrm{d}n}{\mathrm{d}r} r \sin i + n \sin i + nr \cos i \frac{\mathrm{d}i}{\mathrm{d}r} = 0 \tag{D.2}$$

or

$$\begin{aligned} \frac{\mathrm{d}i}{\mathrm{d}r} &= \frac{-1}{nr\sqrt{1-\sin^2 i}} \left(\frac{\mathrm{d}n}{\mathrm{d}r} r \sin i + n \sin i \right) \\ &= \frac{-\rho}{\sqrt{n^2 r^2 - \rho^2}} \left(\frac{1}{n} \frac{\mathrm{d}n}{\mathrm{d}r} + \frac{1}{r} \right), \end{aligned} \tag{D.3}$$

where Eq. (3.23) was used. Using the above equation and Eq. (3.22) in the derivative of Eq. (D.1) with respect to r,

$$\begin{aligned}\frac{\mathrm{d}\phi}{\mathrm{d}r} &= \frac{\mathrm{d}\theta}{\mathrm{d}r} + \frac{\mathrm{d}i}{\mathrm{d}r} \\ &= \frac{\rho}{\sqrt{n^2r^2-\rho^2}}\left[\frac{1}{r} - \left(\frac{1}{n}\frac{\mathrm{d}n}{\mathrm{d}r} + \frac{1}{r}\right)\right] \\ &= \frac{-\rho\frac{\mathrm{d}n}{\mathrm{d}r}}{n\sqrt{n^2r^2-\rho^2}},\end{aligned} \tag{D.4}$$

an expression that can be integrated to yield Eq. (3.8).

D.2 Variational Calculus in Integral Minimization

This section details how to minimize an integral of the type

$$T = K\int_{x_1}^{x_2} f\left(x, y(x), \frac{\mathrm{d}y(x)}{\mathrm{d}x}\right), \tag{D.5}$$

where K is a constant, and f is any well behaved function of x, y, and $\frac{\mathrm{d}y}{\mathrm{d}x}$.

This function is assumed to have only one extreme value and that it is a minimum. Then,

$$\delta T = 0 \tag{D.6}$$

will set the condition under which the integral will be minimum. The δ symbol indicates path variation.

If x_1 and x_2 are fixed points, then

$$\begin{aligned}
\delta T &= K \int_{x1}^{x2} \delta f \left(x, y(x), \frac{\mathrm{d}y}{\mathrm{d}x}(x) \right) \\
&= K \int_{x1}^{x2} \left(\frac{\partial f}{\partial y} \delta y + \frac{\partial f}{\partial \frac{\mathrm{d}y}{\mathrm{d}x}} \delta \left(\frac{\mathrm{d}y}{\mathrm{d}x} \right) \right) \mathrm{d}x \\
&= K \int_{x1}^{x2} \left(\frac{\partial f}{\partial y} \delta y - \frac{\mathrm{d}}{\mathrm{d}x} \left(\frac{\partial f}{\partial \frac{\mathrm{d}y}{\mathrm{d}x}} \right) \delta y + \frac{\mathrm{d}}{\mathrm{d}x} \left(\frac{\partial f}{\partial \frac{\mathrm{d}y}{\mathrm{d}x}} \delta y \right) \right) \mathrm{d}x \\
0 &= K \int_{x1}^{x2} \left(\frac{\partial f}{\partial y} - \frac{\mathrm{d}}{\mathrm{d}x} \left(\frac{\partial f}{\partial \frac{\mathrm{d}y}{\mathrm{d}x}} \right) \right) \delta y \, \mathrm{d}x + \left(\frac{\partial f}{\partial \frac{\mathrm{d}y}{\mathrm{d}x}} \delta y \right|_{x1}^{x2} . \qquad \text{(D.7)}
\end{aligned}$$

Note that the last term in the last expression is zero because the end points are fixed ($\delta y(x_1) = \delta y(x_2) = 0$). Furthermore, because δy could be any infinitesimal variation of the path at every position x, it is required that the expression inside the integral be zero at each position. Hence,

$$\frac{\partial f}{\partial y} = \frac{\mathrm{d}}{\mathrm{d}x} \left(\frac{\partial f}{\partial \frac{\mathrm{d}y}{\mathrm{d}x}} \right), \qquad \text{(D.8)}$$

an expression known as the "Euler Equation".

D.3 Scaling the Modulation

This section finds an analytical expression that approximately scales the modulation received from the system when only the scale height or the radius of a planet with an isothermal and cloud-free atmosphere are changed. Many planets, include HD 209458b, are clearly non-isothermal at the levels of relevance, but this is the only possible approximation to obtain an estimate applicable to all planets.

Consider first the result from Eq. (3.15): the transit depth is proportional to the relative area between the planet and the star. Now, consider a wavelength range in which the extreme values of modulation (i.e., where the planet is the

least and most transparent) are at wavelengths λ_1 and λ_2, respectively. Then, the modulation range in that wavelength range is given by $\Delta\mathcal{R} = \mathcal{R}_{\lambda_2} - \mathcal{R}_{\lambda_1}$. The corresponding planetary radius difference responsible for the modulation is $\Delta r = r_2 - r_1$, where $\mathcal{R}_{\lambda_i} = (r_i/R_\star)^2$ for a wavelength, λ_i, and a stellar radius, $R_\star$.

Since the only parameter defining the vertical radius scale in an isothermal atmosphere is the scale height, H (Eq. B.52), the radius difference between two pressure levels is proportional to the scale height, $\Delta r = hH$. Then, the modulation range between the two wavelengths is given by

$$\begin{aligned}
\Delta\mathcal{R} &= \mathcal{R}_{\lambda_2} - \mathcal{R}_{\lambda_1} \\
&= \frac{r_2^2}{R_\star^2} - \frac{r_1^2}{R_\star^2} \\
&= \frac{1}{R_\star^2}\left[(r_1 + hH)^2 - r_1^2\right] \\
&= \frac{2r_1 hH}{R_\star^2} + \frac{(hH)^2}{R_\star^2},
\end{aligned} \tag{D.9}$$

where $R_\star$ is the star's radius. The proportionality constant between wavelengths, h, can be assumed to remain constant for different planets with similar composition. Also, the scale height is much smaller than the radius of the planet, and thus the second term in the last equation is much smaller than the first. Finally, the scaling relationship is given by

$$\Delta\mathcal{R}_\lambda \propto \frac{r_1 H}{R_\star^2}. \tag{D.10}$$

Using a reference planet for which we know the modulation difference, the scale height and the least opaque radius ($\Delta\mathcal{R}$, H, and r_1, respectively), we can find the proportionality constant, $2h$, of Eq. (D.9). Then, the modulation extremes of an otherwise similar planet with different values of scale height and

least opaque radius is given by

$$\mathcal{R}_{\lambda_1} = \left(\frac{r_1}{R_\star}\right)^2 \tag{D.11}$$

$$\mathcal{R}_{\lambda_2} = \mathcal{R}_{\lambda_1}\left(1 + 2hH/r_1\right). \tag{D.12}$$

The value of the modulation at wavelengths of intermediate opacity can then be linearly scaled.

transit Details E

E.1 Atmosphere File

The atmosphere file was obtained from the model of Iro et al. (2005). Note that the backslashes at the ends of some of the lines are not part of the original file. They have only been inserted to indicate that such lines are not broken in the original atmosphere file. Use of backlashes will cause errors in `transit`.

```
#Atmosphere title
n Nicolas Iro planetary profile
#zero-point in height is 94358.9, units in km and mbar
z 94358.9
ur 1e5
up 1e3

#abundances by number
q number

#isotope list
i 16.043-CH4 28.01CO !0Water 2.016IonMolHyd 1.008IonHyd 39.0983K 22.989770Na 63.8TiO

f 0-1H1H16O  = 0.997    Water
f 0-1H2H16O  = 0.000508 Water
f 0-1H1H17O  = 0.000508 Water
f 0-1H1H18O  = 0.001984 Water
f 2.016H2    = 0.85     other
f 4.002602He = 0.15     other

#rad-z pres temp q_i...
-6797.21 0.3488E+07 5276.19885762853                                                    \
2.288755146204095E-005 3.355625569829411E-004 6.996799290255744E-004 1.971551592148621E-007  \
2.002971522545255E-006

-6605.93 0.3081E+07 5135.52171269482                                                    \
2.464749893568713E-005 3.585631604628022E-004 6.967625071026350E-004 1.445866793768784E-007  \
1.654991461389484E-006 3.493150597999350E-008 1.755735929971673E-006 8.307058546994134E-009
```

```
-6418.18 0.2719E+07 4996.56400991509                                                    \
2.620468808952703E-005 3.803359167307499E-004 6.936042525387732E-004 1.047088367348490E-007  \
1.354797601068482E-006 3.802896954651508E-008 1.898600537564553E-006 9.433918475820438E-009

-6234.42 0.2398E+07 4859.67345825839                                                    \
2.752634296239660E-005 4.006824153013065E-004 6.902609958403700E-004 7.475414445073374E-008  \
1.096662815080397E-006 4.149103377569838E-008 2.044256044209157E-006 1.071207273952752E-008

-6055.65 0.2115E+07 4725.60624725833                                                    \
2.859355760562810E-005 4.194213340432474E-004 6.867708541780253E-004 5.276735044063724E-008  \
8.798194236751479E-007 4.535349489514384E-008 2.191308616464540E-006 1.216101248354721E-008

-5881.45 0.1865E+07 4594.07087686937                                                    \
2.941271161600030E-005 4.365825452893958E-004 6.831221304823646E-004 3.678123725724853E-008  \
6.989242709096753E-007 4.966911601143299E-008 2.337847977933361E-006 1.381270049541165E-008

-5712.44 0.1645E+07 4465.56057153885                                                    \
2.999746350053497E-005 4.521346649917112E-004 6.793093871890548E-004 2.533513394545432E-008  \
5.499183985529492E-007 5.445772343841498E-008 2.480837748867101E-006 1.569319877697437E-008

-5548.20 0.1451E+07 4339.80360764891                                                    \
3.037572931562274E-005 4.661750702092626E-004 6.753041951788058E-004 1.722186434192596E-008  \
4.281210685161056E-007 5.976230159833208E-008 2.618192476348203E-006 1.784232994919246E-008

-5387.74 0.1279E+07 4216.08115684046                                                    \
3.058046899466417E-005 4.788534128488691E-004 6.710710031892665E-004 1.151703898903291E-008  \
3.290561966637530E-007 6.606929200946904E-008 2.748414873179922E-006 2.031840496429680E-008

-5231.46 0.1127E+07 4094.74624705575                                                    \
```

```
3.064471918028774E-005 4.902099056258669E-004 6.666302924152087E-004 7.576755382974266E-009  \
2.496233867517354E-007 7.300272925821537E-008 2.870085841385745E-006 2.316399012849762E-008

-5080.11 0.9934E+06 3976.43759165079                                                          \
3.060453997970839E-005 5.002798692012535E-004 6.620493261473886E-004 4.914425695644014E-009  \
1.871948148098462E-007 8.054956629770078E-008 2.980391718927080E-006 2.641651642605998E-008

-4933.25 0.8757E+06 3860.87093829006                                                          \
3.049583664674147E-005 5.091869874627665E-004 6.573973188356611E-004 3.138385370927014E-009  \
1.386348871768355E-007 8.871134582371098E-008 3.078711251490027E-006 3.013767882817131E-008

-4790.92 0.7721E+06 3748.13485898742                                                          \
3.035227796915957E-005 5.170180396770463E-004 6.527870618903489E-004 1.972905015530588E-009  \
1.013742084785055E-007 9.743300274232966E-008 3.164666573773028E-006 3.438113092258683E-008

-4653.16 0.6810E+06 3638.33043109244                                                          \
3.020530944247117E-005 5.238555382928619E-004 6.483495447070146E-004 1.222090316014825E-009  \
7.325756009364535E-008 1.066776042968723E-007 3.238643233080199E-006 3.919576733124904E-008

-4519.90 0.6009E+06 3531.46206943571                                                          \
3.008422053990479E-005 5.297816493598613E-004 6.442121210924398E-004 7.458885944672313E-010  \
5.231581419575189E-008 1.163753770107151E-007 3.301192000477421E-006 4.462475371298438E-008

-4391.30 0.5306E+06 3427.72284146669                                                          \
3.001688778329236E-005 5.348609423100703E-004 6.404919191740956E-004 4.488737311240950E-010  \
3.693584079057801E-008 1.264775684543813E-007 3.353029705780061E-006 5.068319605033181E-008

-4266.77 0.4687E+06 3326.79043865894                                                          \
3.002884259618048E-005 5.391756227181210E-004 6.372569848011271E-004 2.659841992979277E-010  \
```

```
2.575810446170245E-008 1.366823087307697E-007 3.395399669404588E-006 5.739081140199031E-008

-4145.97 0.4142E+06 3228.71188470783                                                    \
3.014377503339654E-005 5.427815013874639E-004 6.345541537948967E-004 1.551940635066201E-010  \
1.774259522560081E-008 1.467753604071609E-007 3.429401669081372E-006 6.471388618795448E-008

-4028.99 0.3663E+06 3133.60458723210                                                    \
3.039205589444527E-005 5.457164438434534E-004 6.324108919010160E-004 8.922033557139853E-011  \
1.207596647513920E-008 1.565347963195306E-007 3.456131706092096E-006 7.256953194790490E-008

-3806.75 0.2872E+06 2951.76341385501                                                    \
3.144684291424023E-005 5.496855944427959E-004 6.298198323949993E-004 2.814031942881038E-011  \
5.386068950791445E-009 1.743729555661600E-007 3.492141005018472E-006 8.940745491165733E-008

-3701.01 0.2545E+06 2865.01458616096                                                    \
3.228148992852770E-005 5.508135405689901E-004 6.292940722148292E-004 1.543327715450404E-011  \
3.529099622848649E-009 1.821417513611527E-007 3.503315666548271E-006 9.803228588508286E-008

-3500.25 0.2006E+06 2699.92692996258                                                    \
3.484371416048080E-005 5.513036410986113E-004 6.298377110701320E-004 4.437303675884455E-012  \
1.459568458108881E-009 1.950333163932991E-007 3.515840804504522E-006 1.146516627893646E-007

-3404.47 0.1782E+06 2620.92622677873                                                    \
3.664594850997878E-005 5.506872722570576E-004 6.308850744847525E-004 2.314847122389454E-012  \
9.181896624719312E-010 2.001805807158007E-007 3.518358979435843E-006 1.223120918259154E-007

-3311.88 0.1585E+06 2544.74316773400                                                    \
3.886397732496781E-005 5.494655578893799E-004 6.324786427549295E-004 1.190914162181370E-012  \
5.709785652737202E-010 2.044757694851074E-007 3.518912303106363E-006 1.292837676941098E-007
```

```
-3124.57 0.1242E+06 2391.74982836073                                                    \
4.535760081019312E-005 5.445916458263877E-004 6.379608336997405E-004 2.771582127510248E-013  \
2.002741857229530E-010 2.111820087615975E-007 3.514746460266225E-006 1.414883613525198E-007

-3019.91 0.1078E+06 2306.87359908730                                                    \
5.053374077505516E-005 5.401309126660482E-004 6.426712014512218E-004 1.138898225572472E-013  \
1.053768133257926E-010 2.138860198193507E-007 3.509334227212243E-006 1.469988217233450E-007

-2785.91 0.7787E+05 2138.13073954986                                                    \
6.316410349090860E-005 5.286762936095931E-004 6.544055710828475E-004 1.566300436170525E-014  \
2.523834449407797E-011 2.174633892447384E-007 3.492089815859760E-006 1.550865322033667E-007

-2657.94 0.6488E+05 2039.83630645563                                                    \
7.240957500651794E-005 5.200688880517990E-004 7.154798776953539E-004 4.299698777909407E-015  \
9.825535693476973E-012 2.187738059313772E-007 3.467587873636615E-006 1.376692814379858E-008

-2524.00 0.5340E+05 1969.26677183831                                                    \
7.728097221575569E-005 5.155270430823294E-004 7.244652258174865E-004 1.531235536411911E-015  \
4.716225505438873E-012 2.193764522588350E-007 3.452822263246455E-006 1.571758506344790E-009

-2384.83 0.4346E+05 1904.17248806066                                                    \
8.105871786798106E-005 5.119971764282897E-004 7.285146858320986E-004 5.483208543892237E-016  \
2.283418938336183E-012 2.197791359067302E-007 3.437604771843812E-006 1.860855373350620E-010

-2240.82 0.3501E+05 1856.12640728984                                                    \
7.723594223512016E-005 5.159885043868562E-004 7.245701170301493E-004 2.387699484418781E-016  \
1.294219079053526E-012 2.199846542405735E-007 3.429259419973211E-006 3.691911252872751E-011
```

```
-1949.32 0.2250E+05 1791.60938166202                                                    \
5.787140818047784E-005 5.355527853804517E-004 7.049693568018843E-004 6.824553455252472E-017  \
5.760157996888339E-013 2.201593207553610E-007 3.428123910894232E-006 4.188477016930382E-012

-1428.69 0.1000E+05 1758.99546000148                                                    \
1.734166314399184E-005 5.762380702092477E-004 6.641968162734310E-004 2.633559121724432E-017  \
3.752756931519752E-013 2.200730703480201E-007 3.467313367575108E-006 2.330355993632967E-012

-1324.95 0.8500E+04 1749.25163068056                                                    \
1.382505901110546E-005 5.797757954910212E-004 6.606513714242072E-004 2.052804555778935E-017  \
3.289725833696616E-013 2.200741383438836E-007 3.471780841836758E-006 1.787830396569290E-012

-1223.71 0.7250E+04 1745.06893914399                                                    \
1.055528319290673E-005 5.830618984732982E-004 6.573582543431500E-004 1.763721972445336E-017  \
3.108722155347647E-013 2.200475813303434E-007 3.478231713534466E-006 1.742119392203251E-012

-1103.79 0.6000E+04 1738.47329663072                                                    \
7.744674952076294E-006 5.858889387263134E-004 6.545248832222118E-004 1.430250090173924E-017  \
2.840828237540767E-013 2.200243271185781E-007 3.484620275795773E-006 1.569642667264356E-012

-956.224 0.4750E+04 1734.19075205923                                                    \
5.090744862041361E-006 5.885581483713632E-004 6.518489733397215E-004 1.180932413688898E-017  \
2.679389936177240E-013 2.199720765633915E-007 3.493297035809025E-006 1.636815351748789E-012

-765.394 0.3500E+04 1725.65313619064                                                    \
3.009614323614736E-006 5.906537706268107E-004 6.497466480399942E-004 8.718038110361397E-018  \
2.380665872016611E-013 2.199179990390133E-007 3.502331487314653E-006 1.511387582938990E-012

-488.414 0.2250E+04 1716.41297206842                                                    \
```

```
1.362358662306404E-006 5.923122421333354E-004 6.480783017942145E-004 5.928185236565990E-018  \
2.092302727192559E-013 2.198102980568394E-007 3.514497613320899E-006 1.543108659458339E-012

0.00 0.1000E+04 1683.21187515680                                                              \
3.703368243927029E-007 5.933107526665509E-004 6.470654468999297E-004 2.149064013993947E-018  \
1.297324979138093E-013 2.197262907132810E-007 3.528072499267953E-006 7.356855526281815E-013

101.73 0.8500E+03 1674.13951856672                                                            \
2.924379280955064E-007 5.933889653632118E-004 6.469852426197597E-004 1.670261337140408E-018  \
1.134594616027361E-013 2.197314647223343E-007 3.529790906300395E-006 5.603333104537368E-013

200.93 0.7250E+03 1665.68063409199                                                            \
2.313298736573261E-007 5.934499407736133E-004 6.469220529534724E-004 1.313296071736520E-018  \
1.000003819709663E-013 2.197335879739817E-007 3.531479778952993E-006 4.361249116744039E-013

318.42 0.6000E+03 1653.52899661375                                                            \
1.789416916119284E-007 5.935023643796895E-004 6.468679361543467E-004 9.453821093790923E-019  \
8.321763643840317E-014 2.197556738627437E-007 3.532890681555699E-006 2.904050215787555E-013

462.39 0.4750E+03 1634.39067658349                                                            \
1.363385404131417E-007 5.935455110697533E-004 6.468242775558628E-004 5.776505459566672E-019  \
6.195960868200845E-014 2.198196175412170E-007 3.533515038952122E-006 1.409378864944487E-013

648.27 0.3500E+03 1605.81182400115                                                            \
9.996334463590903E-008 5.935822131251036E-004 6.467868243256082E-004 2.782020192371910E-019  \
3.936280981545612E-014 2.199287658878769E-007 3.533166422271902E-006 4.393356371034336E-014

911.08 0.2250E+03 1547.29103639709                                                            \
7.915488310539901E-008 5.936012074274382E-004 6.467616207735672E-004 6.387097319542544E-020  \
```

```
1.474548116069202E-014 2.201732643012766E-007 3.526620631233242E-006 2.835578571920567E-015

1369.04 0.1000E+03 1432.01745480159                                                    \
6.584535982208594E-008 5.935894376834594E-004 6.467157545641794E-004 2.682834533100636E-021  \
1.681075012195499E-015 2.204741524685072E-007 3.498596358573177E-006 5.644334928315287E-018

1456.76 0.8500E+02 1393.44970588608                                                    \
8.116145299049089E-008 5.935593788785797E-004 6.467107401372983E-004 8.841630208343351E-022  \
7.489217702719806E-016 2.205369394428895E-007 3.477012484218299E-006 4.872618672592226E-019

1541.09 0.7250E+02 1377.87891486445                                                    \
7.388008818166155E-008 5.935595438384308E-004 6.466955778201595E-004 5.305026970775589E-022  \
5.336354287503672E-016 2.205517106922336E-007 3.470769242552760E-006 1.909264491001369E-019

1639.65 0.6000E+02 1341.14487077742                                                    \
8.762761034007249E-008 5.935268701835508E-004 6.466842573313651E-004 1.673787251538080E-022  \
2.320877608837707E-016 2.205871499930660E-007 3.441880196999766E-006 1.834956386136150E-020

1758.67 0.4750E+02 1314.76017886215                                                    \
8.301937019519268E-008 5.935155469244793E-004 6.466608981582999E-004 6.712905900284050E-023  \
1.240421565514235E-016 2.206031209687680E-007 3.421729406069286E-006 1.835048748722489E-020

1910.17 0.3500E+02 1269.01704875414                                                    \
9.604044231546902E-008 5.934698641222280E-004 6.466325487217570E-004 1.335845888616898E-023  \
3.928590699193770E-017 2.206246156236486E-007 3.368268192222678E-006 1.835159745260454E-020

2121.95 0.2250E+02 1226.61094637323                                                    \
8.409525606102767E-008 5.934445773217067E-004 6.465781048215436E-004 2.508225173949297E-024  \
1.254296330074858E-017 2.206355341583309E-007 3.316895551564453E-006 1.835222447537323E-020
```

```
2493.71 0.1000E+02 1159.92593670299                                                    \
6.030047199126184E-008 5.933920640738683E-004 6.464702054185623E-004 1.377505074911249E-025  \
1.760879018341730E-018 2.206450369843365E-007 3.223048428295327E-006 1.835274169846177E-020

2566.00 0.8500E+01 1144.29379241972                                                    \
6.020087701601284E-008 5.933702785685571E-004 6.464446712825595E-004 6.781740610501495E-026  \
1.075053754298304E-018 2.206465346002604E-007 3.195137177222019E-006 1.835281082285209E-020

2636.13 0.7250E+01 1138.40893894715                                                    \
4.957886271299352E-008 5.933721716332472E-004 6.464274355001855E-004 4.928020605005904E-026  \
8.904517329040475E-019 2.206467607346836E-007 3.193910618249242E-006 1.835283241518375E-020

2718.85 0.6000E+01 1123.60649310289                                                    \
4.664257089653460E-008 5.933519567733721E-004 6.463988827301901E-004 2.421385691997266E-026  \
5.485790005160263E-019 2.206478191810600E-007 3.169985716621892E-006 1.835288100810174E-020

2819.95 0.4750E+01 1114.91257671644                                                    \
3.535923501581917E-008 5.933487426241126E-004 6.463759653530110E-004 1.490513915849843E-026  \
4.106843150419853E-019 2.206481085442388E-007 3.167275743597723E-006 1.835290432236241E-020

2950.61 0.3500E+01 1096.34891259506                                                    \
2.910259238614511E-008 5.933216767044451E-004 6.463352085487331E-004 5.704881297937894E-027  \
2.176294617203540E-019 2.206490337813278E-007 3.142692805038582E-006 1.835294625630454E-020

3137.11 0.2250E+01 1081.07115091637                                                    \
1.711480897822868E-008 5.933035064622309E-004 6.462984491035147E-004 2.307462012583610E-027  \
1.271129654906191E-019 2.206494029255673E-007 3.138909110904416E-006 1.835297220761401E-020
```

```
3474.88 0.1000E+01 1049.74496697843                                                    \
7.188241818627557E-009 5.932426534427921E-004 6.462239954460741E-004 3.549882688253392E-028  \
4.014566194446156E-020 2.206502054904095E-007 3.119862776483724E-006 1.835300991268830E-020

3542.19 0.8500E+00 1041.49001873745                                                    \
6.382047297905780E-009 5.932225165622432E-004 6.462020329723868E-004 2.190754686209038E-028  \
2.928084542002803E-020 2.206504387879163E-007 3.110444872435968E-006 1.835301718717175E-020

3607.94 0.7250E+00 1038.03736433969                                                    \
5.065690231277813E-009 5.932147486793275E-004 6.461942924525352E-004 1.708040380695014E-028  \
2.563270211665825E-020 2.206504480271155E-007 3.113440837401368E-006 1.835301974974334E-020

3685.96 0.6000E+00 1029.34737826835                                                    \
4.331023463946267E-009 5.931917678375487E-004 6.461700341925813E-004 1.008443538232451E-028  \
1.824694863171526E-020 2.206506573997933E-007 3.104791816211989E-006 1.835302600328720E-020

3781.98 0.4750E+00 1023.38512719801                                                    \
3.167205393147245E-009 5.931758955476480E-004 6.461549226045316E-004 6.644156155743893E-029  \
1.440946812611130E-020 2.206507103758788E-007 3.106343401300954E-006 1.835302960210022E-020

3906.92 0.3500E+00 1011.05034206693                                                    \
2.379341575437494E-009 5.931393558048795E-004 6.461178395856105E-004 3.026512304616464E-029  \
8.756144113931447E-021 2.206509475269083E-007 3.096441423773103E-006 1.835303626262926E-020

4086.44 0.2250E+00 998.854385382341                                                    \
1.365924348301548E-009 5.931004305963297E-004 6.460814288611472E-004 1.277618351107495E-029  \
5.288471638708721E-021 2.206510733666631E-007 3.095749966903877E-006 1.835304137776320E-020

4411.72 0.1000E+00 972.778775262557                                                    \
```

```
5.595009078553486E-010 5.930042571166037E-004 6.459886451213009E-004 2.045519810532742E-030  \
1.723060975546530E-021 2.206513916862058E-007 3.083880576048005E-006 1.835304932848944E-020

4476.34 0.8500E-01 964.654346578762                                                          \
5.113177363807803E-010 5.929704143915963E-004 6.459538895140993E-004 1.189884803106640E-030  \
1.199588404216898E-021 2.206515146051652E-007 3.074978493602387E-006 1.835305120597954E-020

4539.34 0.7250E-01 962.085400069256                                                          \
4.009970066324653E-010 5.929593976373931E-004 6.459449024492017E-004 9.486832343044962E-031  \
1.068694738659730E-021 2.206515095159268E-007 3.078095341542228E-006 1.835305163842471E-020

4613.99 0.6000E-01 953.389362218851                                                          \
3.551566988603801E-010 5.929202754024351E-004 6.459050694011111E-004 5.211952436025849E-031  \
7.188343335516197E-022 2.206516217876899E-007 3.069611467925149E-006 1.835305326289981E-020

4705.65 0.4750E-01 948.417010594395                                                          \
2.583622274539339E-010 5.928968583297595E-004 6.458839069363391E-004 3.461973897848482E-031  \
5.712529075994854E-022 2.206516402610919E-007 3.071271823320180E-006 1.835305397051221E-020

4824.61 0.3500E-01 935.494980221628                                                          \
2.081014773749490E-010 5.928317282581631E-004 6.458180611174130E-004 1.369279911840529E-031  \
3.106065187955959E-022 2.206517741630643E-007 3.060368456858460E-006 1.835305574144764E-020

4995.01 0.2250E-01 923.745505143888                                                          \
1.242358424106194E-010 5.927669186559264E-004 6.457559138836316E-004 5.326552367871490E-032  \
1.758862667708011E-022 2.206518399719082E-007 3.058332683361342E-006 1.835305689157163E-020

5302.28 0.1000E-01 894.425427114787                                                          \
6.398156898532973E-011 5.925773559235020E-004 6.455661031899348E-004 5.371084621077315E-033  \
```

```
3.982421606294403E-023 2.206520239434356E-007 3.041221713747292E-006 1.835305894708513E-020

5363.05 0.8500E-02 885.105598721544                                                    \
6.349117718569104E-011 5.925073452564027E-004 6.454936981696756E-004 2.645618588651542E-033  \
2.432379319725489E-023 2.206520780667209E-007 3.032921095761440E-006 1.835305942092552E-020

5422.23 0.7250E-02 882.413862600836                                                    \
5.068437176736252E-011 5.924861310808710E-004 6.454742039359954E-004 2.033824994420723E-033  \
2.105598759817443E-023 2.206520801997157E-007 3.034602111627617E-006 1.835305949136542E-020

5492.26 0.6000E-02 872.139288370608                                                    \
4.972930677203244E-011 5.924006920483541E-004 6.453860910898831E-004 9.086930299899988E-034  \
1.203642929974097E-023 2.206521274310172E-007 3.026409945615476E-006 1.835305989353975E-020

5578.13 0.4750E-02 867.118015874396                                                    \
3.726290774508451E-011 5.923562171371998E-004 6.453433802219016E-004 5.677060914872816E-034  \
9.114243549941630E-024 2.206521362360184E-007 3.027294224131459E-006 1.835306000510109E-020

5689.42 0.3500E-02 852.737588106571                                                    \
3.412313992971963E-011 5.922178678245169E-004 6.452016723626029E-004 1.729172913774909E-034  \
4.034512699330112E-024 2.206521822432874E-007 3.018086332236971E-006 1.835306038901758E-020

5848.53 0.2250E-02 837.630021972832                                                    \
2.487763831063934E-011 5.920527048153071E-004 6.450352716825251E-004 4.491620569119692E-035  \
1.662491722938948E-024 2.206522124769209E-007 3.012794147608094E-006 1.835306064780147E-020

6136.24 0.1000E-02 817.245427002899                                                    \
1.091169324405212E-011 5.917912047296717E-004 6.447764903151737E-004 6.122215164970880E-036  \
4.769198571154839E-025 2.206522358877930E-007 3.012204191584048E-006 1.835306082562170E-020
```

E.2 Built-in Help

The following output is obtained by invoking `transit -h`.

```
Usage:
transit [options]

  Where [options] are (note that whenever there is a
mandatory argument, it is mandatory for both short and
long options)...


GENERAL ARGUMENTS
 -V, --version
          Prints version number and exit.
 -h, --help
          Prints list of possible parameters.
 -d, --defaults
          Prints default values of the different variable.
 -v, --verb
          Increase the verbose level by one .
 -q, --quiet
          Decrease the verbose level to the minimum .
 -p, --paramf=<filename>
          Use filename to read  parameters  in  addition  to
          default file(s): './.transitrc'.

INPUT/OUTPUT
 -o, --output=<outfile>
          Change output file name, a  dash  (-)  directs  to
          standard output. Default: -.
 --atm=<atmfile>
          File   containing   atmospheric   info    (Radius,
          pressure,  temperature).  A  dash  (-)   indicates
          alternative input. Default: -.
 --linedb=<linedb>
          File containing line information (TLI  format,  as
          given by 'lineread'. Default: ./res/lineread.tli.
 --outtoomuch=<filename>
          Ouputs depth where toomuch optical depth has  been
          attained as a function of wavelength .
 --outsample=<filename>
          Outputs   sampling   information.   A   dash   (-)
```

```
          indicates standard input. By default there  is  no
          such output.

RADIUS OPTIONS (planetary radii units, unless stated otherwise)
 -r, --radius
          Interactively input radius parameters.
 --rad-low=<radius>
          Lower radius. 0 if you  want  to  use  atmospheric
          data minimum. Default: 0.
 --rad-high=<radius>
          Higher radius. 0 if you want  to  use  atmospheric
          data maximum. Default: 0.
 --rad-delt=<spacing>
          Radius spacing. 0 if you want to  use  atmospheric
          data spacing. Default: .5.
 --rad-fct=<factor>
          Radius factor.  Multiplicating  radius  values  by
          this gives centimeters. Default: 0.

ATMPOSPHERE OPTIONS
 --number-abund
          Indicates that  given  abundances  are  by  number
          rather than by mass.
 --onept=<press,temp,extra_iso>
          Don't  calculate  transit  spectra,  just   obtain
          spectra for  a  given  pressure  and  temperature.
          Unless oneabund is  also  specified  and  has  the
          correct number of isotopes,  the  abundances  will
          be asked interactively.
 --oneextra=<mass1name1,mass2name2,...>
          It only has effect with --onept,  a  list  of  the
          atomic mass  and  names  for  the  extra  isotopes
           specified with --onept. If it  doesn't  have  the
          right amount  of  values,  the  program  will  ask
          interactively.
 --oneabund=<q1,...>
          It also only has effect with --onept,  a  list  of
          the abundances of the different  isotopes.  If  it
          is omitted or doesn't have  the  right  amount  of
          values, the program will ask  interactively.  Note
          that the order of isotopes is the  same  given  in
          the TLI data file.
 --onept-interactive
          Wants  to  give  abundances   and   pressure   and
```

```
          temperature interactively through terminal input.
 --allowq=<value>
          How much less than one is  accepted,  so  that  no
          warning is issued if abundances  don't  ad  up  to
          that. Default: 0.01.

WAVELENGTH OPTIONS (all in nanometers)
 -w, --wavelength
          Interactively input wavelength parameters.
 --wl-low=<wavel>
          Lower wavelength. 0 if you want to use  line  data
          minimum. Default: 0.
 --wl-high=<wavel>
          Upper wavelength. 0 if you want to use  line  data
          maximum. Default: 0.
 --wl-delt=<spacing>
          Wavelength  spacing.  It  cannot  be  0  or  less.
          Default: .2.
 --wl-osamp=<integer>
          Wavelength oversampling. It cannot be 0  or  less.
          Default: 100.
 --wl-fct=<factor>
          Wavelength   factor.   Multiplicating   wavelength
          values by this gives centimeters. If 0 or  1  then
          use centimeters. Default: 0.
 --wl-marg=<boundary>
          Not trustable range  in  microns  at  boundary  of
          line databases. Also transitions  this  much  away
          from  the  requested  range  will  be  considered.
          Default: 0.001.

WAVENUMBER OPTIONS (all in cm-1)
 -n, --wavenumber
          Interactively input wavenumber parameters.
 --wn-low=<waven>
          Lower wavenumber. 0 if you want to use  equivalent
          of the wavelength maximum. Default: 0.
 --wn-high=<waven>
          Upper wavenumber. 0 if you want to use  equivalent
          of the wavelength minimum. Default: 0.
 --wn-delt=<spacing>
          Wavenumber spacing. 0 if  you  want  to  have  the
          same  number  of  points  as  in  the  wavelength
          sampling. Default: 0.
```

```
 --wn-osamp=<integer>
         Wavenumber oversampling. 0 if you want the same
         value as for the wavelengths. Default: 0.
 --wn-fct=<factor>
         Output wavenumber factor. Multiplicating
         wavenumber values by this gives centimeters. If 0
         then use wavelength's value. Note that this only
         applies to output, internally wavenumbers will
         always be in cm-1.. Default: 0.
 --wn-marg=<boundary>
         Not trustable range in cm-1 at boundaries.
         Transitions this much away from the requested
         range will be considered. Use the maximum of the
         wavelength boundaries if this value is 0.

EXTINCTION CALCULATION OPTIONS:
 -f, --finebin=<integer>
         Number of fine-bins to calculate the Voigt
         function. Default: 5.
 -a, --nwidth=<number>
         Number of the max-widths (the greater of Voigt or
         Doppler widths) that need to be contained in a
         calculated Voigt profile. Default: 50.
 -u, --maxratio=<uncert>
         Maximum allowed uncertainty in doppler width
         before recalculating profile. Default: 0.001.
 --per-iso
         Calculates extinction per isotope, this allow
         displaying contribution from different isotopes,
         but also consumes more memory.
 --no-per-iso
         Do not calculate extinction per isotope. Saves
         memory (this is the default) .
 --blowex=<factor>
         Blow extinction by factor before computing tau.
         No physical significance of this variable, but
         only debugging. Default: 1.
 --minelow=<low-energy>
         Only use transitions with this minimum low energy
         (in cm-1). Default: 0.
 --cloudrad=<radup,raddown>
         Make a cloud appear linearly from radup to
         raddown Units specified with '--cloudfct', or use
         radfct if there is none.
```

```
 --cloudfct=<factor>
         cloud radius values specified by '--cloudrad'
         will be amultiplied by this to convert to cgs
         units .
 --cloudext=<extinction>
         Maximum extinction of the cloud, which opacity
         will linearly increase from 'radup' to 'raddown' .
 --detailext=<filename:wn1,wn2,...>
         Save extinction at the particular wavenumbers in
         the specified filename.
 --detailcia=<filename:wn1,wn2,...>
         Save extinction due to CIA at the particular
         wavenumbers in the specified filename.
 --cia=<filenames>
         Use the indicated filenames for CIA opacities, it
         is a comma separated list.
 --saveext=<filename>
         Save extinction array in this file which won't
         need to be recomputed if only the radius scale
         (scale height) changes.

RESULTING RAY OPTIONS:
 -s, --solution=<sol_name>
         Name of the kind of output solution ('slant path'
         is currently the only availabale alternative).
         Default: Slant Path.
 --toomuch=<optdepth>
         If optical depth for a particular path is larger
         than optdepth, then do not proceed to lower
         radius. Default: 20.
 --tauiso=<isoid>
         Compute tau only for isotope indexed in isoid
         (index which can actually be different from what
         you expect). Default: 0.
 --outtau=<#radius>
         Output is optical depth instead of modulation. It
         will be asked which radius to plot . Default: 0.
 --taulevel=<integer>
         Do a level integer integration for optical depth.
         1 is for constant index of refraction (better
         precision), use 2 if it is variable.. Default: 1.
 --modlevel=<integer>
         Do an integration of level <integer> to compute
         modulation. 1 doesn't consider limb darkening. -1
```

```
          doesn't consider limb darkening but it only
          returns the moduated radius at which extinction
          becomes one.. Default: 1.
 --detailtau=<filename:wn1,wn2,...>
          Save optical depth at the particular wavenumbers
          in the specified filename.

OBSERVATIONAL OPTIONS:
 -t, --telres=<width>
          Gaussian width of telescope resolution in nm.
          Default: 1.

GEOMETRY PARAMETERS
 --starrad=<radius_sun>
          Stellar radius in solar radius. Default: 1.125.
 --g-orbpar=<smaxis,time,incl,ecc,long_node,arg_per>
          Orbital parameters, in the above order, to use
          the default of any of these (1,0,0,0,0,0), leave
          the corresponding field blank.
 --g-orbparfct=<unitsof:smaxis,time,incl,ecc,long_node,arg_per>
          Units of orbital parameters, in the above order,
          to use the default of any of these
          (AU,deg,hours,,deg,deg), leave the corresponding
          field blank.
 --transparent
          If selected the planet will have a maximum
          optical depth tgiven by toomuch, it will never be
          totally opaque.
---------------------------------
Contact Information: Patricio Rojo <pato@astro.cornell.edu>
```

E.3 Configuration file

This is the configuration file used to obtain the exoatmospheric water spectrum from 0.7 to 2.6 μm using atmospheric profile supplied by Iro et al. (2005).

This file (if called hd20945t8b.cfg) is processed by `transit` by simply calling: '`transit -p hd209458b.cfg`'. TLI file and output files are stored in 'res/' subdirectory. Atmosphere and CIA file in 'dat/' subdirectory.

```
atm dat/iro/atmosph.dat
linedb res/lineread.big.tli
cia dat/cia/h2h2.dat

wl-low .7
wl-high 2.6
wl-fct 1e-4

wn-low 3840
wn-delt .02
wn-osamp 1

rad-delt 100
toomuch 10

modlevel 1

outtoomuch res/hd209458b_big1-fortney.tm.dat
outsample res/hd209458b_big1-fortney.sam.dat
output res/hd209458b_big1-fortney.dat
```

BIBLIOGRAPHY

Abramowitz, M., Stegun, I. A., 1965. Handbook of Mathematical Functions. Dover, NY.

Ackerman, A. S., Marley, M. S., 2001. Precipitating Condensation Clouds in Substellar Atmospheres. ApJ 556, 872–884.

Agol, E., Steffen, J., Sari, R., Clarkson, W., 2005. On detecting terrestrial planets with timing of giant planet transits. MNRAS 359, 567–579.

Alonso, R., Brown, T. M., Torres, G., Latham, D. W., Sozzetti, A., Mandushev, G., Belmonte, J. A., Charbonneau, D., Deeg, H. J., Dunham, E. W., O'Donovan, F. T., Stefanik, R. P., 2004. TrES-1: The Transiting Planet of a Bright K0 V Star. ApJ 613, L153–L156.

Armstrong, B. H., 1967. Spectrum Line Profiles: The Voigt Function. Journal of Quantitative Spectroscopy and Radiative Transfer 7, 61–88.

Arnold, L., Schneider, J., 2004. The detectability of extrasolar planet surroundings. I. Reflected-light photometry of unresolved rings. A&A 420, 1153–1162.

Arribas, S., Gilliland, R. L., Sparks, W. B., López-Martín, L., Mediavilla, E., Gómez-Alvarez, P., 2006. Exploring the Potential of Integral Field Spectroscopy for Observing Extrasolar Planet Transits: Ground-based Observations of the Atmospheric Na in HD 209458b. PASP 118, 21–36.

Backer, D. C., Foster, R. S., Sallmen, S., 1993. A Second Companion of the Millisecond Pulsar 1620-26. Nature 365, 817–819.

Bakos, G. A., Knutson, H., Pont, F., Moutou, C., Charbonneau, D., Shporer, A., Bouchy, F., Everett, M., Hergenrother, C., Latham, D. W., Mayor, M., Mazeh, T., Noyes, R. W., Queloz, D., Pal, A., Udry, S., 2006. Refined parameters of the planet orbiting HD 189733. ArXiv Astrophysics e-prints arXiv:astro-ph/0603291.

Baraffe, I., Selsis, F., Chabrier, G., Barman, T. S., Allard, F., Hauschildt, P. H., Lammer, H., 2004. The effect of evaporation on the evolution of close-in giant planets. A&A 419, L13–L16.

Barnes, J. W., Fortney, J. J., 2004. Transit Detectability of Ring Systems around Extrasolar Giant Planets. ApJ 616, 1193–1203.

Bastian, T. S., Dulk, G. A., Leblanc, Y., 2000. A Search for Radio Emission from Extrasolar Planets. ApJ 545, 1058–1063.

Beaulieu, J.-P., Bennett, D. P., Fouqué, P., Williams, A., Dominik, M., Jorgensen, U. G., Kubas, D., Cassan, A., Coutures, C., Greenhill, J., Hill, K., Menzies, J., Sackett, P. D., Albrow, M., Brillant, S., Caldwell, J. A. R., Calitz, J. J., Cook, K. H., Corrales, E., Desort, M., Dieters, S., Dominis, D., Donatowicz, J., Hoffman, M., Kane, S., Marquette, J.-B., Martin, R., Meintjes, P., Pollard, K., Sahu, K., Vinter, C., Wambsganss, J., Woller, K., Horne, K., Steele, I., Bramich, D. M., Burgdorf, M., Snodgrass, C., Bode, M., Udalski, A., Szymański, M. K., Kubiak, M., Więckowski, T., Pietrzyński, G., Soszyński, I., Szewczyk, O., Wyrzykowski, Ł., Paczyński, B., Abe, F., Bond, I. A., Britton, T. R., Gilmore, A. C., Hearnshaw, J. B., Itow, Y., Kamiya, K., Kilmartin, P. M., Korpela, A. V., Masuda, K., Matsubara, Y., Motomura, M., Muraki, Y., Nakamura, S., Okada, C., Ohnishi, K., Rattenbury, N. J., Sako, T., Sato, S., Sasaki, M., Sekiguchi, T., Sullivan, D. J., Tristram, P. J., Yock, P. C. M., Yoshioka, T., 2006. Discovery of a cool planet of 5.5 Earth masses through gravitational microlensing. Nature 439, 437–440.

Benedict, G. F., McArthur, B. E., Forveille, T., Delfosse, X., Nelan, E., Butler, R. P., Spiesman, W., Marcy, G., Goldman, B., Perrier, C., Jefferys, W. H., Mayor, M., 2002. A Mass for the Extrasolar Planet Gliese 876b Determined from Hubble Space Telescope Fine Guidance Sensor 3 Astrometry and High-Precision Radial Velocities. ApJ 581, L115–L118.

Berton, A., Gratton, R. G., Feldt, M., Henning, T., Desidera, S., Turatto, M., Schmid, H. M., Waters, R., 2006. Detecting Extrasolar Planets with Integral Field Spectroscopy. ArXiv Astrophysics e-prints arXiv:astro-ph/0605207.

Bétremieux, Y., Yelle, R. V., 1999. HST Detection of H_2 Raman Scattering in the Jovian Atmosphere. Icarus 142, 324–341.

Bodenheimer, P., Laughlin, G., Lin, D. N. C., 2003. On the Radii of Extrasolar Giant Planets. ApJ 592, 555–563.

Bodenheimer, P., Lin, D. N. C., Mardling, R. A., 2001. On the Tidal Inflation of Short-Period Extrasolar Planets. ApJ 548, 466–472.

Bond, I. A., Udalski, A., Jaroszyński, M., Rattenbury, N. J., Paczyński, B., Soszyński, I., Wyrzykowski, L., Szymański, M. K., Kubiak, M., Szewczyk, O., Żebruń, K., Pietrzyński, G., Abe, F., Bennett, D. P., Eguchi, S., Furuta, Y., Hearnshaw, J. B., Kamiya, K., Kilmartin, P. M., Kurata, Y., Masuda, K., Matsubara, Y., Muraki, Y., Noda, S., Okajima, K., Sako, T., Sekiguchi, T., Sullivan, D. J., Sumi, T., Tristram, P. J., Yanagisawa, T., Yock, P. C. M., 2004. OGLE 2003-BLG-235/MOA 2003-BLG-53: A Planetary Microlensing Event. ApJ 606, L155–L158.

Borysow, A., Jorgensen, U. G., Fu, Y., 2001. High-temperature (1000-7000 K) collision-induced absorption of H″2 pairs computed from the first principles,

with application to cool and dense stellar atmospheres. Journal of Quantitative Spectroscopy and Radiative Transfer 68, 235–255.

Boss, A. P., 1995. Proximity of Jupiter-Like Planets to Low-Mass Stars. Science 267, 360–362.

Boss, A. P., 2006. Rapid Formation of Gas Giant Planets around M Dwarf Stars. ApJ 643, 501–508.

Bouchy, F., Pont, F., Santos, N. C., Melo, C., Mayor, M., Queloz, D., Udry, S., 2004. Two new "very hot Jupiters" among the OGLE transiting candidates. A&A 421, L13–L16.

Bouchy, F., Udry, S., Mayor, M., Moutou, C., Pont, F., Iribarne, N., da Silva, R., Ilovaisky, S., Queloz, D., Santos, N. C., Ségransan, D., Zucker, S., 2005. ELODIE metallicity-biased search for transiting Hot Jupiters. II. A very hot Jupiter transiting the bright K star HD 189733. A&A 444, L15–L19.

Brown, T. M., 2001. Transmission Spectra as Diagnostics of Extrasolar Giant Planet Atmospheres. ApJ 553, 1006–1026.

Burrows, A., 2005. A theoretical look at the direct detection of giant planets outside the Solar System. Nature 433, 261–268.

Burrows, A., Guillot, T., Hubbard, W. B., Marley, M. S., Saumon, D., Lunine, J. I., Sudarsky, D., 2000. On the Radii of Close-in Giant Planets. ApJ 534, L97–L100.

Burrows, A., Sudarsky, D., Hubbard, W. B., 2003. A Theory for the Radius of the Transiting Giant Planet HD 209458b. ApJ 594, 545–551.

Burrows, A., Volobuyev, M., 2003. Calculations of the Far-Wing Line Profiles of Sodium and Potassium in the Atmospheres of Substellar-Mass Objects. ApJ 583, 985–995.

Chabrier, G., Barman, T., Baraffe, I., Allard, F., Hauschildt, P. H., 2004. The Evolution of Irradiated Planets: Application to Transits. ApJ 603, L53–L56.

Charbonneau, D., 2004. A Review of the Current Status of Follow-Up Techniques to Study Known Extrasolar Planets. In: Dupree, A. K., Benz, A. O. (Eds.), IAU Symposium. p. 367.

Charbonneau, D., Allen, L. E., Megeath, S. T., Torres, G., Alonso, R., Brown, T. M., Gilliland, R. L., Latham, D. W., Mandushev, G., O'Donovan, F. T., Sozzetti, A., 2005. Detection of Thermal Emission from an Extrasolar Planet. ApJ 626, 523–529.

Charbonneau, D., Brown, T. M., Burrows, A., Laughlin, G., 2006a. When Extrasolar Planets Transit Their Parent Stars. ArXiv Astrophysics e-prints arXiv:astro-ph/0603376.

Charbonneau, D., Brown, T. M., Burrows, A., Laughlin, G., 2006b. When Extrasolar Planets Transit Their Parent Stars. ArXiv Astrophysics e-prints arXiv:astro-ph/0603376.

Charbonneau, D., Brown, T. M., Latham, D. W., Mayor, M., 2000. Detection of Planetary Transits Across a Sun-like Star. ApJ 529, L45–L48.

Charbonneau, D., Brown, T. M., Noyes, R. W., Gilliland, R. L., 2002. Detection of an Extrasolar Planet Atmosphere. ApJ 568, 377–384.

Charbonneau, D., Noyes, R. W., Korzennik, S. G., Nisenson, P., Jha, S., Vogt, S. S., Kibrick, R. I., 1999. An Upper Limit on the Reflected Light from the Planet Orbiting the Star tau Bootis. ApJ 522, L145–L148.

Charbonneau, D., Winn, J. N., Latham, D. W., Bakos, G., Falco, E. E., Holman, M. J., Noyes, R. W., Csák, B., Esquerdo, G. A., Everett, M. E., O'Donovan, F. T., 2006c. Transit Photometry of the Core-dominated Planet HD 149026b. ApJ 636, 445–452.

Chauvin, G., Lagrange, A.-M., Dumas, C., Zuckerman, B., Mouillet, D., Song, I., Beuzit, J.-L., Lowrance, P., 2005. Giant planet companion to 2MASSW J1207334-393254. A&A 438, L25–L28.

Cho, J. Y.-K., Menou, K., Hansen, B. M. S., Seager, S., 2003. The Changing Face of the Extrasolar Giant Planet HD 209458b. ApJ 587, L117–L120.

Clayton, D. D., 1983. Principles of stellar evolution and nucleosynthesis. Chicago: University of Chicago Press, 1983.

Collier Cameron, A., Horne, K., Penny, A., Leigh, C., 2002. A search for starlight reflected from υ And's innermost planet. MNRAS 330, 187–204.

Cooper, C. S., Sudarsky, D., Milsom, J. A., Lunine, J. I., Burrows, A., 2003. Modeling the Formation of Clouds in Brown Dwarf Atmospheres. ApJ 586, 1320–1337.

Cox, A. N., 2000. Allen's astrophysical quantities. Allen's astrophysical quantities, 4th ed. Publisher: New York: AIP Press; Springer, 2000. Edited by Arthur N. Cox. ISBN: 0387987460.

Cuntz, M., Saar, S. H., Musielak, Z. E., 2000. On Stellar Activity Enhancement Due to Interactions with Extrasolar Giant Planets. ApJ 533, L151–L154.

Deming, D., Brown, T. M., Charbonneau, D., Harrington, J., Richardson, L. J., 2005a. A New Search for Carbon Monoxide Absorption in the Transmission Spectrum of the Extrasolar Planet HD 209458b. ApJ 622, 1149–1159.

Deming, D., Harrington, J., Seager, S., Richardson, L. J., 2006. Strong Infrared Emission from the Extrasolar Planet HD 189733b. ApJ 644, 560–564.

Deming, D., Seager, S., Richardson, L. J., Harrington, J., 2005b. Infrared radiation from an extrasolar planet. Nature 434, 740–743.

Dyudina, U. A., Sackett, P. D., Bayliss, D. D. R., Seager, S., Porco, C. C., Throop, H. B., Dones, L., 2005. Phase Light Curves for Extrasolar Jupiters and Saturns. ApJ 618, 973–986.

Ehrenreich, D., Tinetti, G., Lecavelier Des Etangs, A., Vidal-Madjar, A., Selsis, F., 2006. The transmission spectrum of Earth-size transiting planets. A&A 448, 379–393.

Einstein, A., 1936. Lens-Like Action of a Star by the Deviation of Light in the Gravitational Field. Science 84, 506–507.

ESA, 1997. The Hipparcos and Tycho Catalogues (ESA 1997). VizieR Online Data Catalog 1239, http://www.rssd.esa.int/Hipparcos/catalog.html.

Farrell, W. M., Desch, M. D., Lazio, T. J., Bastian, T., Zarka, P., 2003. Limits on the Magnetosphere/Stellar Wind Interactions for the Extrasolar Planet about Tau Bootis. In: Deming, D., Seager, S. (Eds.), ASP Conf. Ser. 294: Scientific Frontiers in Research on Extrasolar Planets. pp. 151–156.

Farrell, W. M., Desch, M. D., Zarka, P., 1999. On the possibility of coherent cyclotron emission from extrasolar planets. J. Geophys. Res. 104, 14025–14032.

Fischer, D. A., Valenti, J., 2005. The Planet-Metallicity Correlation. ApJ 622, 1102–1117.

Fischer, D. A., Valenti, J. A., 2003. Metallicities of Stars with Extrasolar Planets. In: Deming, D., Seager, S. (Eds.), ASP Conf. Ser. 294: Scientific Frontiers in Research on Extrasolar Planets. pp. 117–128.

Fortney, J. J., 2005. The effect of condensates on the characterization of transiting planet atmospheres with transmission spectroscopy. MNRAS 364, 649–653.

Fortney, J. J., Marley, M. S., Lodders, K., Saumon, D., Freedman, R., 2005. Comparative Planetary Atmospheres: Models of TrES-1 and HD 209458b. ApJ 627, L69–L72.

Fortney, J. J., Saumon, D., Marley, M. S., Lodders, K., Freedman, R. S., 2006. Atmosphere, Interior, and Evolution of the Metal-rich Transiting Planet HD 149026b. ApJ 642, 495–504.

Gatewood, G., Han, I., Black, D. C., 2001. A Combined Hipparcos and Multichannel Astrometric Photometer Study of the Proposed Planetary System of ρ Coronae Borealis. ApJ 548, L61–L63.

Gilliland, R. L., Goudfrooij, P., Kimble, R. A., 1999. Linearity and High Signal-to-Noise Performance of the STIS CCD. PASP 111, 1009–1020.

Goody, R. M., Yung, Y. L., 1989. Atmospheric Radiation: Theoretical Basis, 2nd Edition. Oxford University Press, NY.

Gould, A., Udalski, A., An, D., Bennett, D. P., Zhou, A. ., Dong, S., Rattenbury, N. J., Gaudi, B. S., Yock, P. C. M., Bond, I. A., Christie, G. W., Horne, K., Anderson, J., Stanek, K. Z., DePoy, D. L., Han, C., McCormick, J., Park, B. ., Pogge, R. W., Poindexter, S. D., Soszynski, I., Szymanski, M. K., Kubiak, M., Pietrzynski, G., Szewczyk, O., Wyrzykowski, L., Ulaczyk, K., Paczynski, B., Bramich, D. M., Snodgrass, C., Steele, I. A., Burgdorf, M. J., Bode, M. F., Botzler, C. S., Mao, S., Swaving, S. C., 2006. Microlens OGLE-2005-BLG-169 Implies Cool Neptune-Like Planets are Common. ArXiv Astrophysics e-prints arXiv:astro-ph/0603276.

Green, D., Matthews, J., Seager, S., Kuschnig, R., 2003. Scattered Light from Close-in Extrasolar Planets: Prospects of Detection with the MOST Satellite. ApJ 597, 590–601.

Guillot, T., 2005. THE INTERIORS OF GIANT PLANETS: Models and Outstanding Questions. Annual Review of Earth and Planetary Sciences 33, 493–530.

Harrington, J., Luszcz, S. H., Deming, D., Seager, S., Richardson, L. J., 2006. *in preparation* .

Hébrard, G., Lecavelier Des Etangs, A., 2006. A posteriori detection of the planetary transit of HD 189733 b in the Hipparcos photometry. A&A 445, 341–346.

Henry, G. W., Donahue, R. A., Baliunas, S. L., 2002. A False Planet around HD 192263. ApJ 577, L111–L114.

Henry, G. W., Marcy, G. W., Butler, R. P., Vogt, S. S., 2000. A Transiting "51 Peg-like" Planet. ApJ 529, L41–L44.

Holman, M. J., Murray, N. W., 2005. The Use of Transit Timing to Detect Terrestrial-Mass Extrasolar Planets. Science 307, 1288–1291.

Holman, M. J., Winn, J. N., Stanek, K. Z., Torres, G., Sasselov, D. D., Allen, R. L., Fraser, W., 2005. High-precision Transit Photometry of OGLE-TR-10. ArXiv Astrophysics e-prints arXiv:astro-ph/0506569.

Horne, K., 1986. An optimal extraction algorithm for CCD spectroscopy. PASP 98, 609–617.

Horne, K., 2003. Status aand Prospects of Planetary Transit Searches: Hot Jupiters Galore. In: Deming, D., Seager, S. (Eds.), ASP Conf. Ser. 294: Scientific Frontiers in Research on Extrasolar Planets. pp. 361–370.

Hubbard, W. B., Fortney, J. J., Lunine, J. I., Burrows, A., Sudarsky, D., Pinto, P., 2001. Theory of Extrasolar Giant Planet Transits. ApJ 560, 413–419.

Ida, S., Lin, D. N. C., 2004a. Toward a Deterministic Model of Planetary Formation. I. A Desert in the Mass and Semimajor Axis Distributions of Extrasolar Planets. ApJ 604, 388–413.

Ida, S., Lin, D. N. C., 2004b. Toward a Deterministic Model of Planetary Formation. II. The Formation and Retention of Gas Giant Planets around Stars with a Range of Metallicities. ApJ 616, 567–572.

Ikoma, M., Hidenori, G., 2006. Constraints on the Mass of a Habitable Planet with Water of Nebular Origin. ApJ .

Ip, W.-H., Kopp, A., Hu, J.-H., 2004. On the Star-Magnetosphere Interaction of Close-in Exoplanets. ApJ 602, L53–L56.

Iro, N., Bézard, B., Guillot, T., 2005. A time-dependent radiative model of HD 209458b. A&A 436, 719–727.

Jackson, J. D., 1999. Classical Electrodynamics, 3rd Edition. John Wiley & Sons, Inc, NY.

Jenkins, J. M., Doyle, L. R., 2003. Detecting Reflected Light from Close-in Extrasolar Giant Planets with the Kepler Photometer. ApJ 595, 429–445.

Jha, S., Charbonneau, D., Garnavich, P. M., Sullivan, D. J., Sullivan, T., Brown, T. M., Tonry, J. L., 2000. Multicolor Observations of a Planetary Transit of HD 209458. ApJ 540, L45–L48.

Karkoschka, E., 1994. Spectrophotometry of the jovian planets and Titan at 300- to 1000-nm wavelength: The methane spectrum. Icarus 111, 174–192.

Kasting, J. F., Whitmire, D. P., Reynolds, R. T., 1993. Habitable Zones around Main Sequence Stars. Icarus 101, 108–128.

Knutson, H., Charbonneau, D., Noyes, R. W., Brown, T. M., Gilliland, R. L., 2006. Using Stellar Limb-Darkening to Refine the Properties of HD 209458b. ArXiv Astrophysics e-prints arXiv:astro-ph/0603542.

Konacki, M., Torres, G., Jha, S., Sasselov, D. D., 2003. An extrasolar planet that transits the disk of its parent star. Nature 421, 507–509.

Konacki, M., Torres, G., Sasselov, D. D., Jha, S., 2005. A Transiting Extrasolar Giant Planet around the Star OGLE-TR-10. ApJ 624, 372–377.

Kurucz, R., 1999. H20 linelist from partridge and schwenke (1997), kurucz CDROMs 25 and 26.

Kuskov, O. L., Kronrod, V. A., 2005. Internal structure of Europa and Callisto. Icarus 177, 550–569.

Laughlin, G., Bodenheimer, P., Adams, F. C., 2004. The Core Accretion Model Predicts Few Jovian-Mass Planets Orbiting Red Dwarfs. ApJ 612, L73–L76.

Laughlin, G., Butler, R. P., Fischer, D. A., Marcy, G. W., Vogt, S. S., Wolf, A. S., 2005a. The GJ 876 Planetary System: A Progress Report. ApJ 622, 1182–1190.

Laughlin, G., Marcy, G. W., Vogt, S. S., Fischer, D. A., Butler, R. P., 2005b. On the Eccentricity of HD 209458b. ApJ 629, L121–L124.

Laughlin, G., Wolf, A., Vanmunster, T., Bodenheimer, P., Fischer, D., Marcy, G., Butler, P., Vogt, S., 2005c. A Comparison of Observationally Determined Radii with Theoretical Radius Predictions for Short-Period Transiting Extrasolar Planets. ApJ 621, 1072–1078.

Lazorenko, P. F., 2006. Astrometric precision of observations at VLT/FORS2. A&A 449, 1271–1279.

Leigh, C., Cameron, A. C., Guillot, T., 2003a. Prospects for spectroscopic reflected-light planet searches. MNRAS 346, 890–896.

Leigh, C., Collier Cameron, A., Udry, S., Donati, J.-F., Horne, K., James, D., Penny, A., 2003b. A search for starlight reflected from HD 75289b. MNRAS 346, L16–L20.

Lopez, B., Schneider, J., Danchi, W. C., 2005. Can Life Develop in the Expanded Habitable Zones around Red Giant Stars? ApJ 627, 974–985.

Lovis, C., Mayor, M., Pepe, F., Alibert, Y., Benz, W., Bouchy, F., Correia, A. C. M., Laskar, J., Mordasini, C., Queloz, D., Santos, N. C., Udry, S., Bertaux, J.-L., Sivan, J.-P., 2006. An extrasolar planetary system with three Neptune-mass planets. Nature 441, 305–309.

Lucas, P. W., Roche, P. F., 2002. A search for the infrared spectroscopic signature of hot Jupiter planets. MNRAS 336, 637–642.

Malumuth, E. M., Hill, R. J., Cheng, E. S., Cottingham, D. A., Wen, Y., Johnson, S. D., Hill, R. S., 2003a. Model of Fringing in the WFC3 CCDs. In: Proceedings of the SPIE. Vol. 4854. pp. 567–576.

Malumuth, E. M., Hill, R. S., Gull, T., Woodgate, B. E., Bowers, C. W., Kimble, R. A., Lindler, D., Plait, P., Blouke, M., 2003b. Removing the Fringes from Space Telescope Imaging Spectrograph Slitless Spectra. PASP 115, 218–234.

Marcy, G., Butler, R. P., Fischer, D., Vogt, S., Wright, J. T., Tinney, C. G., Jones, H. R. A., 2005. Observed Properties of Exoplanets: Masses, Orbits, and Metallicities. Progress of Theoretical Physics Supplement 158, 24–42.

Marcy, G. W., Butler, R. P., Fischer, D., Vogt, S. S., Lissauer, J. J., Rivera, E. J., 2001. A Pair of Resonant Planets Orbiting GJ 876. ApJ 556, 296–301.

Marcy, G. W., Butler, R. P., Fischer, D. A., Vogt, S. S., 2003. Properties of Extrasolar Planets. In: Deming, D., Seager, S. (Eds.), ASP Conf. Ser. 294: Scientific Frontiers in Research on Extrasolar Planets. pp. 1–58381.

Marley, M. S., Gelino, C., Stephens, D., Lunine, J. I., Freedman, R., 1999. Reflected Spectra and Albedos of Extrasolar Giant Planets. I. Clear and Cloudy Atmospheres. ApJ 513, 879–893.

Mayor, M., Queloz, D., 1995. A Jupiter-Mass Companion to a Solar-Type Star. Nature 378, 355–359.

Mazeh, T., Naef, D., Torres, G., Latham, D. W., Mayor, M., Beuzit, J.-L., Brown, T. M., Buchhave, L., Burnet, M., Carney, B. W., Charbonneau, D., Drukier, G. A., Laird, J. B., Pepe, F., Perrier, C., Queloz, D., Santos, N. C., Sivan, J.-P., Udry, S., Zucker, S., 2000. The Spectroscopic Orbit of the Planetary Companion Transiting HD 209458. ApJ 532, L55–L58.

McCullough, P. R., Stys, J. E., Valenti, J. A., Johns-Krull, C. M., Janes, K. A., Heasley, J. N., Bye, B. A., Dodd, C., Fleming, S. W., Pinnick, A., Bissinger, R., Gary, B. L., Howell, P. J., Vanmunster, T., 2006. A Transiting Planet of a Sun-like Star. ArXiv Astrophysics e-prints arXiv:astro-ph/0605414.

McLean, I. S., Becklin, E. E., Bendiksen, O., Brims, G., Canfield, J., Figer, D. F., Graham, J. R., Hare, J., Lacayanga, F., Larkin, J. E., Larson, S. B., Levenson, N., Magnone, N., Teplitz, H., Wong, W., 1998. Design and development of NIRSPEC: a near-infrared echelle spectrograph for the Keck II telescope. In: Fowler, A. M. (Ed.), Proc. SPIE Vol. 3354, p. 566-578, Infrared Astronomical Instrumentation, Albert M. Fowler; Ed. pp. 566–578.

Mellau, G. C., Winnewisser, B. P., 1995. A Method to Remove Fringing from FT-IR Spectra. In: ASP Conf. Ser. 81: Laboratory and Astronomical High Resolution Spectra. p. 138.

Melott, A., 2004. Ozone Abundance in a Nitrogen-Carbon Dioxide Dominated Terrestrial Paleoatmosphere. American Astronomical Society Meeting Abstracts 205, 1431.

Menou, K., Tabachnik, S., 2003. Dynamical Habitability of Known Extrasolar Planetary Systems. ApJ 583, 473–488.

Mihalas, D., 1978. Stellar atmospheres, 2nd Edition. W. H. Freeman and Co., San Francisco.

Miralda-Escudé, J., 2002. Orbital Perturbations of Transiting Planets: A Possible Method to Measure Stellar Quadrupoles and to Detect Earth-Mass Planets. ApJ 564, 1019–1023.

Montanes-Rodriguez, P., Palle, E., Goode, P. R., 2006. Vegetation signature in the observed globally-integrated spectrum of Earth: Modeling the red edge strength using simultaneous cloud data and application for extrasolar planets. ArXiv Astrophysics e-prints arXiv:astro-ph/0604420.

Moorwood, A., Cuby, J.-G., Biereichel, P., Brynnel, J., Delabre, B., Devillard, N., van Dijsseldonk, A., Finger, G., Gemperlein, H., Gilmozzi, R., Herlin, T., Huster, G., Knudstrup, J., Lidman, C., Lizon, J.-L., Mehrgan, H., Meyer, M., Nicolini, G., Petr, M., Spyromilio, J., Stegmeier, J., 1998. ISAAC sees first light at the VLT. The Messenger 94, 7–9.

Moutou, C., Pont, F., Bouchy, F., Mayor, M., 2004. Accurate radius and mass of the transiting exoplanet OGLE-TR-132b. A&A 424, L31–L34.

Paczynski, B., 1986. Gravitational microlensing by the galactic halo. ApJ 304, 1–5.

Partridge, H., Schwenke, D. W., 1997. The Determination of an Accurate Isotope Dependent Potential Energy Surface for Water from Extensive Ab Initio Calculations and Experimental Data. J. Chem. Phys. 106, 4618–4639, [P&S].

Pepper, J., Gaudi, B. S., 2005. Searching for Transiting Planets in Stellar Systems. ApJ 631, 581–596.

Pierlushi, J. H., Vanderwood, P. C., Gomez, R. B., 1977. Fast Calculation Algorithm for the Voigt Profile. Journal of Quantitative Spectroscopy and Radiative Transfer 18, 555–558.

Pont, F., Bouchy, F., Queloz, D., Santos, N. C., Melo, C., Mayor, M., Udry, S., 2004. The "missing link": A 4-day period transiting exoplanet around OGLE-TR-111. A&A 426, L15–L18.

Richardson, L. J., Deming, D., Seager, S., 2003a. Infrared Observations during the Secondary Eclipse of HD 209458b. II. Strong Limits on the Infrared Spectrum Near 2.2 μm. ApJ 597, 581–589.

Richardson, L. J., Deming, D., Wiedemann, G., Goukenleuque, C., Steyert, D., Harrington, J., Esposito, L. W., 2003b. Infrared Observations during the Secondary Eclipse of HD 209458b. I. 3.6 Micron Occultation Spectroscopy Using the Very Large Telescope. ApJ 584, 1053–1062.

Richardson, L. J., Seager, S., Harrington, J., Deming, D., 2005. The Radius of HD 209458 b at 24 Microns. American Astronomical Society Meeting Abstracts 207, #191.07.

Rieke, G. H., 2003. Detection of light: from the ultraviolet to the submillimeter. Detection of light: from the ultraviolet to the submillimeter, by G.H. Rieke. 2nd ed. Cambridge, UK: Cambridge University Press, 2003.

Rivera, E. J., Lissauer, J. J., Butler, R. P., Marcy, G. W., Vogt, S. S., Fischer, D. A., Brown, T. M., Laughlin, G., Henry, G. W., 2005. A ~7.5 $M_\oplus$ Planet Orbiting the Nearby Star, GJ 876. ApJ 634, 625–640.

Rojo, P., Harrington, J., 2006. A Method To Remove Fringes From Images Using Wavelets. ArXiv Astrophysics e-prints arXiv:astro-ph/0605609.

Rowe, J. F., Matthews, J. M., Seager, S., Kuschnig, R., Guenther, D. B., Moffat, A. F. J., Rucinski, S. M., Sasselov, D., Walker, G. A. H., Weiss, W. W., 2006. An Upper Limit on the Albedo of HD 209458b: Direct Imaging Photometry with the MOST Satellite. ArXiv Astrophysics e-prints arXiv:astro-ph/0603410.

Rubenstein, E. P., Schaefer, B. E., 2000. Are Superflares on Solar Analogues Caused by Extrasolar Planets? ApJ 529, 1031–1033.

Rybicki, G., Lightman, A., 1979. Radiative processes in Astrophysics, 1st Edition. John Wiley & Sons, Inc, New York; Toronto.

Saar, S. H., Cuntz, M., 2001. A search for Ca ii emission enhancement in stars resulting from nearby giant planets. MNRAS 325, 55–59.

Sakurai, J. J., 1994. Modern Quantum Mechanics, revised Edition. Addison-Wesley Publishing Co., Reading, MA; Menlo Park, CA; New York.

Sánchez-Lavega, A., 2004. The Magnetic Field in Giant Extrasolar Planets. ApJ 609, L87–L90.

Santos, N. C., Israelian, G., Mayor, M., 2004. Spectroscopic [Fe/H] for 98 extra-solar planet-host stars. Exploring the probability of planet formation. A&A 415, 1153–1166.

Santos, N. C., Pont, F., Melo, C., Israelian, G., Bouchy, F., Mayor, M., Moutou, C., Queloz, D., Udry, S., Guillot, T., 2006. High resolution spectroscopy of stars with transiting planets. The cases of OGLE-TR-10, 56, 111, 113, and TrES-1. A&A 450, 825–831.

Santos, N. C., Udry, S., Mayor, M., Naef, D., Pepe, F., Queloz, D., Burki, G., Cramer, N., Nicolet, B., 2003. The CORALIE survey for southern extra-solar planets. XI. The return of the giant planet orbiting HD 192263. A&A 406, 373–381.

Sato, B., Fischer, D. A., Henry, G. W., Laughlin, G., Butler, R. P., Marcy, G. W., Vogt, S. S., Bodenheimer, P., Ida, S., Toyota, E., Wolf, A., Valenti, J. A., Boyd, L. J., Johnson, J. A., Wright, J. T., Ammons, M., Robinson, S., Strader, J., McCarthy, C., Tah, K. L., Minniti, D., 2005. The N2K Consortium. II. A Transiting Hot Saturn around HD 149026 with a Large Dense Core. ApJ 633, 465–473.

Seager, S., 2003. The Significance of the Sodium Detection in the Extrasolar Planet HD 209458b Atmosphere. In: Deming, D., Seager, S. (Eds.), ASP Conf. Ser. 294: Scientific Frontiers in Research on Extrasolar Planets. pp. 457–466.

Seager, S., Hui, L., 2002. Constraining the Rotation Rate of Transiting Extrasolar Planets by Oblateness Measurements. ApJ 574, 1004–1010.

Seager, S., Richardson, L. J., Hansen, B. M. S., Menou, K., Cho, J. Y.-K., Deming, D., 2005a. On the Dayside Thermal Emission of Hot Jupiters. ApJ 632, 1122–1131.

Seager, S., Turner, E. L., Schafer, J., Ford, E. B., 2005b. Vegetation's Red Edge: A Possible Spectroscopic Biosignature of Extraterrestrial Plants. Astrobiology 5, 372–390.

Seager, S., Whitney, B. A., Sasselov, D. D., 2000. Photometric Light Curves and Polarization of Close-in Extrasolar Giant Planets. ApJ 540, 504–520.

Shkolnik, E., Walker, G. A. H., Bohlender, D. A., 2003. Evidence for Planet-induced Chromospheric Activity on HD 179949. ApJ 597, 1092–1096.

Shkolnik, E., Walker, G. A. H., Bohlender, D. A., Gu, P.-G., Kürster, M., 2005. Hot Jupiters and Hot Spots: The Short- and Long-Term Chromospheric Activity on Stars with Giant Planets. ApJ 622, 1075–1090.

Showman, A. P., Guillot, T., 2002. Atmospheric circulation and tides of "51 Pegasus b-like" planets. A&A 385, 166–180.

Skrutskie, M. F., Cutri, R. M., Stiening, R., Weinberg, M. D., Schneider, S., Carpenter, J. M., Beichman, C., Capps, R., Chester, T., Elias, J., Huchra, J., Liebert, J., Lonsdale, C., Monet, D. G., Price, S., Seitzer, P., Jarrett, T., Kirkpatrick, J. D., Gizis, J. E., Howard, E., Evans, T., Fowler, J., Fullmer, L., Hurt, R., Light, R., Kopan, E. L., Marsh, K. A., McCallon, H. L., Tam, R., Van Dyk, S., Wheelock, S., 2006. The Two Micron All Sky Survey (2MASS). AJ 131, 1163–1183, http://www.ipac.caltech.edu/2mass/releases/allsky/index.html.

Spencer, J. R., Pearl, J. C., Segura, M., Flasar, F. M., Mamoutkine, A., Romani, P., Buratti, B. J., Hendrix, A. R., Spilker, L. J., Lopes, R. M. C., 2006. Cassini Encounters Enceladus: Background and the Discovery of a South Polar Hot Spot. Science 311, 1401–1405.

Starck, J.-L., Murtagh, F., 2002. Astronomical image and data analysis. Berlin: Springer.

Stevens, I. R., 2005. Magnetospheric radio emission from extrasolar giant planets: the role of the host stars. MNRAS 356, 1053–1063.

Struve, O., 1952. Proposal for a project of high-precision stellar radial velocity work. The Observatory 72, 199–200.

Sudarsky, D., Burrows, A., Hubeny, I., 2003. Theoretical Spectra and Atmospheres of Extrasolar Giant Planets. ApJ 588, 1121–1148.

Sudarsky, D., Burrows, A., Hubeny, I., Li, A., 2005. Phase Functions and Light Curves of Wide-Separation Extrasolar Giant Planets. ApJ 627, 520–533.

Tingley, B., 2004. Using color photometry to separate transiting exoplanets from false positives. A&A 425, 1125–1131.

Tingley, B., Sackett, P. D., 2005. A Photometric Diagnostic to Aid in the Identification of Transiting Extrasolar Planets. ApJ 627, 1011–1018.

Tingley, B., Thurl, C., Sackett, P., 2006. The color signature of the transit of HD 209458: discrepancies between stellar atmospheric models and observations. A&A 445, L27–L30.

Torrence, C., Compo, G. P., 1998. A practical guide to wavelet analysis. Bull. of the Am. Meteor. Soc. 79, 61–78.

Udalski, A., Jaroszyński, M., Paczyński, B., Kubiak, M., Szymański, M. K., Soszyński, I., Pietrzyński, G., Ulaczyk, K., Szewczyk, O., Wyrzykowski, Ł., Christie, G. W., DePoy, D. L., Dong, S., Gal-Yam, A., Gaudi, B. S., Gould, A., Han, C., Lépine, S., McCormick, J., Park, B.-G., Pogge, R. W., Bennett, D. P., Bond, I. A., Muraki, Y., Tristram, P. J., Yock, P. C. M., Beaulieu, J.-P., Bramich, D. M., Dieters, S. W., Greenhill, J., Hill, K., Horne, K., Kubas, D., 2005. A Jovian-Mass Planet in Microlensing Event OGLE-2005-BLG-071. ApJ 628, L109–L112.

Udalski, A., Paczynski, B., Zebrun, K., Szymaski, M., Kubiak, M., Soszynski, I., Szewczyk, O., Wyrzykowski, L., Pietrzynski, G., 2002a. The Optical Gravitational Lensing Experiment. Search for Planetary and Low-Luminosity Object Transits in the Galactic Disk. Results of 2001 Campaign. Acta Astronomica 52, 1–37.

Udalski, A., Pietrzynski, G., Szymanski, M., Kubiak, M., Zebrun, K., Soszynski, I., Szewczyk, O., Wyrzykowski, L., 2003. The Optical Gravitational Lensing Experiment. Additional Planetary and Low-Luminosity Object Transits from the OGLE 2001 and 2002 Observational Campaigns. Acta Astronomica 53, 133–149.

Udalski, A., Szewczyk, O., Zebrun, K., Pietrzynski, G., Szymanski, M., Kubiak, M., Soszynski, I., Wyrzykowski, L., 2002b. The Optical Gravitational Lensing Experiment. Planetary and Low-Luminosity Object Transits in the Carina Fields of the Galactic Disk. Acta Astronomica 52, 317–359.

Vidal-Madjar, A., Désert, J.-M., Lecavelier des Etangs, A., Hébrard, G., Ballester, G. E., Ehrenreich, D., Ferlet, R., McConnell, J. C., Mayor, M., Parkinson, C. D., 2004. Detection of Oxygen and Carbon in the Hydrodynamically Escaping Atmosphere of the Extrasolar Planet HD 209458b. ApJ 604, L69–L72.

Vidal-Madjar, A., Lecavelier des Etangs, A., Désert, J.-M., Ballester, G. E., Ferlet, R., Hébrard, G., Mayor, M., 2003. An extended upper atmosphere around the extrasolar planet HD209458b. Nature 422, 143–146.

Wallace, L., Livingston, W., Hinkle, K., Bernath, P., 1996. Infrared Spectral Atlases of the Sun from NOAO. ApJS 106, 165–169.

Wiedemann, G., Deming, D., Bjoraker, G., 2001. A Sensitive Search for Methane in the Infrared Spectrum of τ Bootis. ApJ 546, 1068–1074.

Winglee, R. M., Dulk, G. A., Bastian, T. S., 1986. A search for cyclotron maser radiation from substellar and planet-like companions of nearby stars. ApJ 309, L59–L62.

Winn, J. N., Holman, M. J., 2005. Obliquity Tides on Hot Jupiters. ApJ 628, L159–L162.

Winn, J. N., Noyes, R. W., Holman, M. J., Charbonneau, D., Ohta, Y., Taruya, A., Suto, Y., Narita, N., Turner, E. L., Johnson, J. A., Marcy, G. W., Butler, R. P., Vogt, S. S., 2005. Measurement of Spin-Orbit Alignment in an Extrasolar Planetary System. ApJ 631, 1215–1226.

Wittenmyer, R. A., Welsh, W. F., Orosz, J. A., Schultz, A. B., Kinzel, W., Kochte, M., Bruhweiler, F., Bennum, D., Henry, G. W., Marcy, G. W., Fischer, D. A., Butler, R. P., Vogt, S. S., 2005. System Parameters of the Transiting Extrasolar Planet HD 209458b. ApJ 632, 1157–1167.

Wolszczan, A., 1994. Confirmation of Earth Mass Planets Orbiting the Millisecond Pulsar PSR:B1257+12. Science 264, 538–542.

Wolszczan, A., Frail, D. A., 1992. A planetary system around the millisecond pulsar PSR1257 + 12. Nature 355, 145–147.

Woolf, N. J., Smith, P. S., Traub, W. A., Jucks, K. W., 2002. The Spectrum of Earthshine: A Pale Blue Dot Observed from the Ground. ApJ 574, 430–433.

Zarka, P., Treumann, R. A., Ryabov, B. P., Ryabov, V. B., 2001. Magnetically-Driven Planetary Radio Emissions and Application to Extrasolar Planets. Ap&SS 277, 293–300.

Zucker, S., Mazeh, T., 2000. Analysis of the Hipparcos Measurements of HD 10697: A Mass Determination of a Brown Dwarf Secondary. ApJ 531, L67–L69.

GLOSSARY

Wikipedia* was used extensively in the creation of this glossary. Other resources included books like "Detection of Light"(Rieke, 2003)

ABBA cycle: Standard procedure in spectral IR observations where the telescope is nodded such that the spectra will appear in two different positions in the detector array (beams A and B). Then, consecutive frames at different beam positions can be subtracted to eliminate the emission from the sky.

AMU: Atomic Mass Unit. It is defined as 1/12 the mass of Carbon-12, or $1.66053886 \times 10^{-24}$ grams.

airmass: The path length that the light from a celestial source has to travel through the Earth's atmosphere in units of the distance it would have traveled if the source were at the zenith. In a first approximation (plane-parallel atmosphere) it is obtained by taking the inverse of the cosine of the zenith angle z:

$$\text{airmass} = \frac{1}{\cos z}$$

blackbody: An object that absorbs all electromagnetic radiation that falls onto it. The amount of radiation they emit per frequency I_ν is directly related to their temperature and is given by:

$$I(\nu) = \frac{2h\nu^3}{c^2} \frac{1}{\exp(\frac{h\nu}{kT}) - 1}, \tag{E.1}$$

where ν, h, and c are the frequency, the Planck constant, and the speed of light, respectively.

c.g.s.: Centimeter-Gram-Second. This is a standard system where every physical unit is expressed in terms of these 3 basic units. This system is used throughout this work.

dark current: The signal produced by the detector in absence of photon illumination.

declination: Also designed by *dec*. It is one of the two coordinates of the equatorial coordinate system (the other is right ascension). Declination is comparable to latitude, projected unto the celestial sphere and is measured in degrees north (or positive) and south (or negative) of the celestial equator.

*http://www.wikipedia.com

Earth: The planet immediately below most of us. Symbol: $\oplus$

EGP: Extrasolar Giant Planet.

ephemeris: From the Greek word ephemeros: daily. Information about the position and timing of astronomical objects and/or events.

FWHM: Full-Width-Half-Maximum. Is an expression of the extent of a function, given by the difference between the two extreme values of the independent variable at which the dependent variable is equal to half of its maximum value. In other words, it measures the full width of a feature at a height equal to the half of the feature's maximum.

magnitude: The logarithmic measure of the brightness of an object, measured in a specific wavelength or passband (e.g., B, V, R for blue, central, and red passbands in the visible spectrum, respectively). The scale is inverted such that brighter objects have a smaller magnitude. The average human eye can see stars up to a magnitude $V = 6$.

main sequence star: Most stars, when placed in a temperature-luminosity diagram, are located in a well-defined region, which is called the main sequence. This happens because when they burn Hydrogen in their cores there is a direct relationship between surface temperature and radius (and thus total luminosity). Since such hydrogen burning stage is the longest stage in the life of every star, the main sequence is the most populated area of a temperature-luminosity diagram.

IR: Infrared (Infra + Red). The electromagnetic radiation of a wavelength longer than that of visible light, but shorter than that of microwave radiation (approximately between 0.75μm and 1 mm)

opacity: The amount of light per unit density absorbed by a medium.

phase: In the context of this work phase always refers to the system phase which goes from -0.5 to 0.5 as the planet transits around the star. Phase 0 is at the center of the transit.

Poisson noise: Noise in the photon flux, which it is always assumed to follow Poisson statistics.

quantum mechanics (QM): Is a fundamental area of theoretical astrophysics dealing with the behavior of matter and waves at the atomic and subatomic levels.

red giant: They are stars of 0.4 - 100 times the mass of the Sun, which have exhausted their supply of hydrogen in their cores and moved out of the main sequence. They have hydrogen fusion in a shell outside the core.

right ascension: Also designed as R.A. or α. It is one of the coordinates of the equatorial coordinate system (the other is declination). Right ascension is comparable to longitude, projected unto the celestial sphere and is measured in hours (0^h-$23^h59^m59.\bar{9}^s$) from the vernal equinox point.

seeing: The blurring and twinkling of astronomical objects caused by turbulence in the Earth's atmosphere. It measures the FWHM of the observed disc of a point source.

SNR: Signal-to-Noise Ratio. A widely used quantity that indicates the signal strength in units of the noise it exhibits.

STP: Standard Temperature and Pressure. Those standard conditions are defined to be 15°C for temperature and 1 atmosphere for pressure.

spectral type: A classification of stars based on photospheric temperature and its associated spectral characteristics.

spectrograph slit: A slit of variable width in the intrument's optics. Its function is to let through light from only a thin slice of the sky so that it can be wavelength-dispersed in the direction perpendicular to the slit.

TCM-i: Telluric Correction Method #i. This acronym is defined for this work and identifies each of the telluric correction methods in §4.2.3.

telescope overhead: Both the time a telescope requires to position itself on the new target and the time it takes to read the values in the detection array. In other words, it is the observing time that is lost to the technical requirements of the telescope.

telluric: Of or pertaining to the Earth, e.g., telluric water vapor is the water vapor present in the atmosphere of our planet.

TLI: Transit Line Information. Format in which `transit` expects the line information to be stored. A TLI file is created by the accompanying routine `lineread`.

zenith: Point in the sky directly overhead.

INDEX

Page numbers in **bold** face indicate that the page contains a section where the entry is the main topic.